



Title	Studies on Structure-Controlled Nano-carbon Materials for Electrocatalysis
Author(s)	金, 制憲
Citation	北海道大学. 博士(理学) 甲第13359号
Issue Date	2018-09-25
DOI	10.14943/doctoral.k13359
Doc URL	http://hdl.handle.net/2115/71987
Type	theses (doctoral)
File Information	Jeheon_Kim.pdf



[Instructions for use](#)

Studies on Structure-Controlled Nano- carbon Materials for Electrocatalysis

電極触媒能を有する構造規制ナノカーボンに関する研究

Jeheon Kim

Graduate School of Chemical Sciences and Engineering

Hokkaido University

2018

Contents

Chapter 1	General Introduction	1
Chapter 2	Selective syntheses of graphitic carbon and polyacetylene by electrochemical deposition	45
Chapter 3	Synthesis and electrocatalytic activity for nitrogen doped vertically aligned carbon nanotube	64
Chapter 4	Synthesis and electrocatalytic activity for fluorine-doped carbon	81
Chapter 5	General conclusion	118
List of Publication		121
Acknowledgments		122

Chapter 1

General Introduction

Carbon is the 6th element and a member of group 14 in the periodic table. In general, elemental carbon has the nonmetallic property and tetravalent character which is important because the four electrons are able to form covalent chemical bonds.¹ Carbon material can be found as various allotropes, which have different structures. In addition, carbon allotropes have rich deposits (the fourth abundant element in the universe by mass) and many applications with long history.²⁻⁷ These carbon materials have different physical, chemical, electrochemical, catalytic and mechanical properties.⁸ To explore the carbon allotropes, many researchers have studied the synthesis method and structural evaluation of them.⁹⁻¹²

Furthermore, synthesized carbon allotropes have potential electrocatalytic activity for hydrogen evolution reaction (HER), oxygen reduction reaction (ORR), and oxygen evolution reaction (OER). In particular, catalytic activity of carbon allotropes can be enhanced by heteroatom-doping such as nitrogen, sulfur, boron, and phosphorus to carbon allotropes.¹³⁻¹⁸ Therefore, heteroatom-doped carbon allotropes are used as electrochemical catalyst for commercial application.¹⁹

In this chapter, I introduce the carbon allotropes, their properties, synthesis methods, and evaluation methods for the physicochemical understanding of carbon. I will also review the principle of ORR and OER for heteroatom-doped carbon catalysts.

1.1 Molecular orbital theory for carbon nanomaterial

In general, each orbital in single atom is characterized by the principal quantum number (n), azimuthal quantum number (l), and the magnetic quantum number (m).²⁰ Besides, electrons occupy s orbitals, p orbitals, d orbitals, and f orbitals which are orbitals with azimuthal quantum number $l = 0, 1, 2,$ and 3 .²¹ From the *Schrodinger equation* and *Pauli's exclusion principle*, electron energies can be calculated by quantum number. Orbital with $n = 1$ can hold one or two electrons, whereas the orbital with $n = 2$ level can hold up to eight electrons in 2s and 2p subshells.^{22,23} The valence bond is formed through the interaction between atomic orbitals. For example, carbon can be occupied by two electrons in 1s, two electrons in 2s, and two electrons in 2p_x, 2p_y, 2p_z. However, it is known that CH₂ is unstable and cannot exist without reaction, while CH₄ can exist as stable form. To form the four bonds, the configuration of carbon must have four unpaired electrons. This is effect from sp³ hybrid orbitals.²⁴ Therefore, orbital hybridization of carbon can leads to different bond structures such as single bond, double bond, and triple bond, resulting in different carbon allotropes.

All of these carbon allotropes can be divided into subcategories as zero-dimension (nanoparticle), one-dimension (nanowires and nanotubes), two-dimension (layered materials), and three-dimension (diamond and graphite) as shown in Fig 1.1. Change of atomic coordinates can influence on the inherent properties.

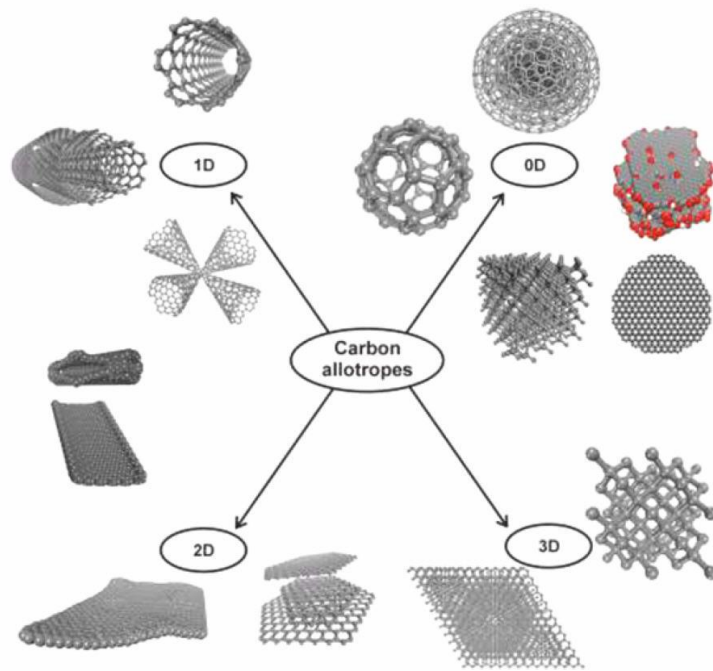


Fig 1.1 Schematic image of carbon allotropes

1.1.1 Zero-dimensional carbon

Zero-dimensional carbon nanomaterials are represented by carbon nanoparticle structure such as fullerene, onion-like carbon, nanodiamond, and graphene quantum dots.²⁵⁻²⁷ Among them, fullerene is well known as zero-dimensional carbon allotrope which is composed with hexagonal rings and pentagonal rings with spherical shape.²⁸ Population of experimentally produced fullerene are rich with C₆₀ spherical molecule and lower numbers of magic-numbered clustered carbons (e.g., C₇₀, C₇₆, C₈₂, and C₈₄). In case of the C₆₀ fullerene, many researchers have studied on physical, chemical, and electrical properties because of its stability. For example, the ¹³C nuclear magnetic resonance (NMR) spectrum of C₆₀ shows a single resonance at 143.2 ppm because all of its carbon nuclei are equivalent as shown in Fig 1.2a.²⁹ In addition, optical property of the fullerene is characterized by electronic structure of fullerene molecules. In case of UV-Vis absorption spectrum, C₆₀ in hexane shows intense band at 213, 257, and 329 nm. On the other hand, C₇₀ in hexane has several intense bands at 214, 236, 360, 378, and 468 nm as shown in Fig 1.2b. As a result, C₆₀ and C₇₀ have the different color in toluene as deep purple and red, respectively. Furthermore, fullerene has been used as donor/acceptor based solar cell because of its high electron affinity.³⁰ For other zero-dimensional carbon allotropes, graphene quantum dots, carbon dots, and nanodiamonds are studied on the electrochemical, physical, and photochemical properties.^{26,27,31}

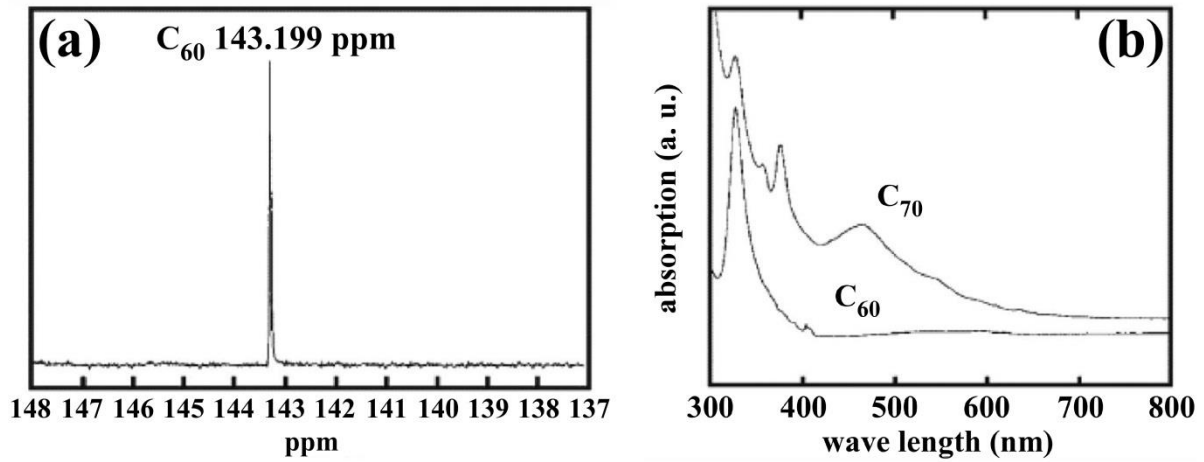


Fig 1.2 (a) ^{13}C NMR spectrum of pure C_{60} in deuterated benzene, C_6D_6 . (b) UV-vis spectra of C_{60} and C_{70} in hexane.

1.1.2 One-dimensional carbon

One-dimensional carbon nanomaterial has the linear carbon structure. Iijima and Ichihashi, pioneer of carbon nanomaterial research, synthesized single-walled and multi-walled carbon nanotubes. This carbon nanotube is also composed from rolled-up graphene sheet. The chirality of the single walled carbon nanotubes (SWCNTs) relates to the angle at which the graphene sheets roll up, and hence the alignment of the π -orbital as shown in Fig 1.3. Carbon nanotube can be largely categorized as zigzag, armchair, and chiral structure. Dresselhaus *et al.* described SWNTs in terms of the tube diameter (d) and its chiral angle (θ).³² The chiral vector (C_h) was defined in terms of the graphene sheet lattice translation integer represents (n, m) and the unit vectors (a_1, a_2), and it is defined as follows:³³

$$\vec{C}_h = n\vec{a}_1 + m\vec{a}_2$$

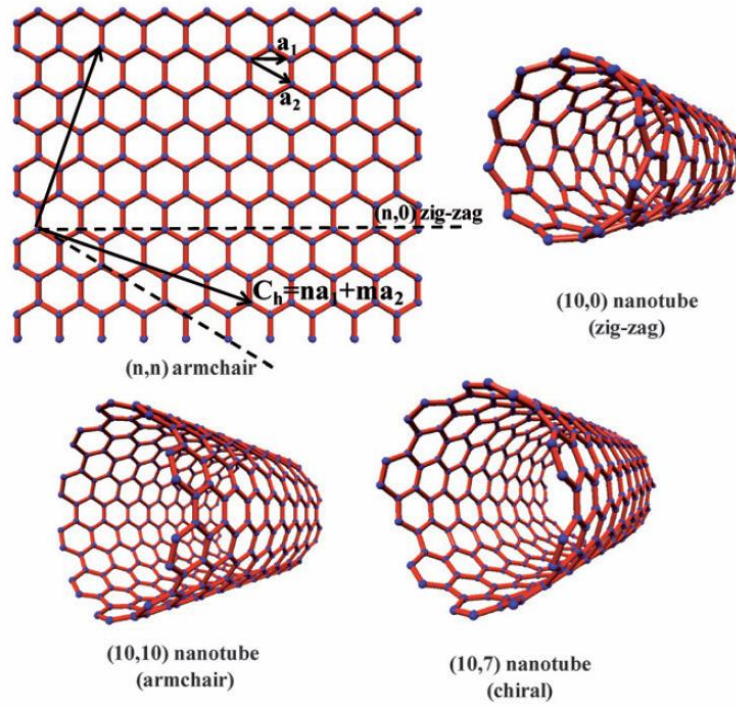


Fig 1.3 Schematic image of armchair (n, n) , zig-zag $(n, 0)$, and chiral (n, m) carbon nanotube structure. (n, m) is chiral integer

Important factor is chiral integer (n, m) because it can be determinant for metallic or semiconducting carbon nanotubes. Metallic nanotubes are achiral and in the armchair configuration with indexes (n, n) , while chiral (n, m) and achiral zigzag $(n, 0)$ tubes are semiconducting unless the vector indexes give a whole number when the calculation $(n - m)/3$ is performed.

The scanning tunnel microscopy (STM) experiments give a direct experimental probe of the electronic density of states (DOS) near the Fermi level.³⁴ Metallic and semiconducting SWCNTs has been also investigated by DOS analysis. Besides, the DOS in the Fermi level of all carbon nanotubes can be expressed in terms of a universal function $U(E')$:

$$U(E') = \frac{2\sqrt{3}}{\pi^2} \sum_{m'=-\infty}^{\infty} g(E', \epsilon'_{m'}),$$

where, $g(E', \epsilon'_{m'})$ is universal integer factor, therefore DOS of universal function for metallic or semiconducting carbon nanotube can be solved by this universal relationship.³⁵

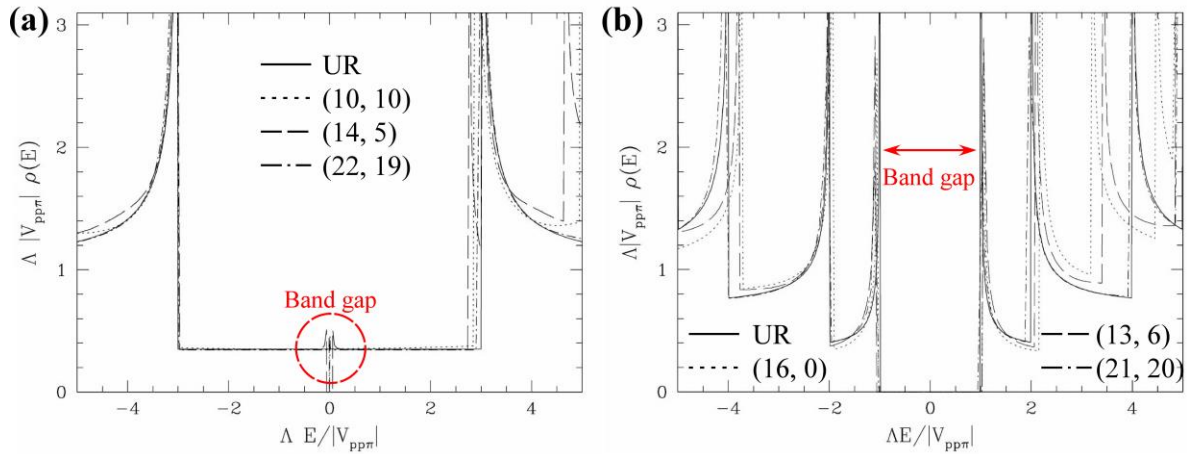


Fig 1.4 Comparison of scaled first-principles DOS universal relationship for (a) metallic and (b) semiconducting SWCNT with different chiral integer.

Fig 1.4a shows DOS analysis of SWCNTs with universal relationship. As a result, DOS for the metallic and achiral universal relationship can be reproduced with results of (10, 10), (14, 5), and (22, 19) SWCNTs, in which is calculated by first-principle calculation for “the $n_1 - n_2 = 3q$ ”. For increasing the diameter of tubes, the band gap decreased to zero as property of zero-band gap semi-conductor. In case of the “ $n_1 - n_2 \neq 3q$ ” as represented Fig 1.4 (b), SWCNT with (16,0), (13,6), and (21,20) chirality shows similar DOS from first-principle calculation. Simple calculation chiral integer, which is divided with $(n - m)/3$ calculation for metallic or semiconducting SWCNTs, corresponds with first-principles DOS universal relationship.³⁶

The other one-dimensional carbon nanomaterial has multiple carbon-hydrogen bond. Fig 1.5 (a) shows various carbon-hydrogen alloys for diagram of $sp^2 - sp^3$ for carbon orbital with amount of hydrogen. Among these hydrogenated carbons, polyacetylene has the attractive properties such as high conductivity and thermal stability in Fig 1.5 (b).³⁷ In 1977, polyacetylene, which is synthesized by Natta *et al.*, has definite advantage on electrical application.³⁸ An unusual structure of poly acetylene that consists of single bond and double

bond between carbon atoms has a high conductivity by ionic donor-acceptor interaction through the doping. In summary, the one-dimensional carbon nanomaterials have various electrical properties with the aid of carbon bond. From the viewpoint of electrical property, one-dimensional carbon nanomaterial is used as metallic and semiconducting applications.³⁹

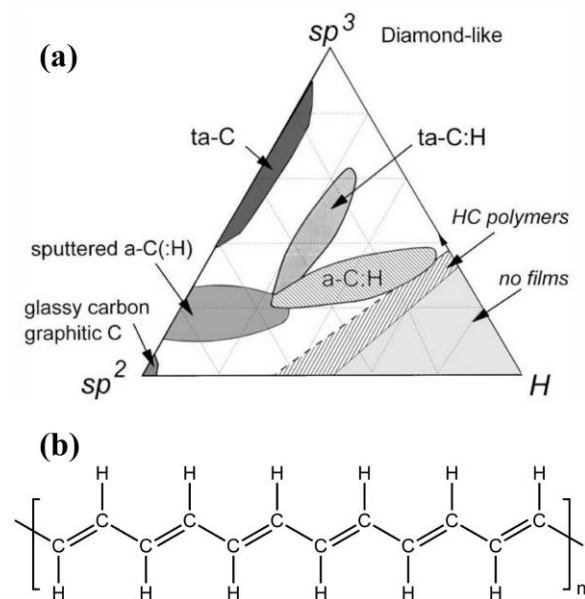


Fig 1.5 (a) Ternary phase diagram of bonding in amorphous carbon-hydrogen alloys. (b) Molecular structure of trans-poly acetylene molecule.

1.1.3 Two-dimensional carbon

Most of two-dimensional carbon nanomaterials have the graphene structure, which is composed of hexagonal lattice. This graphene structure is composed of carbon sp^2 hybridization which continually connect the single and double bond through π -conjugated system. Moreover, the graphene structure has a triangular lattice with a basis of two atoms per unit cell. The lattice vector is defined as

$$\vec{a}_1 = \frac{a}{2}(3, \sqrt{3}), \vec{a}_2 = \frac{a}{2}(3, -\sqrt{3})$$

where $a = 1.42 \text{ \AA}$ is distance between carbon to carbon as shown in Fig 1.6 a.

The reciprocal-lattice vectors are written as

$$\vec{b}_1 = \frac{2\pi}{3a}(1, \sqrt{3}), \vec{b}_2 = \frac{2\pi}{3a}(1, -\sqrt{3})$$

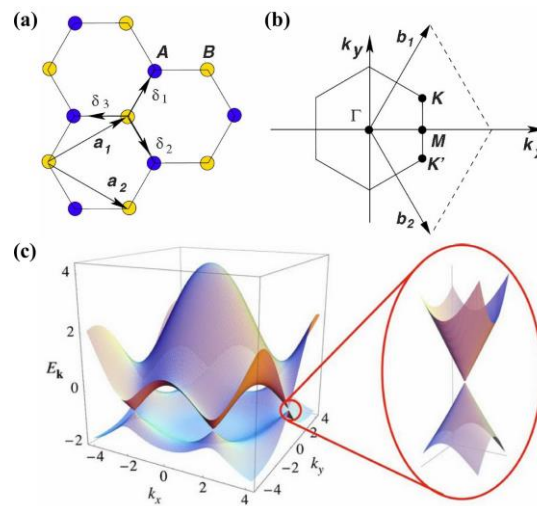


Fig 1.6 (Top) Honeycomb lattice and its Brillouin zone. Left: lattice of graphene (a_1 and a_2 are the lattice unit vectors, and $\delta_i, i=1, 2, 3$ are the nearest-neighbor vectors). Right: corresponding Brillouin zone. (Bottom) Electronic dispersion in the honeycomb lattice. Left: energy spectrum (in units of t). Right: zoom in of the energy bands close to one of the Dirac points.

In particular, two points K and K' are located at corners of Brillouin zone graphene, and given as Dirac points by

$$K = \left(\frac{2\pi}{3a}, \frac{2\pi}{3\sqrt{3}a} \right), K' = \left(\frac{2\pi}{3a}, -\frac{2\pi}{3\sqrt{3}a} \right)$$

Fig 1.6 (c) shows full band structure of graphene with t (≈ 2.8 eV) and t' which are the nearest-neighbor hopping energy and next nearest-neighbor hopping energy, respectively.⁴⁰ Close to Dirac point ($t' = 0$), the electron-hole nature is apparent in density of states per unit cell. These conjugation and electron-hole can enhance the electron transfer and charge transfer.^{41,42} Besides, graphene has attracted a lot of attention for properties such as charge transport. On the basis of the properties, graphene can be used as sensor, transistor, electrode, and energy storage device.^{43,44} Recently, graphene dispersion is used as printing material in 3D printer.⁴⁵

1.1.3 Three-dimensional carbon nanomaterial

An example for three-dimensional carbon nanomaterials is diamond and graphite structure as shown in Fig 1.7. In 1772, Antoine Lavoisier showed that the combustion product of the diamond was only carbon dioxide, therefore diamond consists of only elemental carbon.⁴⁶ Later 1797, Smithson Tennant demonstrated that burning of same amount of diamond or graphite leads to production of the same amount of carbon dioxide gas, proving that diamond and graphite have the equal quantity of elemental carbon, but resulting in different structure.⁴⁷ After development of spectroscopy, the structure of diamond was elucidated as the tetrahedral sp^3 structure by X-ray photoelectron spectroscopy.⁷ On the other hand, graphite has trigonal planar sp^2 carbon with p-orbital for π -bonding. The structure of graphite consists of strong covalent bond in-plane direction and weak intermolecular force out-of-plane direction as shown in Fig 1.7. To synthesize the diamond, many researchers adopted the high temperature and high pressure method. Consequently, commercial application is possible because of these methods.⁹ Majority of property for diamond is strong hardness, so diamond has been used as diamond cutters. In addition, diamond is used as electrical insulators.⁴⁸

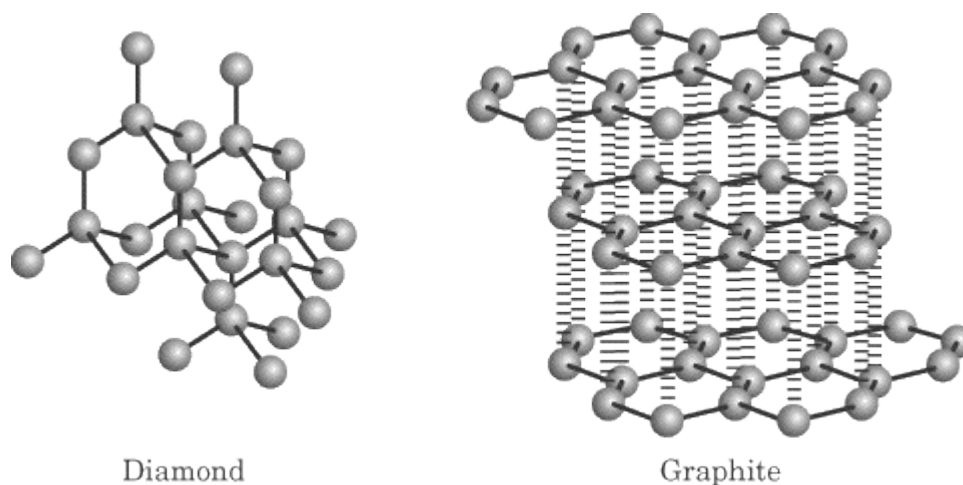


Fig 1.7 Schematic illustration of the structure for diamond and graphite. Solid line and dotted line are strong covalent bond and weak intermolecular force.

1.2 Various synthesis techniques

Carbon nanomaterials such as graphene, graphitic carbon, SWCNTs, and multi-walled carbon nanotubes (MWCNTs) can be synthesized by various synthesis methods on catalysts. For example, since the report by K.S. Novoselov *et al.*, graphene has been studied on its characterization and synthesis technique.^{49,50} Since the Iijima's study, synthesis for helical microtubules of graphitic carbon has been employed with the arc discharge evaporation.⁵¹ Reina *et al.*, reported that graphitic carbon could be synthesized by chemical vapor deposition on the metal films.⁵² In case of the polyacetylene synthesis, most of catalyst for polymerization reported so far involves Ziegler-Natta catalysts that consist of organoaluminum and metallocene complex.³⁸ Therefore, many researchers have adopted the various synthesis methods. To verify the detail in synthesis methods, next I introduce the detailed mechanism, condition, and advantage in this section.

1.2.1 Arc discharge synthesis

Various techniques of carbon nanotube synthesis have been widely investigated aiming for high yield and low energy consumption condition. By the early 1990s, Iijima synthesized carbon nanotube by arc discharge process using huge current (~ 100 A) and Fe catalysts as shown in Fig 1.8 (a).⁵⁰ Arc discharge is a method, in which two electrodes are placed in a container under helium or argon gas atmosphere.⁵³ A high current is passed through the circuit closed by an arc between two electrodes. Carbon can be vaporized above 3000 °C, and product is subsequently deposited on the cathode electrode. Using this method, yield is up to 30 % by weight. In addition, length of synthesized nanotubes is about 50 μm with few structural defects. According to Iijima's research, product is obtained as SWCNTs and MWCNTs as shown in Fig 1.8 (b). However, selective synthesis such as only SWCNTs or MWCNTs is still difficult for arc discharge system.

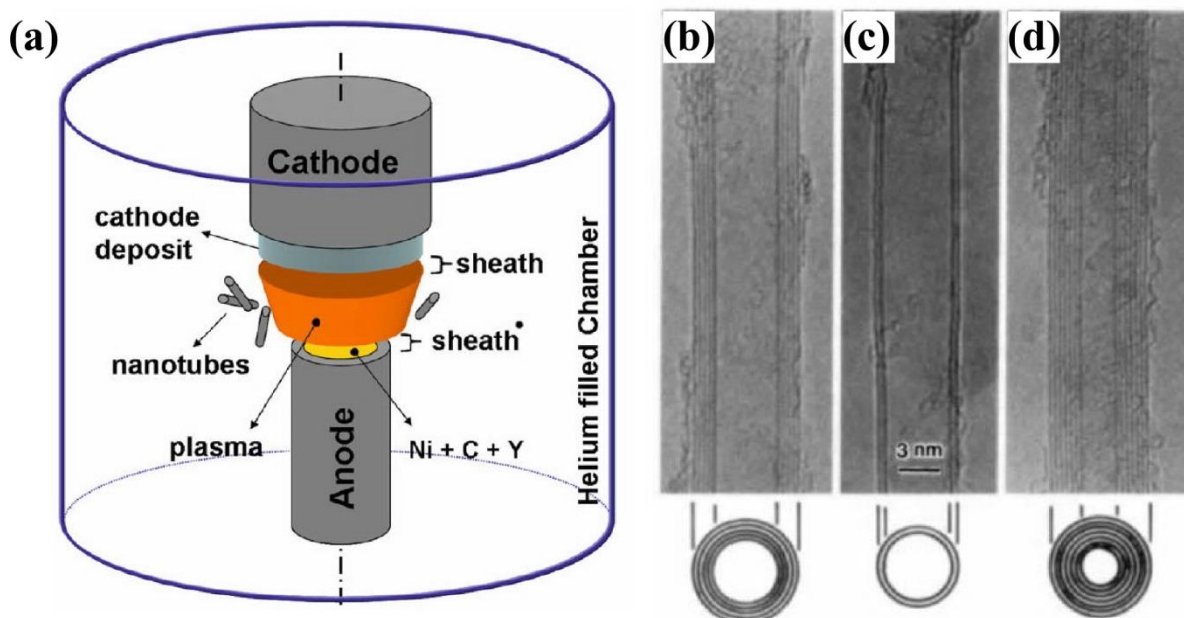


Fig 1.8 (a) Schematic illustration of arc discharge system. Electron micrographs of (b) SWCNT with diameter 6.7 nm, (c) double walled carbon nanotube with diameter 5.5 nm, and (d) seventh walled carbon nanotube with diameter 6.5 nm using arc discharge synthesis.

1.2.2 Laser ablation synthesis

To increase the yield for pure SWCNTs, Guo *et al.* synthesized the SWCNTs by a laser impinging on a metal-graphite composite target to induce vaporization of mixture of carbon and transition metals (Fig 1.9).⁶ In laser ablation, a pulsed laser vaporizes a graphite target in a high-temperature reactor (above 1200 °C) while an inert gas is bled into the chamber. Nanotubes are grown on the cooler surfaces of the reactor as the vaporized carbon condenses. Fig 1.9 (b-e) is TEM images of Co/Ni-catalyzed nanotube material deposited on the cold copper collector with high-yield. SWCNTs were typically found bundle formation, in which many tubes found together in van der Waals contact over most of their length. This bundle formation requires very high density of SWCNTs in the gas phase to have collided and aligned prior to landing on the cold collector. Besides, very little carbon particle is available for coating the SWCNTs before this alignment. The laser ablation method yields around 70% and produces primarily single-walled carbon nanotubes with a controllable diameter determined by the reaction temperature. However, instrument of laser ablation is more expensive than arc discharge system.⁵⁴

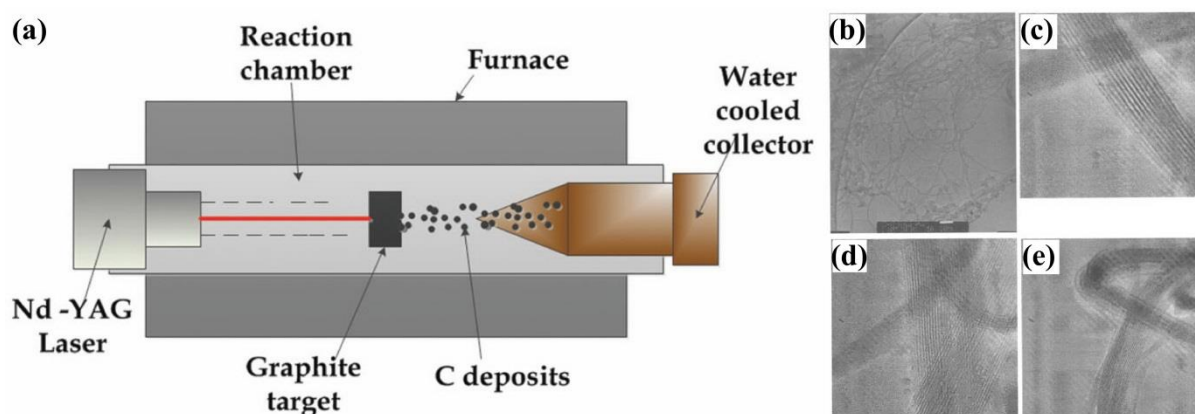


Fig 1.9 (a) Schematic illustration of laser ablation. Transmission electron micrograph (TEM) of SWCNT at (b) medium magnification view and (c-e) high magnification view

1.2.3 Chemical vapor deposition (CVD)

To improve synthetic techniques toward the high quality of carbon nanomaterial, Zhao *et al.* adopted the graphene synthesis by chemical vapor deposition using ethanol as carbon precursor.⁵⁵ The CVD of various hydrocarbon gases on transition metal catalysts is successful for obtaining graphene and carbon nanotube.⁵⁶ During the synthesis (Fig 1.10 (a)), ethanol precursor decomposes into different products as carbon suppliers at high temperature of 1000 °C. And then, activated species of carbon is chemically adsorbed on the copper surface. Because the activation energy of surface diffusion of carbon on copper is low (~ 0.06 eV), activated species of carbon is easily diffuse and aggregate on the active surface of copper to provide nucleated carbon island. Finally, crystal growth of graphene over nucleated carbon island by supplied carbon source resulted in formation of graphene. Fig 1.10 (b) shows the scanning electron microscope (SEM) image of graphene on the copper surface after 10 min growth from ethanol. As a result, domain boundaries of graphene are formed on copper. In addition, Raman spectra of graphene show the D band, G band, and 2D band,

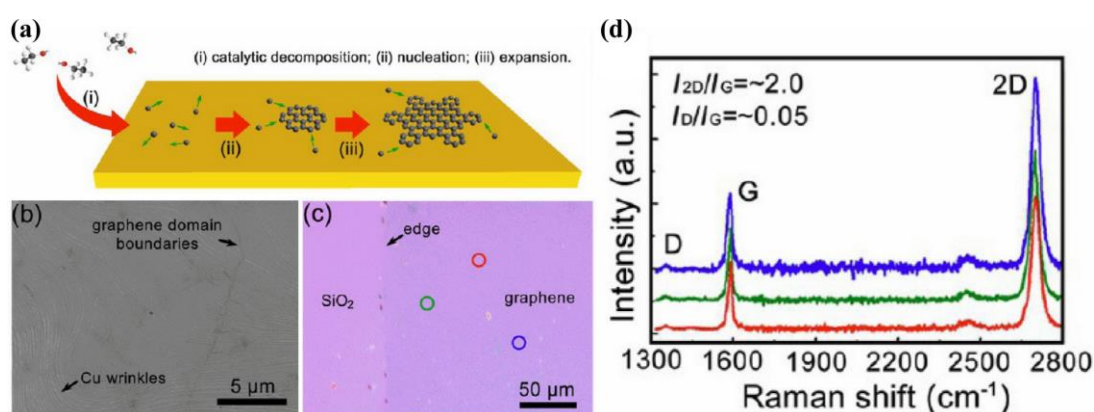


Fig 1.10 (a) Schematic of the initial state of the growth of graphene on copper from ethanol. (b) Scanning electron microscopy (SEM) image of graphene on the copper after 10 min of growth from ethanol. (c) Optical micrograph and (d) Raman spectra of graphene at different position.

which originates the graphene structure in Fig 1.10 (c and d). I explain the detail D band, G band, and 2D band of Raman spectroscopy next section (Section 1.3.2).

Carbon synthesis can be controlled by transition metal catalysts such as Ni, Co, and Fe, that is advantage of the CVD technique. In terms of activation energy for growth of SWCNTs and carbon nanofibers (CNFs), Hofmann *et al.* reported temperature-dependency on SWCNTs growth as shown in Fig 1.11.⁵⁷ In the 250-500 °C range, the growth rates are very similar with Ni and Co catalyst, whereas it is lower with Fe catalyst. Nevertheless, it is clear that activation energy is always below 0.4 eV. For the fundamental processes, CNT or CNFs is grown on a metal particle as followed; (1) adsorption of gas precursor molecule on catalyst surface, (2) dissociation of precursor molecule, (3) diffusion of the growth species, and (4) nucleation and incorporation of carbon into growing structure. The barrier for C₂H₄ or CH₄ dissociation on the catalyst interface exceeds 0.9 eV on Ni (111) planes or edges. Therefore, the activation energy for thermal growth must be at least as high as the barrier for gas decomposition.

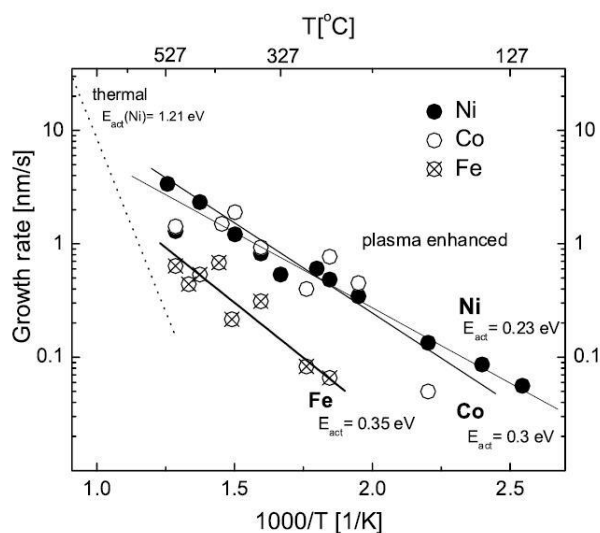


Fig 1.11 Arrhenius plots for carbon nanofiber growth rates on different catalysts in NH₃ diluted C₂H₂. The activation energies are calculated from the slope of the linear fit to the data. The dotted line is the growth rate variation for Ni thermal CVD.

General CVD methods suffer from the production of impurities which potentially damage the nanotubes. Therefore, impurities must be removed in purifications steps by weak oxidizer. Dispersion of SWCNTs in dispersion for further processing also presents challenges because the smooth-sided tubes readily aggregate and form parallel bundles or ropes as a result of van der Waals interactions. To solve this problem, Hata *et al.* demonstrated the addition of a controlled amount of water vapor in the growth atmosphere because of preserving the catalysts, resulting in enhancement of activity and lifetime for catalysts.⁵⁸ Fig 1.12 shows SWCNTs forest grown with water-assisted CVD. Synthesized SWCNTs have 2.5 mm height in a 10 min growth time. The production efficiency is about 100 times higher than for the laser ablation method. In case of the SEM image (Fig 1.12 (c)), nanotubes are densely packed and vertically aligned from the substrate. In addition, TEM images of nanotubes show the presence of thin nanotubes and the absence of metallic particles as shown in Fig 1.12 (d) and (e). Water-assisted CVD is possible for large-scale synthesis of SWCNTs.

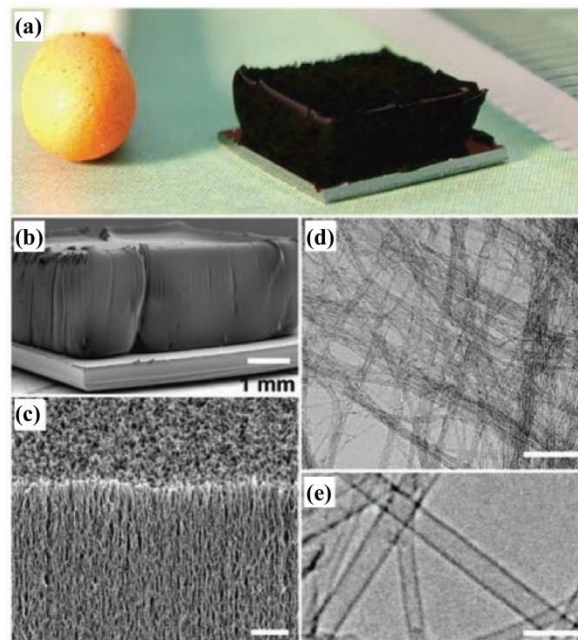


Fig 1.12 (a) Photograph of a 2.5 mm-tall SWCNTs forest. (b) SEM image of the same SWCNTs forest. (c) SEM image of the SWCNTs forest ledge. (d) low- and (e) high-resolution TEM image.

To evaluate the growth process, Yoshida *et al.* showed *in-situ* environmental transmission electron microscopy (ETEM) observation of the nucleation and continuous growth of SWCNTs in Fe-catalyzed CVD.⁵⁹ As a result, carbon nanotubes are grown from nanoparticle catalysts (NPCs) of fluctuating crystalline iron carbide (FeC_x) as represented in Fig 1.13. Before the nucleation of SWCNT, a NPC exhibits different facets every frame ($t = 8.05$ and 16.45 s), as shown in Fig 1.13 (a). And then, carbon cage is formed on NPC at $t = 29.05$ s. After incubation period, the stable dome or nucleus of a SWCNT appears at $t = 35.35$ s. After nucleation, SWCNT is gradually grown after $t = 38.5$ s. In case of the snapshot of a NPC with a carbon dome, carbon is grown up on the lattice site of a NPC in Fig 1.13 (b). Structural control of SWCNT is possible by preparing NPCs with the proper structures on substrates.

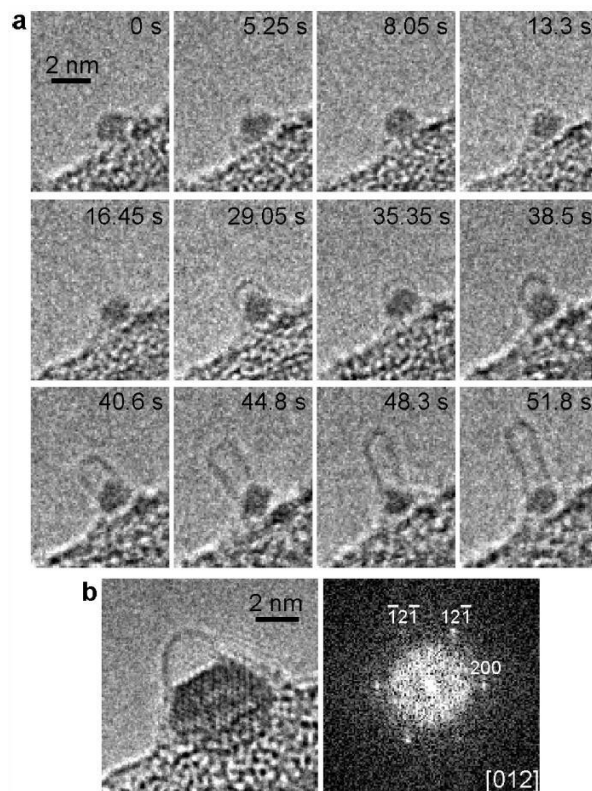


Fig 1.13 Nucleation and growth process of a SWCNT from a nanoparticle catalyst (NPC) on a substrate. (a) Structural fluctuation of both carbon caps. (b) A snapshot of a NPC with carbon dome

1.2.4 Electrochemical deposition

Electrochemical deposition is a process that requires electric current to reduce dissolved cations in the electrolyte, and then deposited material can be coated on the working electrode in the electrolyte as represented in Fig 1.14.⁶⁰ Recently according to published reports by Shawky *et al.*, demonstrated electrochemical deposition of SWCNT from acetic acid in aqueous electrolyte solution over Ni nanocatalysts supported by Au surface at room temperature.⁶¹ This system has the attractive features such as relatively inert reaction conditions than CVD, uniform and compact deposition on the template-based structure, and faster deposition rate than thermal deposition.

Namba *et al.* reported that diamond phase film was fabricated by electrochemical deposition from ethanol at -1.2 kV for 70 °C on the Si substrate. As a result, diamond powder was deposited about 0.12 μm thickness on the Si substrate for 12 h.⁶² To reduce the applying voltage and requiring time, Gupta *et al.* reported that diamond like carbon synthesis by electrochemical deposition using acetic acid and H₂O at 3 V for 85 °C and 30 min.⁶³ Especially, to enhance the activity of electron field emission, nitrogen- and sulfur-doped diamond like carbon could be synthesized by electrochemical reduction of urea as nitrogen precursor and carbon disulfide as sulfur precursor at 1 kV for 75 °C and 30 min on the Si substrate.⁶⁴ Ling *et al.* synthesized the iron- and cobalt-doped diamond like carbon film by electrochemical deposition on the Si substrate from Fe(II) acetylacetonate and Co(II) acetylacetonate as iron and cobalt precursor, respectively (synthesis condition is 1 kV, 75 °C, and 40 min).⁶⁵ In consideration of these results, electrochemical deposition is widely used as sensitive and selective synthesis method for many cations in electrolyte on the catalyst.

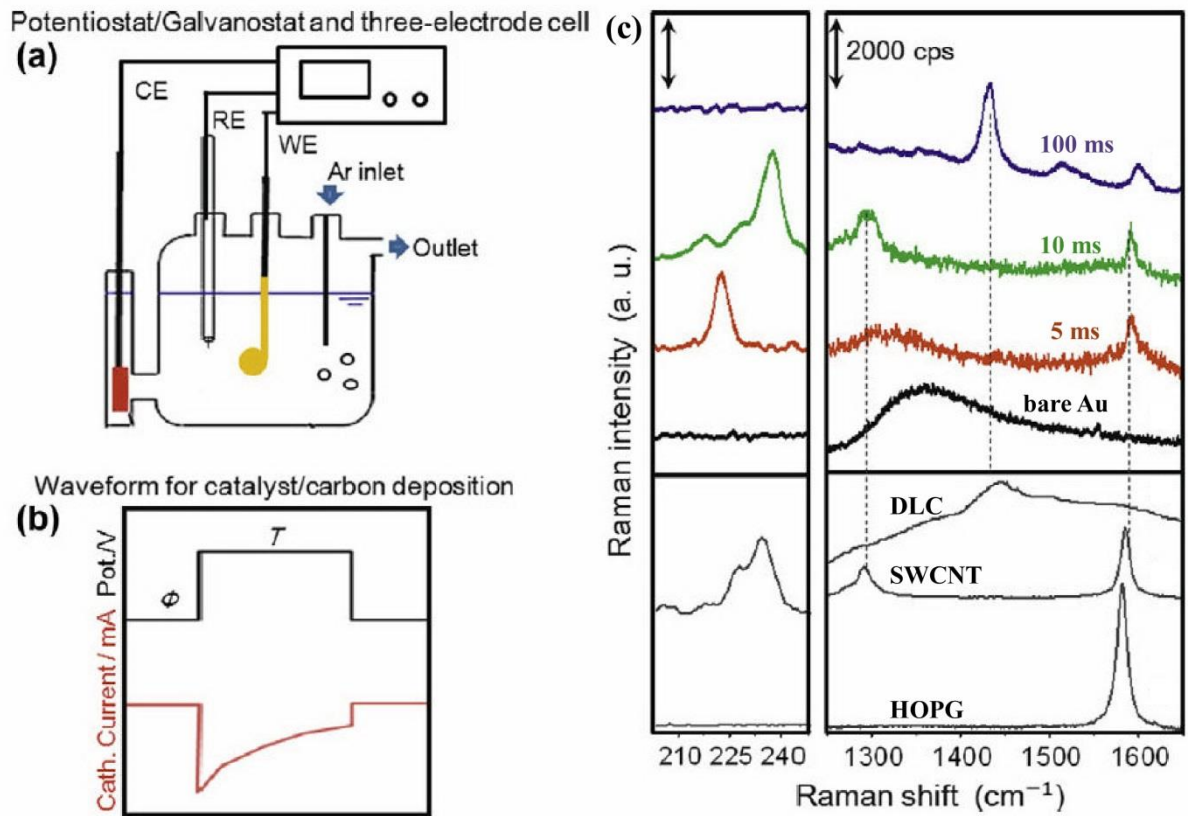


Fig 1.14 (a) Schematic image of experimental setup for electrochemical deposition and (b) bias/current waveforms generated for deposition. (c) Raman spectra of HOPG, commercial SWCNT, DLC film, bare Au surface, and over Au supporting Ni nanoparticles deposited for 5, 10, and 100 ms.

1.3 Characterization method

1.3.1 Raman spectroscopy

Raman spectroscopy is vibrational spectroscopy based on the inelastic scattering of laser through the interaction with matter that provides the information about identification of molecular species as shown in Fig 1.15.⁶⁶ The difference in energy (or wavelength) of the scattered light from a material originates in characteristic of a particular bond in its molecular structure. In other words, to evaluate the binding energy, relationship is followed as;

$$\nu_{\text{laser}} - \nu_{\text{scattered}} = \nu_{\text{Raman}}$$

The binding energy of molecules from this Raman binding energy can be evaluated by experimental factor. Therefore, the unique various energy shifts associated with different molecular vibrations leads to a Raman spectrum.⁶⁷

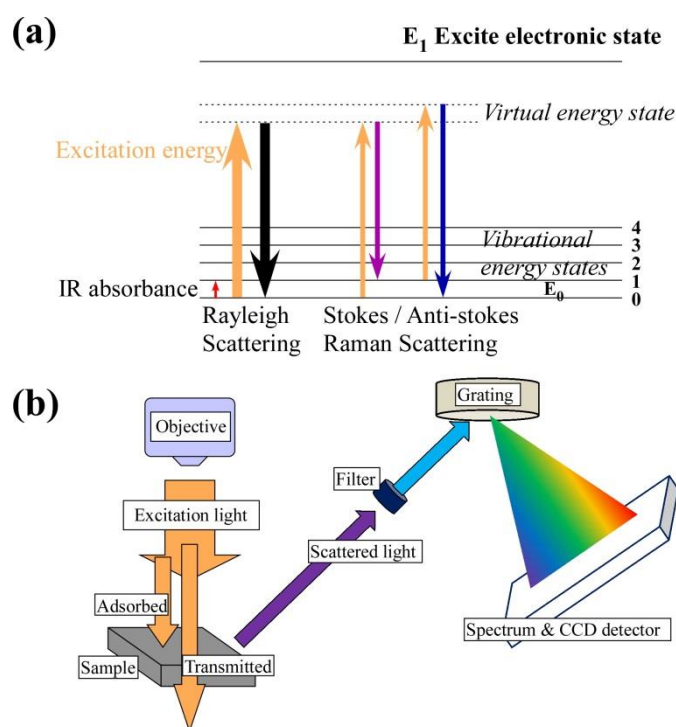


Fig 1.15 (a) E_1 excite electronic state for Rayleigh scattering, strokes, and anti-strokes Raman scattering. (b) Schematic image for process involved in collecting Raman spectra.

1.3.2 Raman spectra for carbon allotropes

Due to the different binding energy of phonon modes in carbon allotropes, Raman spectroscopy also can be verified their structures. Especially, G band, D band, and 2D band, are important diagnostic feature in Raman spectrum for carbon allotropes as shown in Fig 1.15.⁶⁸ At first, G band is well known Raman mode in single crystalline graphene of six-membered carbon stretching mode, which corresponds to the in-plane, zone center, doubly degenerate phonon mode with E_{2g} symmetry. This G band has a single peak at 1580 cm^{-1} arising from tangential mode.⁶⁹ Next, D band is sp^2 disordered graphene at around 1350 cm^{-1} . This D band originates from the defect site and edge site of graphene structure. D band and 2D band come from second-order double resonant process between nonequivalent K points in the Brillouin zone of graphene. Especially, SWCNTs have the radial breathing mode (RBM) from 100 to 350 cm^{-1} . In the RBM of Fig 1.15 bottom, its frequency ν_{RBM} depends on the nanotube diameter. MWCNTs do not have RBM peaks because RBM is interrupted by multi-wall. Therefore, SWCNTs should be appeared to RBM peaks.⁷⁰

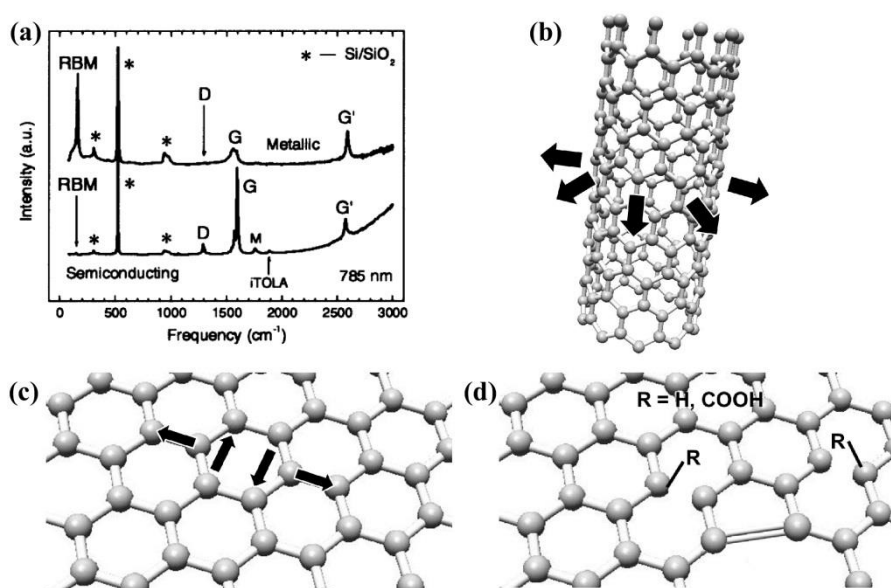


Fig 1.16 (a) Raman spectra for metallic and semiconducting SWCNTs. Bond structures of (b) RBM, (c) G band, and (d) D band.

1.3.3 Atomic force microscopy (AFM)

Atomic force microscopy (AFM) is microscope for sample surface using physical probe of tip and cantilever. When the tip and cantilever are tapped by roughness of sample during measuring process, laser can detect the vibration of tip, and then sample image is mapped via position-sensitive detector (PSD) as represented in Fig 1.17.⁷¹ Forces between the tip and the sample lead to a deflection of the cantilever according to Hooke's law. Imaging modes have the 3 modes such as contact mode, tapping mode, and non-contact mode. The contact mode is dragged across the sample surface. Tapping mode is used to evaluate the close to the sample. Non-contact mode is that the tip of the cantilever does not contact the sample surface, and it just measured the *van der Waals* forces from 1 to 10 nm.⁷²

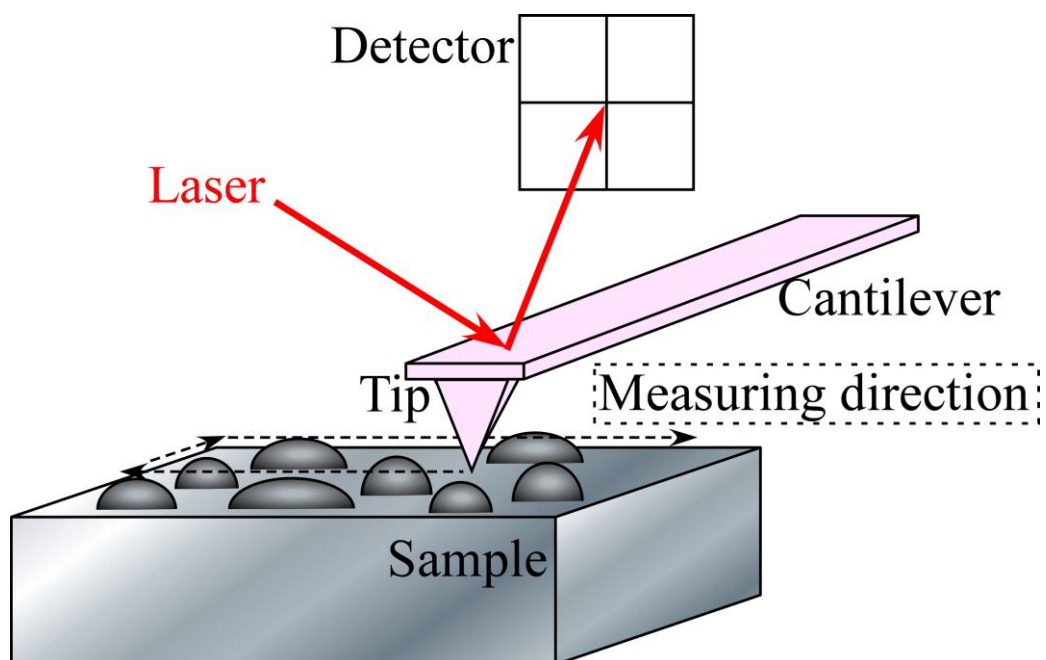


Fig 1.17 Schematic image of AFM measurement.

1.3.4 Specific surface area analysis

Pore size is important factor from viewpoint of specific surface area. In general, pore size distribution can be classified to micro-porous (< 2 nm), meso-porous (2~50 nm), and macro-porous (> 50 nm) distribution as shown in Fig 1.18 (a). Pore size distribution analysis is conducted by gas adsorption and desorption measurement at low temperature. For example, nitrogen gas can strongly adsorb on the porous solid surface until the formation of monolayer. And then, after the saturation of monolayer, nitrogen gas is weakly adsorbed on the nitrogen monolayer because interaction between nitrogen and nitrogen is weaker than nitrogen to solid surface as shown in Fig 1.18 (b). Therefore, specific surface area, which is total surface area of material per unit of mass, can be evaluated by using this principle.⁷³

The micro porous size and distributions are evaluated by BET (Brunauer–Emmett–Teller method).⁷⁴ BET method assumes that molecules of multi-layer are gained by infinitely overlapping adsorption on the molecule of mono-layer, and intermolecular interaction is absence. A BET equation follows as;

$$\frac{1}{v\left[\left(\frac{P}{P_0}\right) - 1\right]} = \frac{C - 1}{v_m C} \left(\frac{P}{P_0}\right) + \frac{1}{v_m C}$$

where, p and p_0 are equilibrium and the saturation pressure of adsorbates at the temperature of adsorption, v is the adsorbed gas quantity, v_m is the monolayer adsorbed gas quantity and C is the BET constant.

In the range of $0.05 < p/p_0 < 0.35$ (micro porous region), adsorption isotherm can be plotted as a straight line in Fig 1.18 (c). The slope A and the y-intercept I of the line are used to calculate the v_m and C as following;

$$v_m = \frac{1}{A+I}, c = 1 + \frac{A}{I},$$

Finally, total surface area (S_{total}) and specific surface area (S_{BET}) is evaluated by

$$S_{total} = \frac{v_m N_s}{V}, S_{BET} = \frac{S_{total}}{a},$$

where N is Avogadro's number, V the molar volume of the adsorbate gas

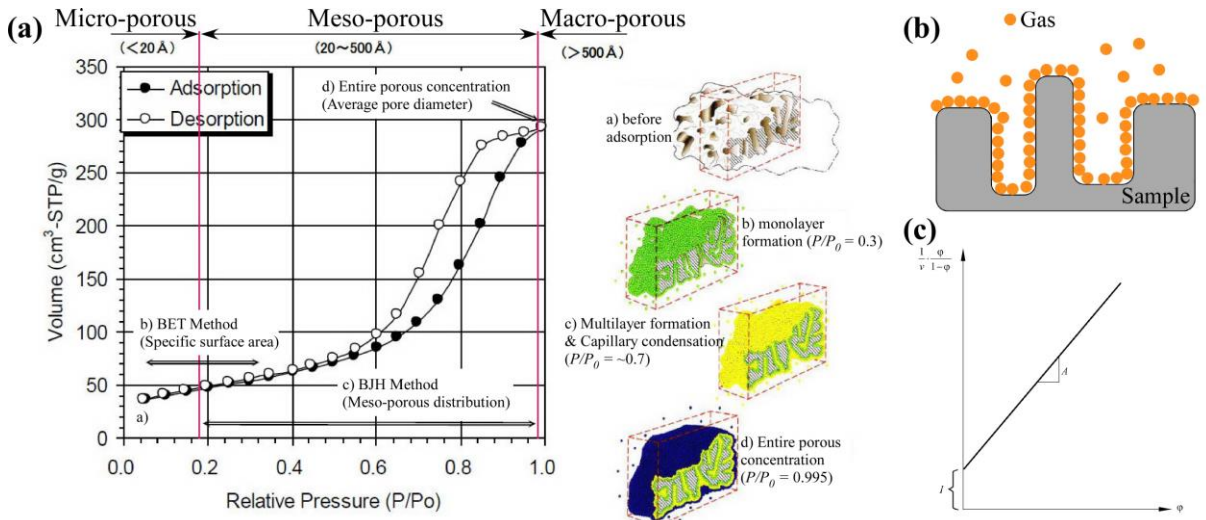


Fig 1.18 (a) Adsorption-desorption isotherm of porous structure at low temperature. (b) Schematic illustration of the adsorption of gas (c) BET plots of adsorption-desorption isotherm.

1.3.5 X-ray photoelectron spectroscopy (XPS)

XPS is a surface characterization technique that can be used for the surface chemistry of material in vacuum. Because the specific energy of X-ray source is known with particular wavelength (for Al K α X-rays, $E_{\text{photon}} = 1486.7$ eV) and the emitted electrons' kinetic energies can be measured, the electron binding energy of each of the emitted electrons can be determined by using an equation as shown in Fig 1.19;⁶⁹

$$E_{\text{binding}} = E_{\text{photon}} - (E_{\text{kinetic}} + \phi)$$

where E_{binding} is the binding energy (BE) of the electron, E_{photon} is the energy of the X-ray photons being incident light, E_{kinetic} is the kinetic energy of the electron as measured by the instrument, and ϕ is the work function dependent on both the spectrometer and the material. This equation is essentially a conservation of energy equation. The work function term ϕ is an adjustable instrumental correction factor that accounts for the few eV of kinetic energy given up by the photoelectron as it becomes absorbed by the instrument's detector.⁷⁵

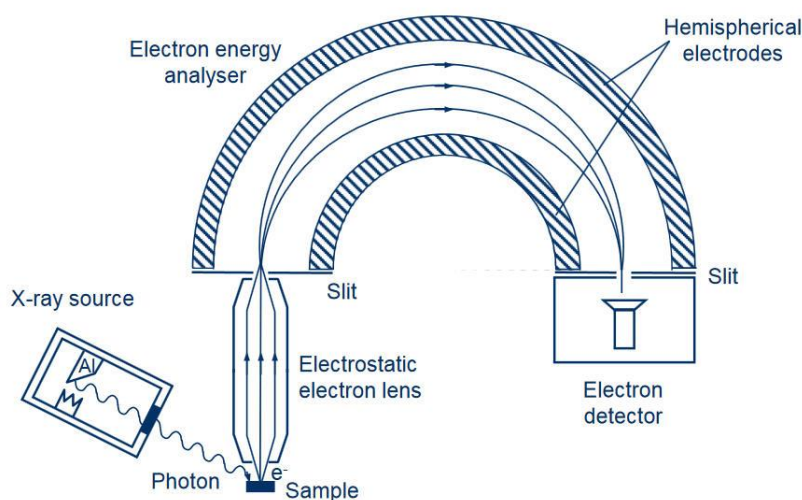


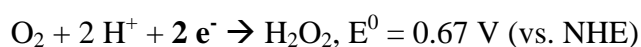
Fig 1.19 Basic components of a monochromatic XPS system.

1.4 Electrocatalysts for carbon based material

1.4.1 Oxygen reduction reaction (ORR)

Electrochemical catalyst is used as many applications for electrochemical conversion system. Among these applications, polymer electrolyte membrane fuel cell has come into spotlight to convert the chemical energy stored in hydrogen fuel to electrical energy with water. In this system, oxygen reduction reaction (ORR) occurs on cathode electrode as shown in Fig 1.20 (a) and (b).⁷⁶ In the ORR, electrocatalysis proceed with two pathways such as two-electron reaction and four-electron reaction, and following the reaction formula.^{77,78}

<Acidic aqueous solution>



<Alkaline aqueous solution>

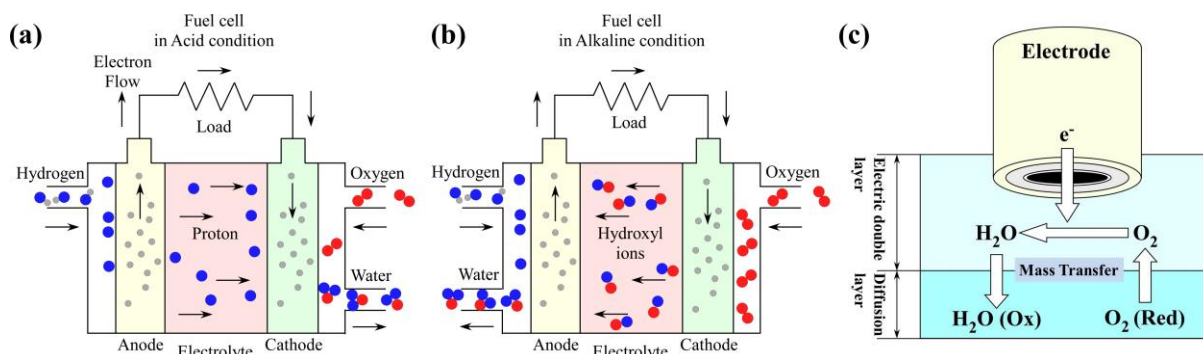


Fig 1.20 Schematic image of the fuel cell in the (a) acid and (b) alkaline electrolyte. (c)

Oxygen reduction reaction on the rotation ring disk electrode.

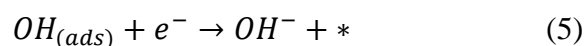
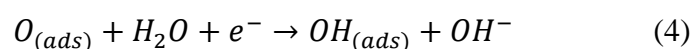
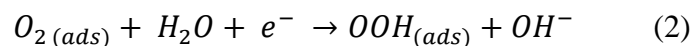
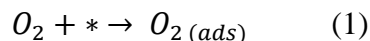
Two-electron reaction produces the hydrogen peroxide, it is tremendous oxidizing agent. This hydrogen peroxide can potentially oxidize cathode easily. Therefore, four-electron reaction is important factor for ORR process. For example, reaction electron number of commercial Pt/C catalysts is near to 3.9 in acidic aqueous solution, while reaction electron number of commercial carbon nanotube is relatively decreased ranging from 3.0 to 3.5.^{79,80}

In general, mass transfer occurs accompanying with the electrode reaction, and then charge polarization appeared on the electric double layer because electrode has the negative charge. As a result, mass transfer limitation is caused by this polarization as shown in Fig 1.20 (c). Therefore, to minimize the double layer charging, rotation disk electrode is adopted for convection system. In addition, ring electrode provides the steady-state method for investigating coupled chemical reaction. Most of rotation ring electrode is platinum, and collects the current density for evolved hydrogen peroxide during ORR process. And then, reaction electron number is estimated by collection efficiency for disk electrode per ring and disk electrode.⁶⁹

In general, Pt-based catalyst has been used as cathode electrode of fuel cell for ORR activity due to its high efficiency.⁸¹ However, large-scale commercial production of this metal has been restricted by its prohibitive cost, limited supply, and weak durability. To improve the problem, nitrogen-doped carbon (N-doped carbon) materials are generally accepted as a potential substitute for Pt to reduce the cost, enhance the stability of ORR electrocatalysts, and then promote the commercialization of fuel cell technology.⁸¹ Many researchers have studied on theoretical and experimental ORR activity for N-doped carbon structure.^{82,83} In particular, ORR activity is changed by N-doped carbon structure such as pyridinic or graphitic N. Yu *et al.* reported nitrogen doped graphene for ORR mechanism using calculation of density functional theory. ORR mechanism in alkaline solution presents two

different mechanisms such as an associative mechanism (i) and a dissociative mechanism (ii).

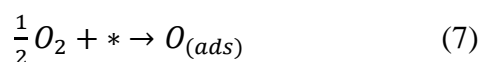
(i) Associative mechanism, which can be described as follows:



where * denotes a free site on the surface. Alternatively, instead of reaction (3), $OOH_{(ads)}$ desorbs from surface,



(ii) Dissociative mechanism, in which the first step is the following:



followed by steps (4) and (5).

To evaluate the two energy profiles for different nitrogen-doped graphene structure, Fig 1.21 shows free energy diagram of ORR on nitrogen-doped graphene through associative and dissociative mechanism. There are different model structure between S1 and S2: in case of the S1, the nitrogen atoms are separated by two carbon atoms, whereas the nitrogen atoms in S2 structure are separated by three carbon atoms. Adsorption site is carbon atom closest to nitrogen atom. As a result, the dissociation barrier of O_2 on these two surfaces is too high, resulting associative mechanism is favored. In case of the associative mechanism, the

removal of $O_{(ads)}$ exhibits the highest barrier i.e. rate-limiting step. Therefore, ORR on nitrogen-doped graphene follows the associative mechanism in alkaline solution and the reaction rate is limited by the $O_{(ads)}$ removal from the surface. Besides, S2 has the lower activation barrier than S1 structure. It is to say that the local concentration of nitrogen atoms on S1 is higher than that on S2, resulting in relatively low ORR activity. Therefore, ORR activity is changed by different form of nitrogen and carbon structure.

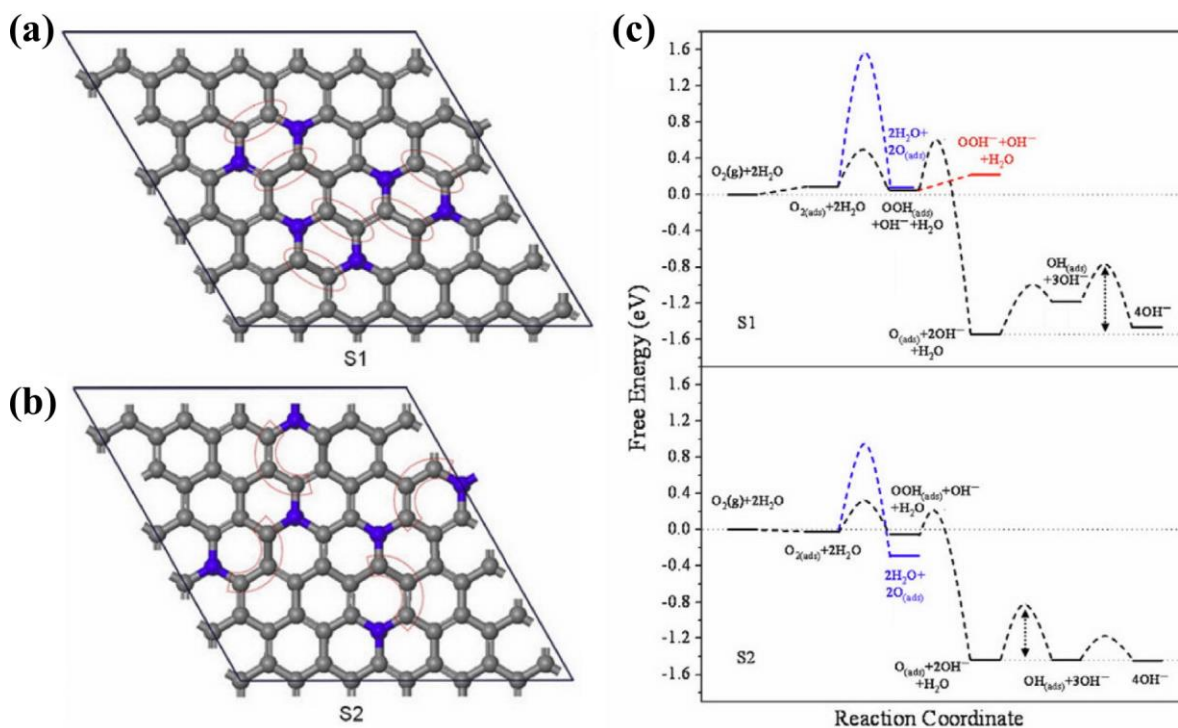


Fig 1.21 Illustration of nitrogen doped graphene structure. N atoms are separated by two C atoms (a, S1) and three C atoms (b, S2). The grey and blue spheres represent C and N atoms, respectively. (c) The free energy diagram for O_2 reduction on S1 and S2 under the condition of 0.04 V and pH = 14. The black line and blue line are intermediates and reaction barrier of associative and dissociative mechanism. The red line indicates the formation of OOH^- .

1.4.2 Oxygen evolution reaction (OER)

Electrochemical water splitting system has come into spotlight to produce the hydrogen fuel due to pollution-free and abundant in reactant.⁸⁴ In this system, hydrogen evolution reaction (HER) and oxygen evolution reaction (OER) can occur on the cathode and anode electrode at the same time as shown in Fig 1.22. According to different media of electrolyte, mechanism of HER and OER can be expressed in different ways;⁸⁵



In acidic solution



In neutral and alkaline solution

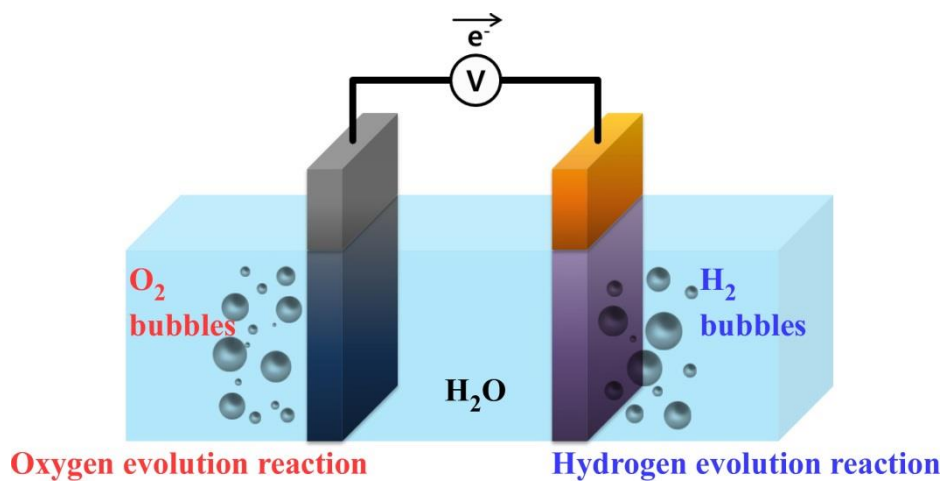
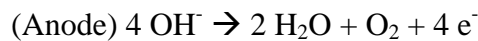
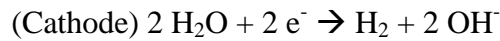


Fig 1.22 Schematic image of electrochemical water splitting system.

On the basis of the thermodynamic study, electrochemical potential for water oxidation is 1.229 V at 25 °C and 1 atm. In particular, OER has the high overpotential because of its higher-number electron reaction. As a result, electrochemical water splitting depends on the OER activity. Therefore, many researchers have studied the reaction mechanism and catalyst for OER.

In general, the majority of catalysts for OER have the noble metal-based oxide such as ruthenium oxide (RuO_2) and iridium oxide due to its inherent activity.⁸⁶ However, it has the commercial limitation because of its high cost and low reserves. To improve the problem, heterogeneous doped porous carbon has been studied to enhance the OER reaction due to its high surface area, and electron conductivity.⁸⁷ Dai *et al.* reported that nitrogen (N) and phosphorous (P) co-doped mesoporous carbon (NPMC) can be synthesized by template-free pyrolysis process as shown in Fig 1.23 (a). As a result, NPMC has the higher surface area than values of previous reported heteroatom doped carbon catalysts. Especially, synthesized NPMC has higher OER activity than Pt/C, and lower overpotential of OER than RuO_2 (Fig 1.23 (b)). Besides, lots of graphitic N and P can induce the OER activity because its high electron transfer activity. For density functional theory calculation, schematic energy profile on N and P co-doped graphene shows in Fig 1.23 (c). All potentials are reported versus the Ag/AgCl. In case of the electrode potential of 0 V, reaction step of the OER is uphill. However, when the electrode potential increases to 0.797 V (0.395 V in overpotential), all the elementary reaction steps become downhill and OER occurs spontaneously over 0.797 V. These results show that the OER is facilitated overall by the N and P co-doped graphene because overpotential of the OER is reduced by N and P co-doping.

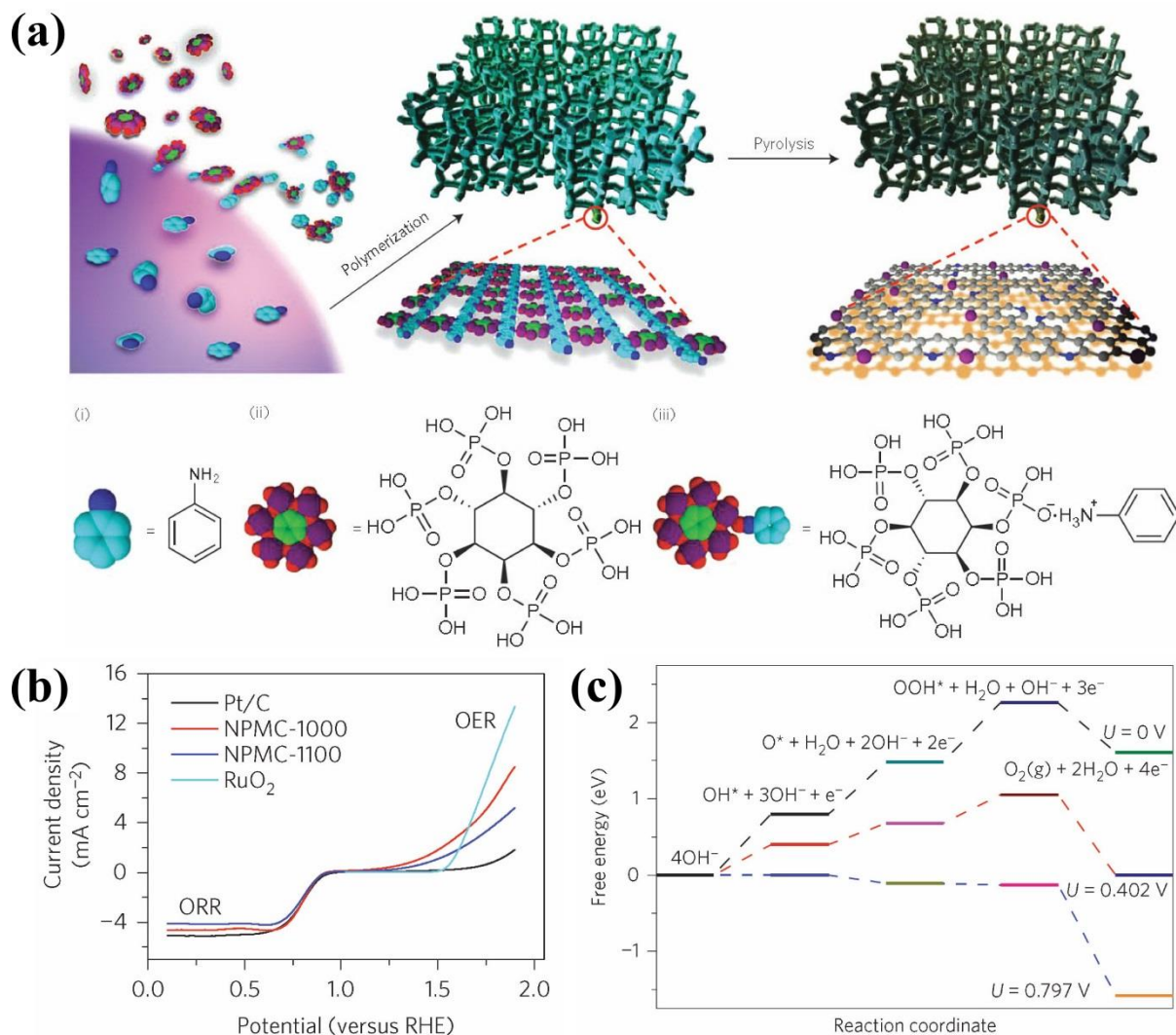


Fig 1.23 (a) Schematic illustration of the preparation process for the N and P co-doped porous carbon (NPMC). (b) Linear sweep voltammograms for NPMCs, Pt/C, and RuO₂. (c) Schematic energy profile for the OER pathway on N and P co-doped graphene in alkaline media.

1.5 Aim of this study

Purpose of this thesis to study the synthesis of carbon nanomaterials and their electrocatalytic applications. First, synthesis of carbon nanomaterials by electrochemical

deposition, and CVD, and pyrolysis method were studied. Different synthesis methods have different advantage. For example, electrochemical deposition has advantage of room temperature and low energy condition, whereas CVD method has advantage of large scale synthesis. Pyrolysis method can selectively synthesize the heteroatom doping. Second, electrochemical analysis for synthesized carbon nanomaterial. According to related research shown in chapter 1.4.1 and 1.4.2, heteroatom doped carbon nanomaterial has electrochemical activity such as ORR and OER. Therefore, I synthesized various heteroatom doped carbon nanomaterials and characterized the ORR and OER activity. Finally, I discussed the synthesis mechanism and electrochemical reaction mechanism.

Chapter 2 describes selective synthesis of carbon nanomaterials such as graphitic carbon or *trans*-poly acetylene by electrochemical deposition using hydrophobic ionic liquid. *Chapter 3* describes vertically aligned CNT (VA-CNT) by water-assisted CVD using carbon sources such as ethylene and hexane, and nitrogen-doped VA-CNT by pyrolysis process, as well as characterization of ORR activity. Chapter 4 describes synthesis and characterization of the fluorine doped carbon black using Nafion with Ketjen black for OER catalyst. Furthermore, I discussed relationship between catalytic activity and carbon to fluorine bond.

The result of this study will offer high potential for synthesis of various carbon nanomaterials and application for electrochemical catalyst using heteroatom doped carbon nanomaterials. Finally, this result will provide electrocatalytic application through the control of bond structure.

1.6 Reference

- (1) Lide, D. R. *CRC Handbook of Chemistry and Physics*, 85th ed.; CRC Press, 2004.

- (2) Edwards, J. H.; Feast, W. J. A New Synthesis of Poly(Acetylene). *Polymer (Guildf)*. **1980**, *21* (6), 595–596.
- (3) Emery, N.; Hérold, C.; Marêché, J.-F.; Lagrange, P. Synthesis and Superconducting Properties of CaC(6). *Sci. Technol. Adv. Mater.* **2008**, *9* (4), 44102.
- (4) Tchougreeff, A. L.; Hoffmann, R. Charge and Spin Density Waves in the Electronic Structure of Graphite: Application to Analysis of STM Images. *J. Phys. Chem.* **1992**, *96* (22), 8993–8998.
- (5) Karabulut, S.; Cetinkaya, S.; Imamoglu, Y. No Title. *Appl. Organomet. Chem.* **2005**, *19*, 997.
- (6) Guo, T.; Nikolaev, P.; Rinzler, A. G.; Tomanek, D.; Colbert, D. T.; Smalley, R. E. Self-Assembly of Tubular Fullerenes. *J. Phys. Chem.* **1995**, *99* (27), 10694–10697.
- (7) R. McFeely, F.; P. Kowalczyk, S.; Ley, L.; G. Carvell, R.; A. Pollak, R.; A. Shirley, D. X-Ray Photoemission Studies of Diamond, Graphite, and Glassy Carbon Valence Bands. *Phys. Rev. B* **1974**, *9*, 5268–5278.
- (8) Hirsch, A. The Era of Carbon Allotropes. *Nat. Mater.* **2010**, *9* (11), 868–871.
- (9) Hanssen, L. M.; Carrington, W. A.; Butler, J. E.; Snail, K. A. Diamond Synthesis Using an Oxygen-Acetylene Torch. *Mater. Lett.* **2007**, *61* (14–15), 2847–2850.
- (10) Kaniyoor, A.; Baby, T. T.; Ramaprabhu, S. Graphene Synthesis via Hydrogen Induced Low Temperature Exfoliation of Graphite Oxide. *J. Mater. Chem.* **2010**, *20* (39), 8467.
- (11) Ren, Z. F.; Huang, Z. P.; Xu, J. W.; Wang, J. H.; Bush, P.; Siegal, M. P.; Provencio, P. N. Synthesis of Large Arrays of Well-Aligned Carbon Nanotubes on Glass. *Science* (80-.). **1998**, *282* (5391), 1105 LP-1107.

- (12) Hunter, J. M.; Fye, J. L.; Roskamp, E. J.; Jarrold, M. F. Annealing Carbon Cluster Ions: A Mechanism for Fullerene Synthesis. *J. Phys. Chem.* **1994**, *98* (7), 1810–1818.
- (13) Duz, B.; Pekmez, K.; Imamoglu, Y.; Suzer, S.; Yildiz, A. No Title. *J. Organomet. Chem.* **2003**, *684*, 77.
- (14) Tavakol, H.; Keshavarzipour, F. A Sulfur Doped Carbon Nanotube as a Potential Catalyst for the Oxygen Reduction Reaction. *RSC Adv.* **2016**, *6* (67), 63084–63090.
- (15) Tian, G.-L.; Zhao, M.-Q.; Yu, D.; Kong, X.-Y.; Huang, J.-Q.; Zhang, Q.; Wei, F. Nitrogen-Doped Graphene/Carbon Nanotube Hybrids: In Situ Formation on Bifunctional Catalysts and Their Superior Electrocatalytic Activity for Oxygen Evolution/Reduction Reaction. *Small* **2014**, *10* (11), 2251–2259.
- (16) Martin, H. B. Hydrogen and Oxygen Evolution on Boron-Doped Diamond Electrodes. *J. Electrochem. Soc.* **1996**, *143* (6), L133.
- (17) Yang, D.-S.; Bhattacharjya, D.; Inamdar, S.; Park, J.; Yu, J.-S. Phosphorus-Doped Ordered Mesoporous Carbons with Different Lengths as Efficient Metal-Free Electrocatalysts for Oxygen Reduction Reaction in Alkaline Media. *J. Am. Chem. Soc.* **2012**, *134* (39), 16127–16130.
- (18) Yan, D.; Dou, S.; Tao, L.; Liu, Z.; Liu, Z.; Huo, J.; Wang, S. Electropolymerized Supermolecule Derived N, P Co-Doped Carbon Nanofiber Networks as a Highly Efficient Metal-Free Electrocatalyst for the Hydrogen Evolution Reaction. *J. Mater. Chem. A* **2016**, *4* (36), 13726–13730.
- (19) Gong, K.; Du, F.; Xia, Z.; Durstock, M.; Dai, L. Nitrogen-Doped Carbon Nanotube Arrays with High Electrocatalytic Activity for Oxygen Reduction. *Science* (80-.).

- 2009**, 323 (5915), 760–764.
- (20) Griffiths, D. J. *Introduction to Quantum Mechanics*, 2nd ed.; Cambridge University Press, 2016.
- (21) Levine, I. N. *Quantum Chemistry*, 6th ed.; Pearson, 2009.
- (22) Bohr, N. LXXIII. On the Constitution of Atoms and Molecules. *Philos. Mag. Ser. 6* **1913**, 26 (155), 857–875.
- (23) Fierz, M.; Pauli, W. On Relativistic Wave Equations for Particles of Arbitrary Spin in an Electromagnetic Field. *Proc. R. Soc. London. Ser. A. Math. Phys. Sci.* **1939**, 173 (953), 211 LP-232.
- (24) Bohr, N. Faraday Lecture. Chemistry and the Quantum Theory of Atomic Constitution. *J. Chem. Soc.* **1932**, No. 0, 349–384.
- (25) Krätschmer, W.; Lamb, L. D.; Fostiropoulos, K.; Huffman, D. R. Solid C60: A New Form of Carbon. *Nature* **1990**, 347 (6291), 354–358.
- (26) Williams, O. A. Nanocrystalline Diamond. *Diam. Relat. Mater.* **2011**, 20 (5–6), 621–640.
- (27) Ponomarenko, L. A.; Schedin, F.; Katsnelson, M. I.; Yang, R.; Hill, E. W.; Novoselov, K. S.; Geim, A. K. Chaotic Dirac Billiard in Graphene Quantum Dots. *Science* (80-.). **2008**, 320 (5874), 356–358.
- (28) Kroto, H. W.; Heath, J. R.; O'Brien, S. C.; Curl, R. F.; Smalley, R. E. C60: Buckminsterfullerene. *Nature* **1985**, 318 (6042), 162–163.
- (29) Lieber, C. M.; Chen, C.-C. Preparation of Fullerenes and Fullerene-Based Materials;

- 1994; pp 109–148.
- (30) Mitsumoto, R.; Araki, T.; Ito, E.; Ouchi, Y.; Seki, K.; Kikuchi, K.; Achiba, Y.; Kurosaki, H.; Sonoda, T.; Kobayashi, H.; et al. Electronic Structures and Chemical Bonding of Fluorinated Fullerenes Studied by NEXAFS, UPS, and Vacuum-UV Absorption Spectroscopies. *J. Phys. Chem. A* **1998**, *102* (3), 552–560.
- (31) Wang, Y.; Hu, A. Carbon Quantum Dots: Synthesis, Properties and Applications. *J. Mater. Chem. C* **2014**, *2* (34), 6921.
- (32) Dresselhaus, M. S.; Dresselhaus, G.; Saito, R. Physics of Carbon Nanotubes. *Carbon N. Y.* **1995**, *33* (7), 883–891.
- (33) Rao, C. N. R.; Voggu, R.; Govindaraj, A. Selective Generation of Single-Walled Carbon Nanotubes with Metallic, Semiconducting and Other Unique Electronic Properties. *Nanoscale* **2009**, *1* (1), 96.
- (34) Wilder, J. W. G.; Venema, L. C.; Rinzler, A. G.; Smalley, R. E.; Dekker, C. Electronic Structure of Atomically Resolved Carbon Nanotubes. *Nature* **1998**, *391* (6662), 59–62.
- (35) Mintmire, J. W.; White, C. T. Universal Density of States for Carbon Nanotubes. *Phys. Rev. Lett.* **1998**, *81* (12), 2506–2509.
- (36) Odom, T. W.; Huang, J.-L.; Kim, P.; Lieber, C. M. Atomic Structure and Electronic Properties of Single-Walled Carbon Nanotubes. *Nature* **1998**, *391* (6662), 62–64.
- (37) Couderc, P.; Catherine, Y. Structure and Physical Properties of Plasma-Grown Amorphous Hydrogenated Carbon Films. *Thin Solid Films* **1987**, *146* (1), 93–107.
- (38) Natta, G.; Mazzanti, G.; Corradini, P. Polimerizzazione Stereospecifica Dell'acetilene. *Atti. Acad. Naz. Lincei Cl. Sci. Fis. Mat. Nat. Rend.* **1958**, *25*, 3–12.

- (39) Arshak, K.; Velusamy, V.; Korostynska, O.; Oliwa-Stasiak, K.; Adley, C. Conducting Polymers and Their Applications to Biosensors: Emphasizing on Foodborne Pathogen Detection. *IEEE Sens. J.* **2009**, *9* (12), 1942–1951.
- (40) Neto, A. H. C.; Guinea, F.; Peres, N. M. R.; Novoselov, K. S.; Geim, A. K. The Electronic Properties of Graphene. **2007**, *81* (March).
- (41) Gillespie, R. J. Teaching Molecular Geometry with the VSEPR Model. *J. Chem. Educ.* **2004**, *81* (3), 298.
- (42) Pauling, L. THE NATURE OF THE CHEMICAL BOND. APPLICATION OF RESULTS OBTAINED FROM THE QUANTUM MECHANICS AND FROM A THEORY OF PARAMAGNETIC SUSCEPTIBILITY TO THE STRUCTURE OF MOLECULES. *J. Am. Chem. Soc.* **1931**, *53* (4), 1367–1400.
- (43) Li, Z.-Y.; Shaheer Akhtar, M.; Hee Kuk, J.; Kong, B.-S.; Yang, O.-B. Graphene Application as a Counter Electrode Material for Dye-Sensitized Solar Cell. *Mater. Lett.* **2012**, *86*, 96–99.
- (44) Geim, A. K. Graphene: Status and Prospects. *Science* (80-.). **2009**, *324* (5934), 1530 LP-1534.
- (45) Mannoor, M. S.; Jiang, Z.; James, T.; Kong, Y. L.; Malatesta, K. A.; Soboyejo, W. O.; Verma, N.; Gracias, D. H.; McAlpine, M. C. 3D Printed Bionic Ears. *Nano Lett.* **2013**, *13* (6), 2634–2639.
- (46) Lavoisier, A. *Elements of Chemistry, in a New Systematic Order: Containing All the Modern Discoveries*; Courier Corporation, 1965.
- (47) Tennant, S. On the Nature of the Diamond. By Smithson Tennant, Esq. F. R. S. *Philos.*

Trans. R. Soc. London **1797**, 87, 123–127.

- (48) Collins, A. T. Thin Film Diamond - The Optical and Electronic Properties of Semiconducting Diamond. *Philos. Trans. R. Soc. London. Ser. A Phys. Eng. Sci.* **1993**, 342 (1664), 233 LP-244.
- (49) Novoselov, K. S.; Geim, A. K.; Morozov, S. V; Jiang, D.; Katsnelson, M. I.; Grigorieva, I. V; Dubonos, S. V; Firsov, A. A. Two-Dimensional Gas of Massless Dirac Fermions in Graphene. *Nature* **2005**, 438 (7065), 197–200.
- (50) Novoselov, K. S.; Geim, A. K.; Morozov, S. V; Jiang, D.; Zhang, Y.; Dubonos, S. V; Grigorieva, I. V; Firsov, A. A. Electric Field Effect in Atomically Thin Carbon Films. *Science* (80-.). **2004**, 306 (5696), 666 LP-669.
- (51) Iijima, S. Helical Microtubules of Graphitic Carbon. *Nature* **1991**, 354 (6348), 56–58.
- (52) Reina, A.; Jia, X.; Ho, J.; Nezich, D.; Son, H.; Bulovic, V.; Dresselhaus, M. S.; Kong, J. Large Area, Few-Layer Graphene Films on Arbitrary Substrates by Chemical Vapor Deposition. *Nano Lett.* **2009**, 9 (1), 30–35.
- (53) Kundrapu, M.; Li, J.; Shashurin, A.; Keidar, M. A Model of Carbon Nanotube Synthesis in Arc Discharge Plasmas. *J. Phys. D. Appl. Phys.* **2012**, 45 (31).
- (54) Janas, D.; Koziol, K. K. Carbon Nanotube Fibers and Films: Synthesis, Applications and Perspectives of the Direct-Spinning Method. *Nanoscale* **2016**, 8 (47), 19475–19490.
- (55) Zhao, P.; Kumamoto, A.; Kim, S.; Chen, X.; Hou, B.; Chiashi, S.; Einarsson, E.; Ikuhara, Y.; Maruyama, S. Self-Limiting Chemical Vapor Deposition Growth of Monolayer Graphene from Ethanol. *J. Phys. Chem. C* **2013**, 117 (20), 10755–10763.

- (56) Kong, J.; Cassell, A. M.; Dai, H. Chemical Vapor Deposition of Methane for Single-Walled Carbon Nanotubes. *Chem. Phys. Lett.* **1998**, *292* (4–6), 567–574.
- (57) Hofmann, S.; Csányi, G.; Ferrari, A. C.; Payne, M. C.; Robertson, J. Surface Diffusion: The Low Activation Energy Path for Nanotube Growth. *Phys. Rev. Lett.* **2005**, *95* (3), 36101.
- (58) Hata, K.; Futaba, D. N.; Mizuno, K.; Namai, T.; Yumura, M.; Iijima, S. Water-Assisted Highly Efficient Synthesis of Impurity-Free Single-Walled Carbon Nanotubes. *Science* (80-.). **2004**, *306* (5700), 1362 LP-1364.
- (59) Yoshida, H.; Takeda, S.; Uchiyama, T.; Kohno, H.; Homma, Y. Atomic-Scale In-Situ Observation of Carbon Nanotube Growth from Solid State Iron Carbide Nanoparticles. *Nano Lett.* **2008**, *8* (7), 2082–2086.
- (60) Gal-Or, L.; Silberman, I.; Chaim, R. Electrolytic ZrO₂ Coatings: I. Electrochemical Aspects. *J. Electrochem. Soc.* **1991**, *138* (7), 1939–1942.
- (61) Shawky, A.; Yasuda, S.; Murakoshi, K. Room-Temperature Synthesis of Single-Wall Carbon Nanotubes by an Electrochemical Process. *Carbon N. Y.* **2012**, *50* (11), 4184–4191.
- (62) Namba, Y. Attempt to Grow Diamond Phase Carbon Films from an Organic Solution. *J. Vac. Sci. Technol. A Vacuum, Surfaces, Film.* **1992**, *10* (5), 3368–3370.
- (63) Gupta, S.; Roy, R. K.; Deb, B.; Kundu, S.; Pal, A. K. Low Voltage Electrodeposition of Diamond-like Carbon Films. *Mater. Lett.* **2003**, *57* (22–23), 3479–3485.
- (64) Kundoo, S.; Saha, P.; Chattopadhyay, K. K. Electron Field Emission from Nitrogen and Sulfur-Doped Diamond-like Carbon Films Deposited by Simple Electrochemical

- Route. *Mater. Lett.* **2004**, 58 (30), 3920–3924.
- (65) Ling, X.; Zhang, P.; Li, R.; Fan, D.; Yao, X. Electron Field Emission of Iron and Cobalt-Doped DLC Films Fabricated by Electrochemical Deposition. *Surf. Interface Anal.* **2013**, 45 (5), 943–948.
- (66) Keresztury, G. Raman Spectroscopy: Theory. In *Handbook of Vibrational Spectroscopy*; John Wiley & Sons, Ltd, 2006; pp 43–44.
- (67) Tolles, W.; Nibler, J.; McDonald, J. R.; Harvey, A. B. *A Review of the Theory and Application of Coherent Anti-Stokes Raman Spectroscopy (CARS)*; 1977; Vol. 31.
- (68) Jorio, A.; Pimenta, M. A.; Filho, A. G. S.; Saito, R.; Dresselhaus, G.; Dresselhaus, M. S. Characterizing Carbon Nanotube Samples with Resonance Raman Scattering. *New J. Phys.* **2003**, 5, 139.1-139.17.
- (69) Wang, H.; Wang, Y.; Cao, X.; Feng, M.; Lan, G. Vibrational Properties of Graphene and Graphene Layers. *J. Raman Spectrosc.* **2009**, 40 (12), 1791–1796.
- (70) Dresselhaus, M. S.; Dresselhaus, G.; Saito, R.; Jorio, A. Raman Spectroscopy of Carbon Nanotubes. *Phys. Rep.* **2005**, 409 (2), 47–99.
- (71) Lang, K. M.; Hite, D. A.; Simmonds, R. W.; McDermott, R.; Pappas, D. P.; Martinis, J. M. Conducting Atomic Force Microscopy for Nanoscale Tunnel Barrier Characterization. *Rev. Sci. Instrum.* **2004**, 75 (8), 2726–2731.
- (72) Zhong, Q.; Inniss, D.; Kjoller, K.; Elings, V. B. Fractured Polymer/Silica Fiber Surface Studied by Tapping Mode Atomic Force Microscopy. *Surf. Sci.* **1993**, 290 (1–2), L688–L692.
- (73) Schull, C. G. The Determination of Pore Size Distribution from Gas Adsorption Data.

- J. Am. Chem. Soc.* **1948**, *70* (4), 1405–1410.
- (74) Brunauer, S.; Emmett, P. H.; Teller, E. Adsorption of Gases in Multimolecular Layers. *J. Am. Chem. Soc.* **1938**, *60* (2), 309–319.
- (75) Siegbahn, K.; Edvarson, K. β -Ray Spectroscopy in the Precision Range of 1 : 105. *Nucl. Phys.* **1956**, *1* (8), 137–159.
- (76) Wang, Y.; Chen, K. S.; Mishler, J.; Cho, S. C.; Adroher, X. C. A Review of Polymer Electrolyte Membrane Fuel Cells: Technology, Applications, and Needs on Fundamental Research. *Appl. Energy* **2011**, *88* (4), 981–1007.
- (77) Bard, A. J.; Faulkner, L. R. *Electrochemical Methods: Fundamentals and Applications*, Vol 2.; Wiley: New York, 1980.
- (78) Yeager, E. Dioxygen Electrocatalysis: Mechanisms in Relation to Catalyst Structure. *J. Mol. Catal.* **1986**, *38* (1–2), 5–25.
- (79) Zhang, M.; Yan, Y.; Gong, K.; Mao, L.; Guo, Z.; Chen, Y. Electrostatic Layer-by-Layer Assembled Carbon Nanotube Multilayer Film and Its Electrocatalytic Activity for O₂ Reduction. *Langmuir* **2004**, *20* (20), 8781–8785.
- (80) Antoine, O.; Durand, R. RRDE Study of Oxygen Reduction on Pt Nanoparticles inside Nafion® : H₂O₂ Production in PEMFC Cathode Conditions. *J. Appl. Electrochem.* **2000**, *30* (7), 839–844.
- (81) ZHDANOV, V.; KASEMO, B. Kinetics of Electrochemical O₂ Reduction on Pt. *Electrochem. commun.* **2006**, *8* (7), 1132–1136.
- (82) Yu, L.; Pan, X.; Cao, X.; Hu, P.; Bao, X. Oxygen Reduction Reaction Mechanism on Nitrogen-Doped Graphene: A Density Functional Theory Study. *J. Catal.* **2011**, *282*

- (1), 183–190.
- (83) Yasuda, S.; Yu, L.; Kim, J.; Murakoshi, K. Selective Nitrogen Doping in Graphene for Oxygen Reduction Reactions. *Chem. Commun.* **2013**, 49 (83), 9627.
- (84) Li, X.; Hao, X.; Abudula, A.; Guan, G. Nanostructured Catalysts for Electrochemical Water Splitting: Current State and Prospects. *J. Mater. Chem. A* **2016**, 4 (31), 11973–12000.
- (85) Suen, N.-T.; Hung, S.-F.; Quan, Q.; Zhang, N.; Xu, Y.-J.; Chen, H. M. Electrocatalysis for the Oxygen Evolution Reaction: Recent Development and Future Perspectives. *Chem. Soc. Rev.* **2017**, 46 (2), 337–365.
- (86) Rossmeisl, J.; Qu, Z. W.; Zhu, H.; Kroes, G. J.; Nørskov, J. K. Electrolysis of Water on Oxide Surfaces. *J. Electroanal. Chem.* **2007**, 607 (1–2), 83–89.
- (87) Wang, J.; Zhong, H.; Qin, Y.; Zhang, X. An Efficient Three-Dimensional Oxygen Evolution Electrode. *Angew. Chemie Int. Ed.* **2013**, 52 (20), 5248–5253.

Chapter 2

Selective syntheses of graphitic carbon and polyacetylene by electrochemical deposition

2.1 Introduction

Conjugated carbon nanomaterials have been widely studied in various fields owing to their unique physical, electrical, thermal, electrochemical, and mechanical properties. Many researchers have adopted various techniques in *Section 1.2*. Among them, electrochemical deposition has come into spotlight due to its low-cost, easy-process and room temperature synthesis. Recently, single wall carbon nanotubes (SWCNTs) was synthesized by electrochemical deposition from acetic acid on Ni nanocatalysts supported by Au.¹ This room-temperature electrochemical process is a promising technique for future applications because it is a simple process compared with the conventional methods. However, the process results in a relatively low yield of SWCNTs (ca. a few tubes / μm^2) due to the low efficiency of the acetic acid reduction reaction, despite the very unique characteristics that enable control of selective C-C bond formation by the size of the metal nanoparticle catalysts on the Au electrode.

Halogenated carbon molecules have high electrochemical decomposition characteristics and have been used as carbon sources for the synthesis of various carbon materials.^{2,3} For example, Herrick and *et al.* reported that carbonaceous fibers can be synthesized in high yield by the galvanostatic deposition of CCl_4 in acetonitrile onto a metal

substrate at room temperature.⁴ The reduction of other halogenated carbon molecules, such as poly(tetrafluoroethylene), hexachlorobuta-1,3-diene and diiodoacetylene, has also resulted in the production of graphitic carbon films.^{5,6} Further analyses indicated that the carbonization process was highly sensitive to the presence of protons in the solvent. In the aprotic solvent, C–C bond formation is dominated by carbon radical reactions, while in protic solvent, carbon–hydrogen (C–H) bond formation is preferential by protonation of the carbon radicals.^{7,8} On the basis of the previous results, protic solvent is critical factor for carbon nanomaterial synthesis and growth. Yan *et al.* reported that hydrogenated diamond-like carbon film which consists of alkane chain can be polymerized by electrochemical deposition from methanol decomposition on the Si substrate.^{9,10} However, this method suffers from high voltage condition with 800 V of methanol decomposition. Previous work demonstrates that the growth of amorphous carbon (a-C:H) films can be obviously promoted by introducing a large quantity of deionized water.¹¹ Meanwhile, acetic acid¹² or formic acid¹³ has been used as carbon source for preparation of carbon film under a low voltage below 20 V, indicating that high voltage is not an essential condition for a-C:H film deposition. However, this condition was suffered from relatively higher temperature about 80 °C.

From consideration of these results, electrochemical reduction of halogenated carbon molecules was employed in this present chapter to achieve high yield relative to previous Shawky's study,¹ and control of the C–C bond formation during synthesis. Hydrophobic ionic liquid was used as an electrolyte because it possesses a wide electrochemical window but can be also used for the controlling the amount of H₂O as proton source, that was difficult for organic solvent. In this study, I adopted the halogenated carbon source such as CCl₄ and CBr₄ as carbon precursor, and the effect of H₂O addition as a proton source was investigated for selective carbon growth by electrochemical deposition method.

2.2 Experimental methods

A three-electrode cell was used for the electrochemical deposition system. Carbon tetrachloride (99.5%, Wako Chemical) and carbon tetrabromide (99.0 %, TCI) were used as the carbon source. *N,N,N*-trimethyl-*N*-propylammonium bis(trifluoromethane)sulfonimide (TMPA-TFSI, Kanto Chemical) was used as the electrolyte, and their molecular structures are shown in Fig 2.1. This ionic liquid has negligible vapor pressure and high temperature stability; therefore, the dehydrated ionic liquid can be easily prepared by heat treatment at 120 °C for 24 h in a vacuum oven (ca. 10 kPa). The reference electrode was a Ag/Ag⁺ electrode in 0.05 M Ag(SO₃CF₃) (99.5% Wako Chemicals) in TMPA-TFSI. 0.1 mm-thick Pt and Ni foils were used as the counter and working electrodes, respectively. Ni foil was ultrasonicated in ethanol for 10 min, and the Pt foils and electrochemical cell were cleaned in piranha solution (H₂SO₄: H₂O₂ = 3 : 1) for 1 h and then rinsed with excess deionized H₂O. All electrodes and the cell were stored in a vacuum oven for 1 day at 120 °C to eliminate all trace amounts of H₂O. To prevent exposure to H₂O, setup of the cell and electrochemical deposition were conducted inside a glove bag under nitrogen gas flow at room temperature. A potentiostat (Hokuto Denko, HSV-110) was used for the electrochemical system. Ar or N₂ gases were bubbled from the inlet to remove oxygen from the electrolyte, and carbon was electrochemically deposited at -2.5 V for polarization time of from 1 to 30 min. Prior to characterization, the as-deposited samples were rinsed with acetone and deionized H₂O (MILLIPORE Milli-Q, resistance: 18.2 MΩ cm) to eliminate the ionic liquid. The influence of a proton source on carbonization was investigated by the addition of 0.1 M deionized H₂O in TMPA-TFSI. Raman spectroscopy (Thermo Scientific, DXR, laser wavelength: 532 nm) and atomic force microscopy (AFM; Nanoscope IIIa, Veeco) in tapping mode were used to analyze the deposited carbon material.

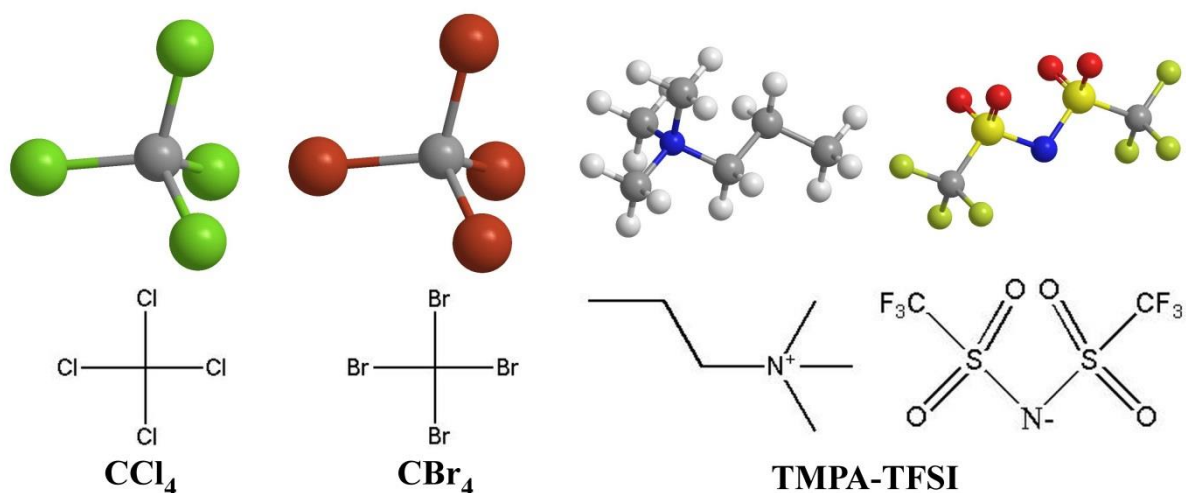


Fig 2.1 Molecular structure of carbon tetrachloride (CCl_4), carbon tetrabromide (CBr_4), and N,N,N-trimethyl-N-propylammonium bis(trifluoromethane)sulfonimide (TMPA-TFSI) ionic liquid as electrolyte.

2.3 Results and discussion

2.3.1 Graphitic carbon synthesis by electrochemical deposition

Cyclic voltammogram (CV) was performed for TMPA-TFSI (ionic liquid, IL), 0.1 M CCl_4 in IL, and 0.1 M CBr_4 in IL to verify electrochemical characteristics as shown in Fig 2.2 (a). In case of the IL (black lines), reduction currents were observed at onset potential of -2.7 V and leading to -0.15 mA cm^{-2} at -3.0 V. In contrast, the reduction currents for solutions of IL containing CCl_4 (red line) and CBr_4 (blue line) were reduced at onset potential of -2.2 V, and -1.6 V, respectively. The higher reduction onset potential observed in CCl_4 than CBr_4 indicates that C-Cl bond is stronger than C-Br bond.¹⁴ In addition, peak of reduction current for CCl_4 in IL, and CBr_4 in IL were reached -0.25 mA cm^{-2} and -0.30 mA cm^{-2} at -3.0 V, respectively. Reduction of halogenated carbon such as CCl_4 and CBr_4 is possible by electrochemical method. Electrochemical deposition was conducted using

chronoamperometry for evaluation of the deposited material and state. Under constant potential of -2.5 V for 30 min on the Ni substrate as represented in Fig 2.2 (b) black lines, the cathodic current density of ionic liquid immediately decreased after the potential step and then quickly dropped to $-3 \mu\text{A cm}^{-2}$. In contrast, the current densities for both ionic liquid with CCl_4 (red line) and CBr_4 (blue line) are continued to flow until the end of the deposition, which suggests that the reduction reaction proceeds on the surface during negative polarization.

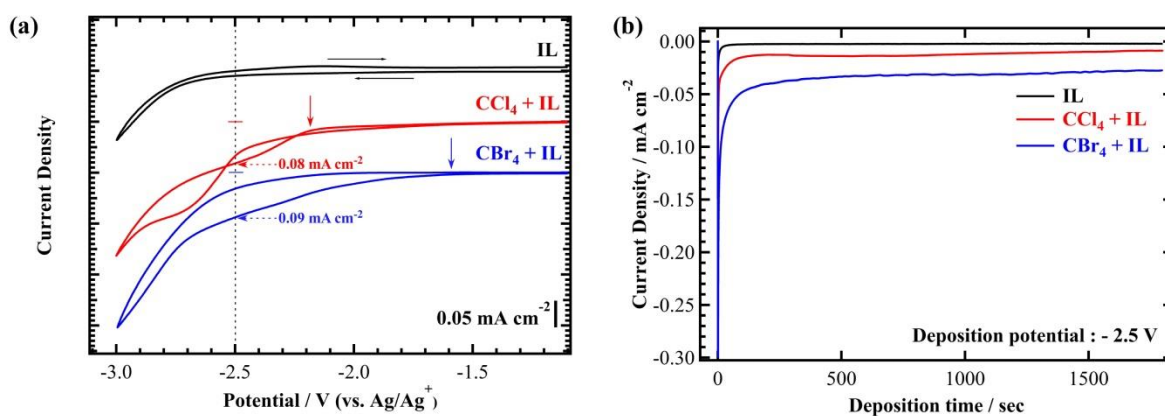


Fig 2.2 (a) Cyclic voltammogram and (b) chronoamperometry of IL (black), CCl_4 + IL (red line), and CBr_4 + IL (blue line). Onset potentials were indicated with arrow. All CV results were obtained at a scan rate of 50 mV/s.

Next, Raman spectroscopy was used to verify the deposited material in Fig 2.3 (b). As a result, Raman spectrum of ionic liquid was not observed in every Raman shift range. On the other hand, in case of as-deposited CCl_4 and CBr_4 in IL, Raman measurement showed two broad Raman peaks at ca. 1570 and 1355 cm^{-1} (Fig. 2.3(b) red and blue lines). It is well known that single crystal graphite, which consists of a pure sp^2 carbon structure, has a single peak at 1580 cm^{-1} arising from the tangential mode (G band), and sp^2 disordered graphite has a broad peak at around 1350 cm^{-1} (D band). The G band has E_{2g} symmetry, which is due to the in-plane vibration of sp^2 carbon atoms and the stacking order, whereas the D band has T_{2g} symmetry, which is attributed to interaxial vibration on the carbon atoms.¹⁵ The ratio of the D to G band intensity (I_D/I_G) enables an estimation of the degree of structural disorder in the sp^2 graphitic carbon structure.¹⁶ Highly crystalline graphite exhibits a low I_D/I_G (typically <0.1). In contrast, polycrystalline or disordered graphitic carbon materials including disordered carbon structures have relatively large I_D/I_G (typically ~ 1). The deposited carbon material had an I_D/I_G value around 0.6 for CCl_4 , and 0.7 for CBr_4 , which indicate the formation of a graphitic carbon structure.

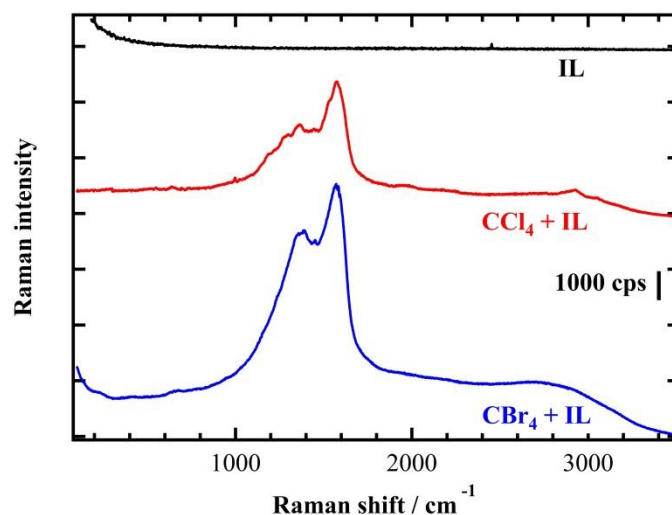
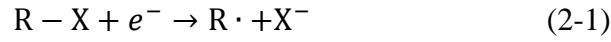


Fig 2.3 Raman spectra for IL (black), CCl_4 + IL (red line), and CBr_4 + IL (blue line). Laser excitation wavelength: 532 nm.

I consider the graphitic carbon growth mechanism. According to previous studies,¹⁷ the dehalogenation process of a carbon-halogen bond on a cathode occurs as follows:



Electron transfer from the cathode to the halogenated carbon molecule R-X (X = halogen atom) initially dissociates the carbon-halogen bond through intermediate molecular anion formation, and then generates carbon radicals R· (Eq. (2-1)). These carbon radicals induce radical reaction and facilitate electrochemical carbonization products (Eq. (2-2)).

Considering these reactions, the electrochemical reduction reaction with CX₄ contributes to the production of carbon radicals (Eq. (2-1)). These carbon radicals such as trihalogenated carbon radical (·CX₃) and dihalogenated carbon biradical (:CX₂) react with each other (Eq. (2-2)) followed by a propagation step of the radicals with the products. Finally, further dehalogenation of these products occurs at the surface, which results in graphitic carbon film formation.

To obtain further insight, the dependence of film formation on the deposition time was investigated. Fig. 2.4 (a)-(c) show CCD images for (a) blank, (b) CCl_4 in IL, and (c) CBr_4 in IL after electrochemical deposition of 30 min on Ni substrate. The color of the film became uniformly darker after 30 min duration of electrochemical deposition. In addition, brown color for CBr_4 in IL is darker than that of CCl_4 in IL. Furthermore, AFM image also appeared as formation of wide and uniform film for decomposed halogenated carbon in Fig. 2.4 (d)-(f). This result also shows that CBr_4 is easily decomposed than CCl_4 by electrochemical deposition, resulting in formation of graphitic carbon.

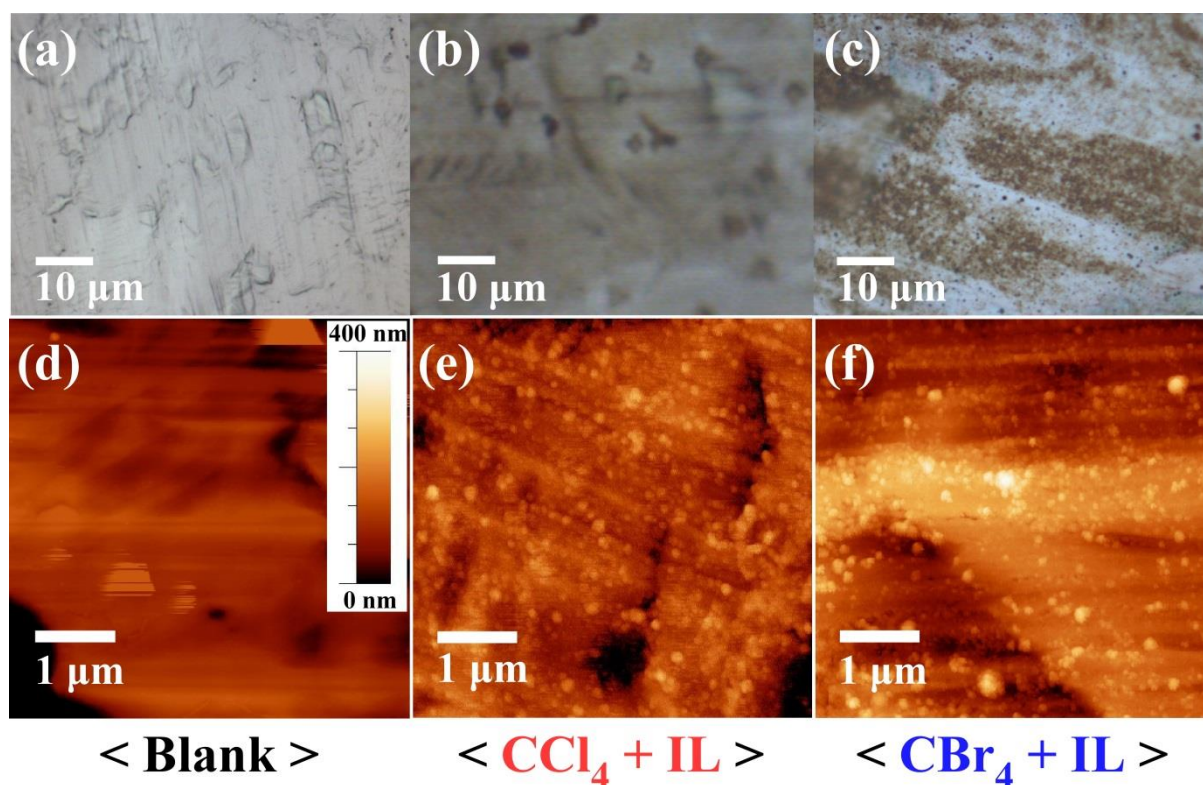


Fig 2.4 CCD images for (a) blank, (b) CCl_4 + IL, and (c) CBr_4 + IL after deposition time of 30 min on Ni substrate. AFM images for (d) blank, (e) CCl_4 + IL, and (f) CBr_4 + IL after deposition time of 30 min on Ni substrate.

The I_D/I_G values from the Raman bands intensities (D-bands and G-bands) shown in Fig. 2.5 gradually increased with the deposition time. These trends indicate that after nucleation of the graphitic nanoparticles formed by the reaction in Eq. (2-1), the particles homogeneously grow in size and thickness upon the reduction reaction progresses to the edge and defect sites of the particles, which results in the formation of a uniform graphitic carbon film.

The graphitic carbon particle size can be calculated according to the following equation:¹⁸

$$L_a(\text{nm}) = (2.4 \times 10^{-10}) \lambda_l^4 \left(\frac{I_D}{I_G}\right)^{-1} \quad (2-3)$$

where L_a and λ_l are the theoretical crystallite size and the Raman laser wavelength, respectively. From this equation, the graphitic particle size for CCl_4 in IL was estimated to be approximately 27 nm, which is good agreement with the size of 34 nm for CCl_4 in IL determined by AFM analysis.

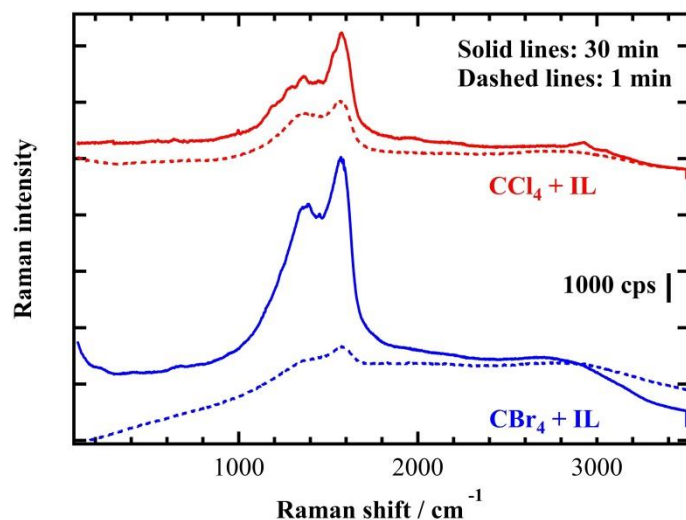


Fig 2.5 Comparison of Raman spectra for $\text{CCl}_4 + \text{IL}$ (red lines) and $\text{CBr}_4 + \text{IL}$ (blue lines) after deposition time of 30 min (solid lines) and 1 min (dashed lines) on Ni substrate.

On the basis of the result, I discussed the growth mechanism. In general, the deposited graphitic carbon has conductivity.¹⁹ Therefore, it is suggested that halogenated carbon such as CCl₄ or CBr₄ could be electrochemically reduced over deposited graphitic carbon by reacting with dangling bond of the graphitic carbon edges, resulting in the thicker graphitic carbon formation growth. Especially, deposited carbon densities could be estimated. In the Shawky's previous work, synthesized carbon nanotubes were covered about a few tubes per 1 μm², which corresponds with the density of 10⁻¹⁸ g/cm². On the other hand, densities of synthesized graphitic carbon in this study was obtained about 10⁻⁶ g/cm², by calculating total electric charges of CCl₄ in Fig. 2.2 (b). These comparisons show that the yield in our system is enormously higher than that in the Shawky's work.¹ Furthermore, the current efficiencies for both carbon depositions were also roughly estimated to be second order of magnitude higher, indicating that my deposition system possesses highly conversion efficiency to the carbon materials.

2.3.2 *trans*-poly acetylene synthesis by electrochemical deposition

In this section, I investigated the effect of proton source on the electrochemical deposition and resulting carbon material. In particular, I used an electrolyte IL in the presence of H₂O, and two carbon sources such as CCl₄ in IL with H₂O and CBr₄ in IL with H₂O for protic solvent effect. To check the reduction reaction, cyclic voltammogram was performed for various electrolyte solutions as shown in Fig. 2.6 (a). As a result, reduction current of -0.01 mA cm⁻² for ionic liquid in H₂O (black lines) was observed. On the other hand, CCl₄ in IL with H₂O (red lines), and CBr₄ in IL with H₂O (blue lines) could be reduced by electrochemical process. Especially, reduction current density shows higher values than one of condition without H₂O as represented in Fig 2.2 (a). These results strongly indicate that increments of the current densities are attributed to the reductions of halogenated carbon and H₂O. Based on these results, carbon deposition was investigated at potential step of -2.5 V for 30 min.

Fig. 2.6 (b) shows current density as a function of deposition time curves, in which potential step was applied for each electrolyte solution. In case of IL + H₂O, the current density rapidly rises and drop, it is to say that ionic liquid only acts as the electrolyte, and do not reduce at - 2.5 V. On the other hand, the current densities for CCl₄ in IL with H₂O, and CBr₄ in IL with H₂O gradually increased during 5 min, and then slowly decreased, and the current continued to flow. The observed reductive current peak strongly indicates that carbon deposition mechanism for IL with halogenated carbon and H₂O is different from that of condition without water. According to related studies, Radisic *et al.* reported that same tendency in current versus time curves observed for Cu electrochemical deposition on an Au surface,²⁰ where the growth process was based on a nucleation and growth mode; carbon clusters can be grown at nucleation sites and the size of the clusters is steadily increased.²¹

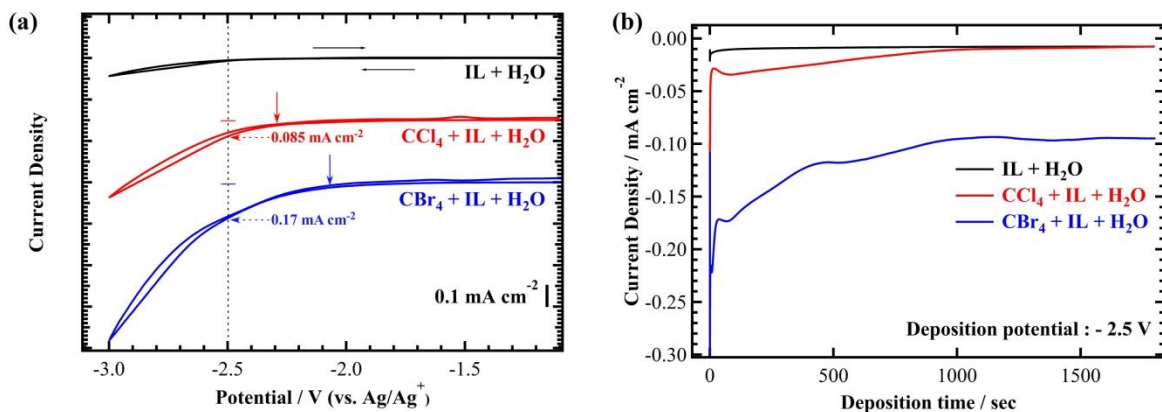


Fig 2.6 (a) Cyclic voltammogram and (b) current versus time curves of IL + H₂O (black line), CCl₄ + IL + H₂O (red line), and CBr₄ + IL + H₂O (blue line). Arrow is onset potential.

To evaluate the deposited material, Fig.2.7 (a) shows Raman spectra for as-deposited IL + H₂O (black line), CCl₄ + IL + H₂O (red line), and CBr₄ + IL + H₂O (blue line) on the Ni substrate. In case of the IL + H₂O (black line), Raman peaks not appear around all Raman shift range. On the other hand, several sharp Raman peaks were observed in samples of CCl₄ + IL + H₂O (red line) and CBr₄ + IL + H₂O (red line), in which correspond to C-C (1115 cm⁻¹), C=C (1500 cm⁻¹ and 2610 cm⁻¹), and C-H (2230 cm⁻¹ and 3000 cm⁻¹) stretching modes of *trans*-poly acetylene as shown in Fig. 2.7 (b).²² Although poly acetylene is well-known to have either *cis*- or *trans*- configuration, Raman bands originating from *cis*-poly acetylene (ca. 920, 1260 and 1550 cm⁻¹) were never observed in this study, indicating the formation of only *trans*-poly acetylene. Furthermore, several small Raman peaks from 300 to 900 cm⁻¹ were also observed, suggesting the formation of a small amount of halogen-modified polyacetylene.²³ Especially, selective carbon synthesis from graphitic carbon to poly acetylene is possible by addition of proton source.

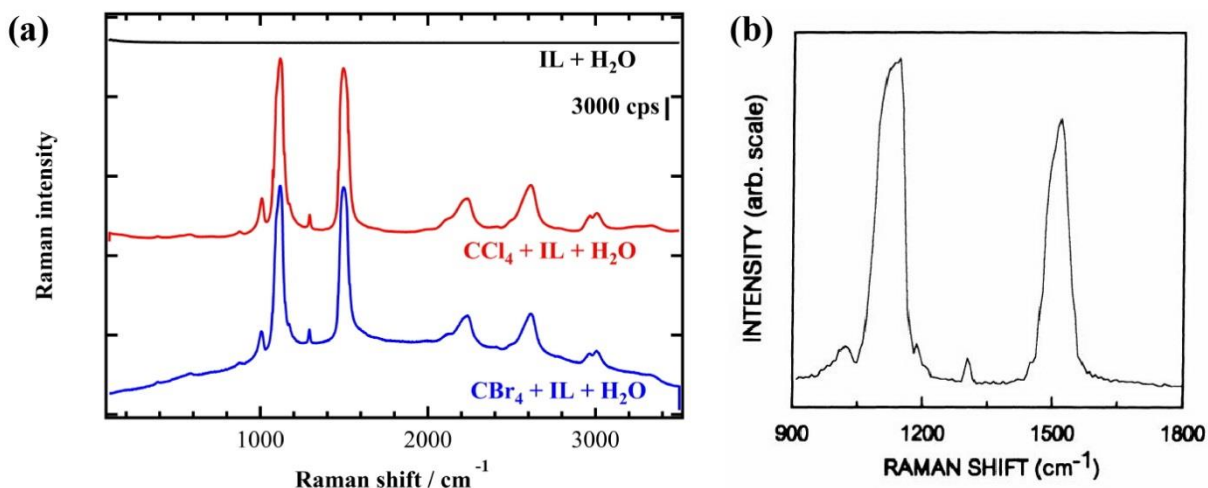


Fig 2.7 (a) Raman spectra for IL + H₂O (black line), CCl₄ + IL + H₂O (red line), and CBr₄ + IL + H₂O (blue line). (b) Raman spectra of trans-poly acetylene as reference data. Laser excitation wavelength: 514 nm.

On the basis of the result, I consider the selective carbon growth mechanism. Using the reaction mechanism of graphitic carbon, the dehalogenation and hydrogenation process of a carbon-halogen bond on a cathode occurs as follows:



For the electrochemical reduction reaction of halogenated carbon in the presence of H₂O, it is suggested that protonation (Eq. (2-4) or Eq. (2-5)) proceeds after the dehalogenation process in Eq. (2-1).

To observe the deposition state, Figs 2.8 (a)-(d) show the CCD images of deposited material for CCl_4 in IL with H_2O at 5 (a), 15 (b), 30 (c), and 45 (d) min. In case of polyacetylene growth in the electrolyte containing halogenated carbon and H_2O , CCD images revealed that small size black particles nucleated over the surface at initial growth stage, and as deposition time increased, the number of nucleation sites and particle size were dramatically increased.

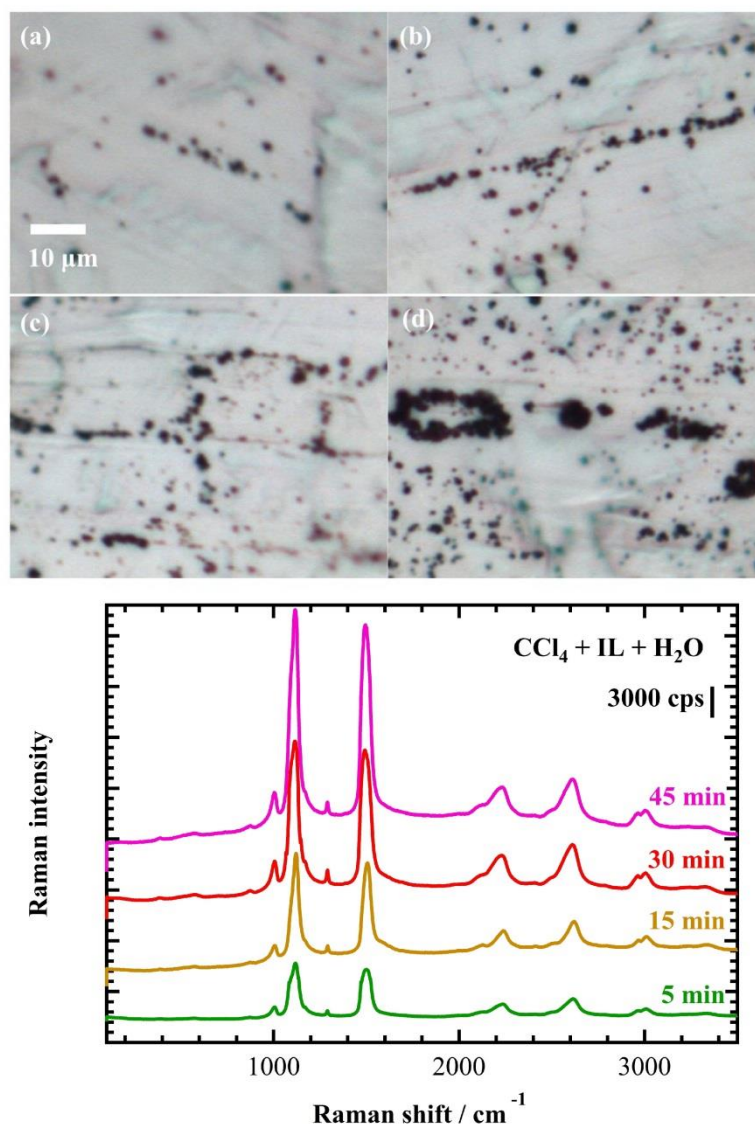


Fig 2.8 CCD images (top) and Raman spectra (bottom) for $\text{CCl}_4 + \text{IL} + \text{H}_2\text{O}$ after deposition time of 5 min (a), 15 min (b), 30 min (c), and 45 min on Ni substrate.

The observed features of these deposits are different from those of the graphitic carbon formation in comparison with Fig 2.4 (b) and (c). Although the intensities in Raman spectra also increased during the formation of the deposits, negligible changes in the features of Raman spectra were observed in the Fig 2.8 (bottom). These results indicate that *trans*-polyacetylene tends to nucleate and grow on the substrate. As shown in Fig. 2.6 (a) and (b), it was suggested that the observed mono-current peak is due to the nucleation and growth mode, which is in good agreement with the results shown in Figs. 2.8 (a) - (d). Therefore, it is considered that at the initial stage, the reduction reactions of Eq. (2-1), (2-4) and (2-5) produce poly acetylene “particles” on the surface. The ionic liquid is considered to be a poor solvent for polyacetylene. Therefore, aggregated particles are expected to form on the surface. These *trans*-polyacetylene particles must have electric conductivity, and thus the reduction reaction occurs on the poly acetylene particles rather than on the bare surface, which results in further nucleation and growth.

2.4 Conclusion

In conclusion, carbon nanomaterials such as graphitic carbon and *trans*-poly acetylene were selectively synthesized by electrochemical deposition. Halogenated carbons such as CCl_4 and CBr_4 were used as carbon source for the synthesis of graphitic carbon. CCl_4 and CBr_4 were easily dehalogenated by electrochemical deposition. Decomposed carbon particles were carbonized by reacting with dangling bond of graphitic carbon edge, resulting in growth of graphitic carbon film. Besides, reproducibility of deposition of graphitic carbon was checked even in different halogenated carbons. This result suggests that synthesis of various carbon nanomaterials is possible using halogenated carbon source.

Furthermore, *trans*-polyacetylene was synthesized by electrochemical deposition using halogenated carbon with protic solvent such as deionized water. For the growth mechanism, *trans*-poly acetylene formation is based on a nucleation and growth mode. In other words, CCl_4 and CBr_4 are affected by dehalogenation and hydrogenation. As a result, hydrogenated carbon is formed. Finally, *trans*-poly acetylene is formed by nucleation and aggregation on the nucleation site of Ni substrate. This synthesis method of *trans*-polyacetylene has not been reported to date, suggesting high potential for new synthesis method of *trans*-polyacetylene derives.

2.5 Reference

- (1) Shawky, A.; Yasuda, S.; Murakoshi, K. Room-Temperature Synthesis of Single-Wall Carbon Nanotubes by an Electrochemical Process. *Carbon N. Y.* **2012**, *50* (11), 4184–4191.
- (2) Saveant, J. M. Electron Transfer, Bond Breaking, and Bond Formation. *Acc. Chem. Res.* **1993**, *26* (9), 455–461.
- (3) Peters, D. G. Halogenated Organic Compounds. In *Organic Electrochemistry*; CRC Press, 2000; pp 341–377.
- (4) Herrick, R. D.; Kaplan, A. S.; Chinh, B. K.; Shane, M. J.; Sailor, M. J.; Kavanagh, K. L.; McCreey, R. L.; Zhao, J. Room-Temperature Electrosynthesis of Carbonaceous Fibers. *Adv. Mater.* **1995**, *7* (4), 398–401.
- (5) Kavan, L.; Dousek, F. P.; Micka, K. Time-Dependent Electrical Resistivity of Carbon. *J. Phys. Chem.* **1990**, *94* (12), 5127–5134.
- (6) Nishihara, H.; Harada, H.; Tateishi, M.; Ohashi, K.; Aramaki, K. *New Approach to Graphite Synthesis: Electrochemical Carbonization of Hexachlorobuta-1,3-Diene*; 1991; Vol. 87.
- (7) Wawzonek, S.; Duty, R. C. Polarographic Studies in Acetonitrile and Dimethylformamide: VI . The Formation of Dihalocarbenes . *J. Electrochem. Soc.* **1961**, *108* (12), 1135–1138.
- (8) Lund, H. Electroorganic Preparations. VII. Reduction of a Compound Containing a Trifluoromethyl Group. *Acta Chem. Scand.* **1959**, *13*, 192–194.

- (9) Yan, X. B.; Xu, T.; Yang, S. R.; Liu, H. W.; Xue, Q. J. Characterization of Hydrogenated Diamond-like Carbon Films Electrochemically Deposited on a Silicon Substrate. *J. Phys. D. Appl. Phys.* **2004**, *37* (17), 2416–2424.
- (10) Yan, X. B.; Xu, T.; Chen, G.; Liu, H. W.; Yang, S. R. Effect of Deposition Voltage on the Microstructure of Electrochemically Deposited Hydrogenated Amorphous Carbon Films. *Carbon N. Y.* **2004**, *42* (15), 3103–3108.
- (11) Zhang, G. F.; He, Y. Y.; Hou, X. D. Influence of Additive on Diamond Films Synthesized Using Liquid Phase Electrochemical Method. *Mater. Sci. Forum* **2011**, *687*, 662–666.
- (12) Gupta, S.; Roy, R. K.; Deb, B.; Kundu, S.; Pal, A. K. Low Voltage Electrodeposition of Diamond-like Carbon Films. *Mater. Lett.* **2003**, *57* (22–23), 3479–3485.
- (13) Gupta, S.; Pal Chowdhury, M.; Pal, A. . Synthesis of DLC Films by Electrodeposition Technique Using Formic Acid as Electrolyte. *Diam. Relat. Mater.* **2004**, *13* (9), 1680–1689.
- (14) Casanova, J.; Ebersson, L. Electrochemistry of the Carbon–halogen Bond. In *The Carbon–Halogen Bond (1973)*; John Wiley & Sons, Ltd., 1973; pp 979–1047.
- (15) Robertson, J. Diamond-like Amorphous Carbon. *Mater. Sci. Eng. R Reports* **2002**, *37* (4), 129–281.
- (16) Ferrari, A. C.; Robertson, J. Interpretation of Raman Spectra of Disordered and Amorphous Carbon. *Phys. Rev. B* **2000**, *61* (20), 14095–14107.
- (17) Kavan, L. Electrochemical Carbon. *Chem. Rev.* **1997**, *97* (8), 3061–3082.
- (18) Cançado, L. G.; Takai, K.; Enoki, T.; Endo, M.; Kim, Y. A.; Mizusaki, H.; Jorio, A.;

- Coelho, L. N.; Magalhães-Paniago, R.; Pimenta, M. A. General Equation for the Determination of the Crystallite Size L_a of Nanographite by Raman Spectroscopy. *Appl. Phys. Lett.* **2006**, 88 (16), 163106.
- (19) Wissler, M. Graphite and Carbon Powders for Electrochemical Applications. *J. Power Sources* **2006**, 156 (2), 142–150.
- (20) Radisic, A.; Vereecken, P. M.; Hannon, J. B.; Searson, P. C.; Ross, F. M. Quantifying Electrochemical Nucleation and Growth of Nanoscale Clusters Using Real-Time Kinetic Data. *Nano Lett.* **2006**, 6 (2), 238–242.
- (21) Bockris, J. O.; Kahn, S. U. M. *Surface Electrochemistry: A Molecular Level Approach*; Springer Science & Business Media, 2013.
- (22) Shirakawa, H.; Ito, T.; Ikeda, S. Raman Scattering and Electronic Spectra of Poly(Acetylene). *Polym J* **1973**, 4 (4), 460–462.
- (23) Socrates, G. *Infrared and Raman Characteristic Group Frequencies: Tables and Charts*; 3rd, Ed.; John Wiley & Sons, 2004.
- (24) Kim, J.; Shawky, A.; Yasuda, S.; Murakoshi, K. Selective Synthesis of Graphitic Carbon and Polyacetylene by Electrochemical Reduction of Halogenated Carbons in Ionic Liquid at Room Temperature. *Electrochim. Acta* **2015**, 176, 388–393.

Chapter 3

Synthesis and electrocatalytic activity for nitrogen doped vertically aligned carbon nanotube

3.1 Introduction

I showed selective synthesis of polyacetylene and graphitic carbon by electrochemical deposition in ionic liquid in *Chapter 2*. To develop the synthesis of the other carbon allotropes, I focused on the synthesis of N-doped vertically-aligned carbon nanotube (VA-CNT) and their applications in electrocatalysis in this chapter. In general, electrocatalytic activity can be enhanced by increasing active site and turnover frequency.¹ VA-CNT is densely packed carbon nanotube (CNT) on substrate, and has higher specific surface area than graphene and CNT.^{2,3} Therefore, N-doped VA-CNT possesses the higher active site.

CNT has been prepared by using various synthesis methods such as chemical vapor deposition (CVD), laser ablation, and electrochemical process.⁴⁻⁷ In particular, water-assisted CVD method is widely used for synthesis of VA-CNT. In this method, metal nanoparticles on metal oxide are used as catalysts for VA-CNT growth.⁸⁻¹⁰ Besides, many researchers have used iron (Fe) nanoparticle on aluminum oxide (AlO_x) as catalyst for VA-CNT growth.¹¹ Yamada *et al.* reported size-selective growth of VA-CNT for dependence of Fe nanoparticle.¹² In addition, many carbon sources are used for synthesis of VA-CNT.¹³⁻¹⁵ The diameter of VA-CNT can be controlled by carbon feeding.¹⁶ However, carbon source dependence has not been discussed to date. In this chapter as first purpose, I synthesize the VA-CNT by water-

assisted CVD for carbon source dependence using ethylene (C_2H_4) and hexane (C_6H_{14}). C_2H_4 and C_6H_{14} have different bond dissociation energy from each other, resulting different forms of synthesized VA-CNT.¹⁷ I also characterized the structure of VA-CNT using analysis of specific surface area. Using this VA-CNT, I synthesize the nitrogen-doped VA-CNT (N-VA-CNT), and evaluate the electrocatalytic activity for the second purpose in this chapter. According to related research, heteroatom-doped carbons, such as nitrogen, sulfur, boron, and halogens, have activity for oxygen reduction reaction (ORR) in proton exchange membrane fuel cell (PEMFC).¹⁸⁻²¹ In my previous work, activity for ORR on nitrogen doped graphene is changed by selective formation of structures such as pyridinic and quaternary N as shown in Fig 3.1.²² In this chapter, I use the VA-CNT as carbon substrate which has high surface area. For heteroatom doping on carbon substrate, Ramavathu *et al.* synthesized the cobalt and nitrogen co-doped CNT by pyrolysis process using cobalt phthalocyanine and CNT as cobalt-nitrogen precursor and carbon substrate, respectively.²³ On the basis of results, I used metal free phthalocyanine and VA-CNT as nitrogen precursor and carbon substrate, as well as analyze the atomic structure of N-VA-CNT by X-ray photoelectron spectroscopy (XPS). Finally, I discussed the ORR activity for nitrogen doping dependence on VA-CNT.

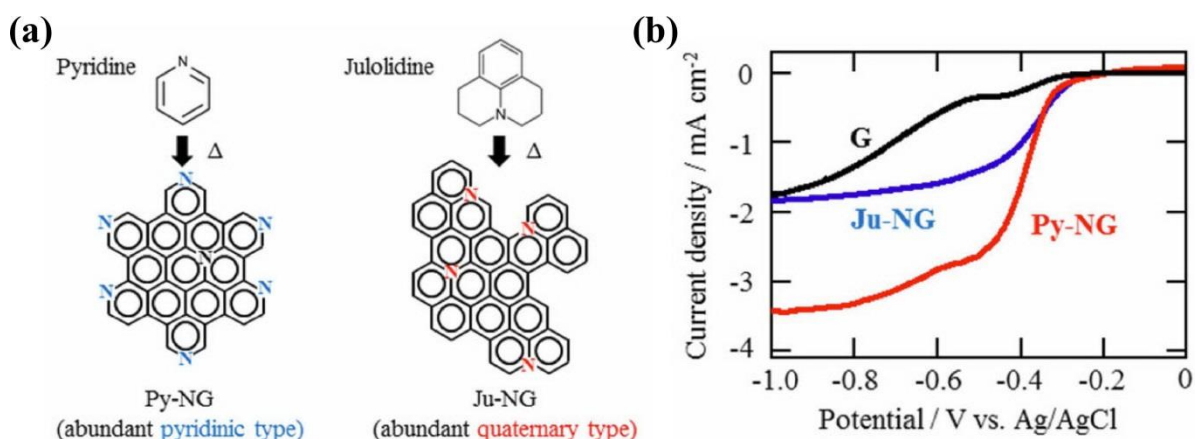


Fig 3.1 (a) Selective nitrogen doping in graphene (left: pyridinic type and right: quaternary type). (b) Linear sweep voltammograms for oxygen reduction reaction (ORR) on pristine graphene, Ju-NG, and Py-NG in an O_2 -saturated 0.1 M KOH solution.

3.2 Experimental methods

3.2.1 Synthesis of vertically aligned carbon nanotube

To prepare the AlO_x film, Al was deposited by evaporation for 25 nm thickness onto a 300 nm thick SiO_2/Si wafer, and baked at 500 °C for 12 hour and 900 °C for 12 hour. Next, Fe nanoparticle was deposited by evaporation for 0.4 nm thickness. Using this substrate, I carried out the water-assisted CVD using *n*-hexane (C_6H_{14} , 98 %, Wako) or ethylene (C_2H_4 , 99 %, Taiyo Nippon Sanso) as carbon source at 800 °C. The Fe-coated $\text{AlO}_x/\text{SiO}_2/\text{Si}$ substrate was placed in a quartz furnace (15 mm inner diameter) as shown in Fig 3.2. VA-CNT was grown on catalyst through formation and growth process. As formation process, carbon source with 7 sccm and H_2O with 7 sccm were dosed during 10 min at 800 °C to generate the carbon nanoparticle. To complete the carbon nanoparticle generation, carbon source with 7 sccm and H_2O with 7 sccm were flowed into the quartz furnace using flowing the Ar gas with 480 sccm as carrier gas, and then carbon growth is possible on the Fe/Al/ SiO_2/Si during 5 min.

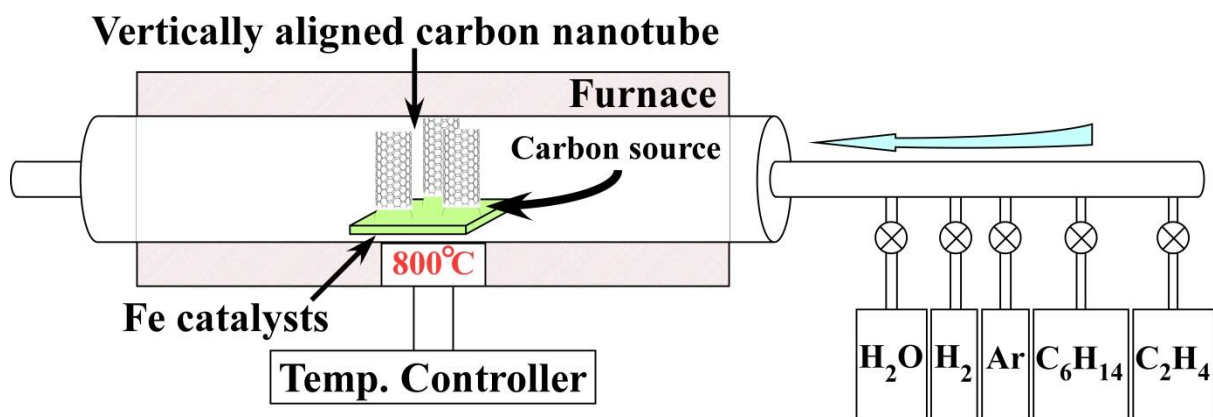


Fig 3.2 Schematic image of chemical vapor deposition system for synthesis of vertically aligned carbon nanotubes

Raman spectroscopy (Thermo Scientific, DXR) and N₂ adsorption-desorption isotherm instrument (Yuasa Ionics Autosorb 6AG) were used to evaluate the structure of VA-CNT. Commercially purchased conventional single walled CNT (diameter: 1.4 ~ 1.6 nm) was used as supporting carbon materials to examine the structural difference from synthesized VA-CNT. 532 nm Excitation wavelength is employed for Raman spectroscopy. Furthermore, samples were heated at 200 °C for 2 hours in vacuum before N₂ adsorption-desorption isotherm analysis for degas treatment. N₂ adsorption-desorption measurement was conducted at 77 K.

3.2.2 Synthesis of nitrogen doped VA-CNT

To prepare the nitrogen doped VA-CNT (N-VA-CNT), phthalocyanine (98 %, TCI) was used as nitrogen precursor as shown in Fig 3.3. Phthalocyanine and VA-CNT were dispersed by ultrasonic homogenizer (Branson Ultrasonics, S-250) at 50 W and 25 kHz in dichloromethane for 30 min. After drying at 80 °C for 12 hours, product was rapidly pyrolyzed at 900 °C for 1 hour in quartz oven with flowing ammonia gas of 150 sccm as supporting nitrogen precursor. And then, composite was prepared by acid treatment in 0.1 M H₂SO₄ for elimination of the contamination. Finally, composite was dried during room temperature and pyrolyzed with aforementioned condition. Atomic analysis of synthesized N-VA-CNT and VA-CNT was evaluated by XPS (JEOL JPS-9200) in ultra-high vacuum system.

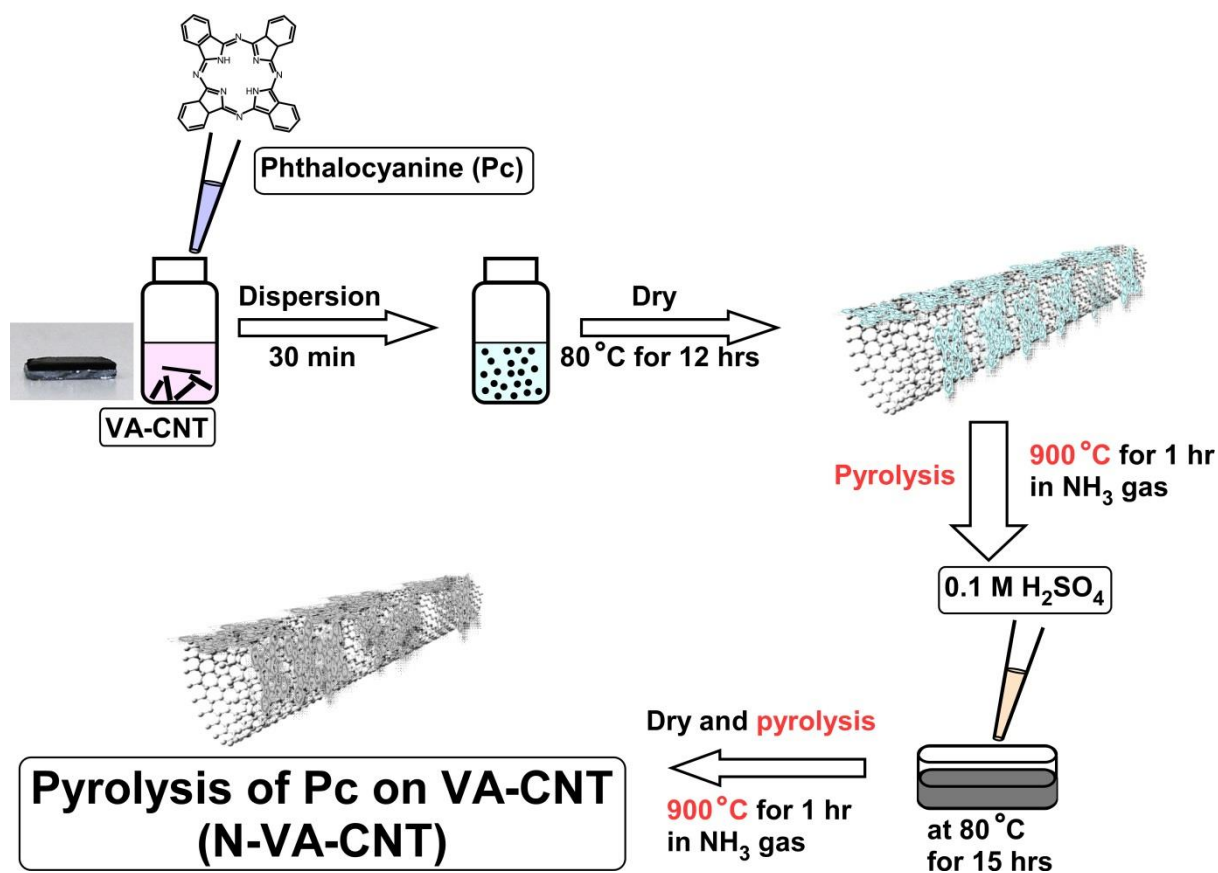


Fig 3.3 Schematic image of procedure for synthesis of nitrogen doped VA-CNT.

3.2.3 Evaluation of ORR catalytic activity

Linear sweep voltammetry (LSV) measurements were recorded using a homemade three-electrode cell using rotating ring disk electrode (RRDE, Hokuto Denko, HR-201) under rotation control (Hokuto Denko, HR-202) and a dual potentiostat (IVIUM, CompactStat). Reversible hydrogen electrode (RHE) and Pt wire were used as the reference and counter electrodes, respectively. The double working electrode was a RRDE, which consisted of a glassy carbon disk (5.0 mm diameter) and Pt ring disk (5.5 and 8.0 mm inner and outer diameters, respectively). Catalyst ink was prepared by sonication of 2.5 mg of catalysts in 50 μL of ethanol, 200 μL of MilliQ water, and 1.25 μL of 5 wt.% Nafion solution for 30 min. 16 microliters of ink were deposited on the glassy carbon (GC) disk and then dried at 60 $^{\circ}\text{C}$ for 6 h, resulting in a catalyst loading of 0.6 mg/cm^2 .

Commercially available Pt/C catalyst (TEC10E50E, 50wt% Pt/C) was also purchased from TKK. 10 mg Pt/C was dispersed in 3 ml ethanol and 10 mL MilliQ water with 50 μL of 5 wt.% Nafion solution by sonication for 30 min, and 10 μL catalyst ink was deposited onto the GC, leading of 20 $\mu\text{g}_{\text{Pt}}/\text{cm}^2$. In case of the acidic condition, LSV and RRDE measurements for Pt/C were carried out in 0.1 M HClO_4 instead of H_2SO_4 aqueous solution to avoid hydrosulfate anion adsorption. For alkaline condition, 0.1 M KOH was used as electrolyte. CV measurements were conducted in O_2 - or Ar-saturated 0.5 M H_2SO_4 and 0.1 M KOH solutions, at a scan rate of 10 mV/s.

LSV in the RRDE test was carried out in O_2 -saturated 0.5 M H_2SO_4 and 0.1 M KOH solutions. Before each measurement, the solution was bubbled with O_2 gas for 30 min, and the Pt ring electrode was activated by sweeping between 0.2 V and 1.4 V at 50 mV/s, until I–V curves were reproducible (typical sweep time ca. 10 min). A potential of the Pt ring disk was set to 1.2 V. The potential of the working electrode was also cycled several times from

0.0 to 1.0 V at 50 mV/s, until similar I–V shapes were observed. Electrochemical data were recorded from 0.0 to 1.0 V, with a scan rate of 10 mV/s and a fixed rotating rate of 1600 rpm. Corrected oxygen reduction currents were obtained by subtracting the background current obtained for the Ar-saturated solution from the measured current obtained for the O₂-saturated solution.

3.3 Results and discussion

3.3.1 Synthesis of vertically aligned carbon nanotube

Fig 3.4 shows Raman spectrum and photographs of VA-CNT and single walled CNT. As a result, radial breathing mode (RBM), D band, G band, and 2D band were found in synthesized VA-CNT. This result indicates that structure of deposited material can be assigned to CNT. In addition, G and D ratio was changed by different carbon source (C₆H₁₄ : 8.1 and C₂H₄ : 4.3). Besides, synthesized VA-CNT has relatively lower G and D ratio than single walled CNT. It is to say that synthesized VA-CNT has relatively larger defect and edge site on CNT than single walled CNT. In case of the RBM band, single walled CNT and VA-CNT (C₆H₁₄) were appeared around 150 ~ 200 cm⁻¹ Raman shift, whereas many peaks were found around 150 ~ 300 cm⁻¹ Raman shift for VA-CNT (C₂H₄) sample. In general, RBM band is diagnostic to diameter of CNT.²⁴ It is known that the Raman shift of RBM band decreased upon increase of diameter of CNT. Therefore, VA-CNT (C₆H₁₄) has larger diameter (1.5 ~ 1.6 nm) of CNT than VA-CNT (C₂H₄) with 0.8 ~ 1.4 nm. In particular, VA-CNT (C₂H₄) has many difference diameters of CNT. This result is also consistent with the relatively low G and D ratio, as well as shoulder of Raman peak from 1400 cm⁻¹ to 1600 cm⁻¹.

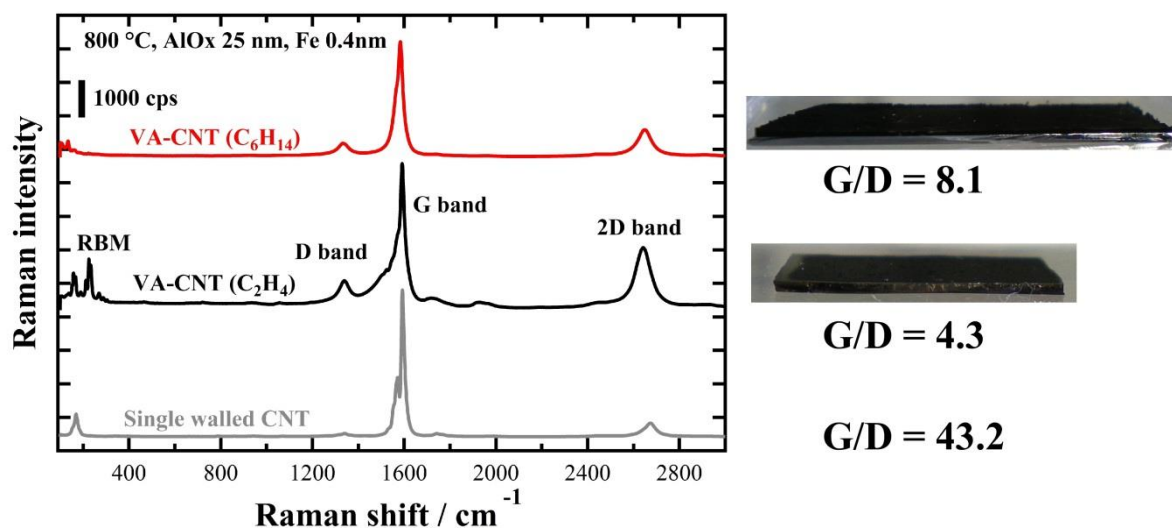


Fig 3.4 Raman spectra for synthesized VA-CNT using hexane (C_6H_{14} , red line) and ethylene (C_2H_4 , black line) as carbon source. Raman spectrum of commercially purchased single walled CNT (grey line) as reference sample. Laser excitation wavelength: 532 nm.

To evaluate the specific surface area, Fig 3.5 shows curves of N_2 adsorption-desorption isotherm for synthesized VA-CNTs and single walled CNT. As a result, hysteresis loop was observed for all of the samples, which is multilayer adsorption on mesoporous and macroporous structures by capillary condensation.²⁴ In addition, specific surface areas for VA-CNT (C_2H_4) and VA-CNT (C_6H_{12}) were $954 \text{ m}^2/\text{g}$ and $1120 \text{ m}^2/\text{g}$, respectively (Table 3.1). This result shows that specific surface area of synthesized VA-CNTs was dramatically increased than one of single walled CNT. According to related research, specific surface area of graphene was $350 \text{ m}^2/\text{g}$.²⁵ Therefore, VA-CNT has more advantage for specific surface area than graphene as carbon substrate. Besides, VA-CNT (C_6H_{12}) has higher specific surface area than VA-CNT (C_2H_4). This result implies that VA-CNT (C_2H_4) has more defect site than VA-CNT (C_6H_{14}), resulting in low specific surface area. Because C_2H_4 is composed of carbon double bond ($C=C$ bond dissociation energy: $172.2 \text{ kJ mol}^{-1}$), carbon decomposition is more insufficient than C_6H_{14} ($C-C$ bond dissociation energy: 89.7 kJ mol^{-1}) resulting low quality of VA-CNT.

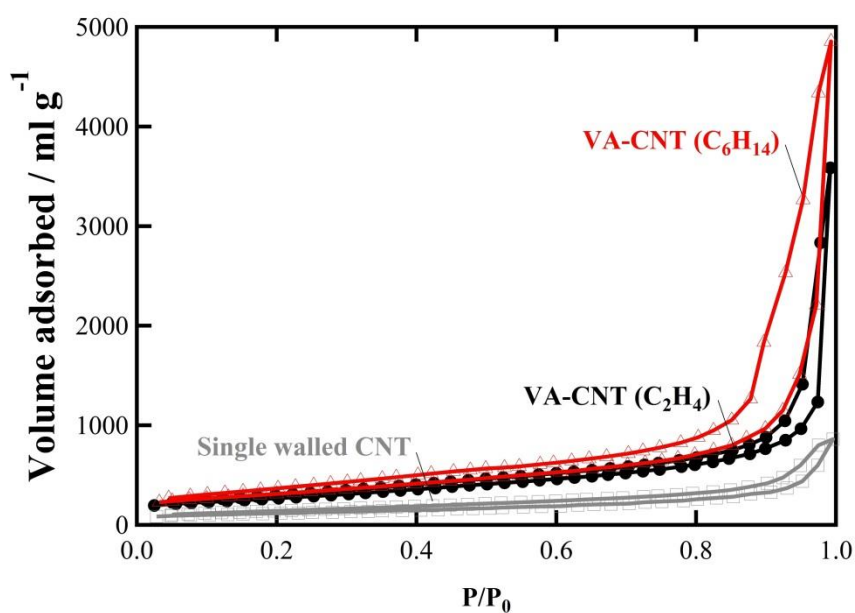


Fig 3.5 N₂ adsorption-desorption isotherm of synthesized VA-CNT (C₆H₁₄ and C₂H₄ as carbon source) and commercially purchased single walled carbon nanotube at 77K.

Table 3.1 Specific surface area for VA-CNT (C₆H₁₄ and C₂H₄ as carbon source) and commercially purchased single walled carbon nanotube

Sample	Specific surface area
VA-CNT (C ₆ H ₁₄)	1120 m ² /g
VA-CNT (C ₂ H ₄)	954 m ² /g
Single-walled CNT	406 m ² /g

3.3.2 Synthesis of nitrogen doped vertically aligned carbon nanotube

Next, to develop the carbon material, N-VA-CNT was synthesized by pyrolysis process using phthalocyanine on VA-CNT. VA-CNT (C_6H_{14}) was used as carbon substrate because of high specific surface area. To verify the nitrogen-doping, N-VA-CNT was evaluated by XPS as shown in Fig 3.6 (a). As a result, XPS peak for N-VA-CNT was appeared around N 1s range, whereas any peaks for VA-CNT was not found from 390 eV to 408 eV. Therefore, I successfully synthesized the nitrogen-doped VA-CNT. In particular, XPS peak for N-VA-CNT is deconvoluted from many nitrogen-graphene forms such as pyridinic (398.5 eV), pyrrolic (400.1 eV), quaternary N (401.3 eV), and nitrogen oxide (403.1 eV).²⁵ This result shows that nitrogen-graphene structure is kept and covered on VA-CNT through the calcination of phthalocyanine on VA-CNT surface.

In case of the Raman spectroscopy, D band for N-VA-CNT was relatively increased in comparison with result of VA-CNT as shown in Fig 3.6 (b). This result implies that defect site is increased by pyrolysis process at 900 °C because D band originates from the defect site. In addition, RBM band was significantly decreased from 150 to 200 cm^{-1} Raman shift. This result indicates that nitrogen-graphene structure is covered on VA-CNT, resulting in blocking the vibration of RBM.

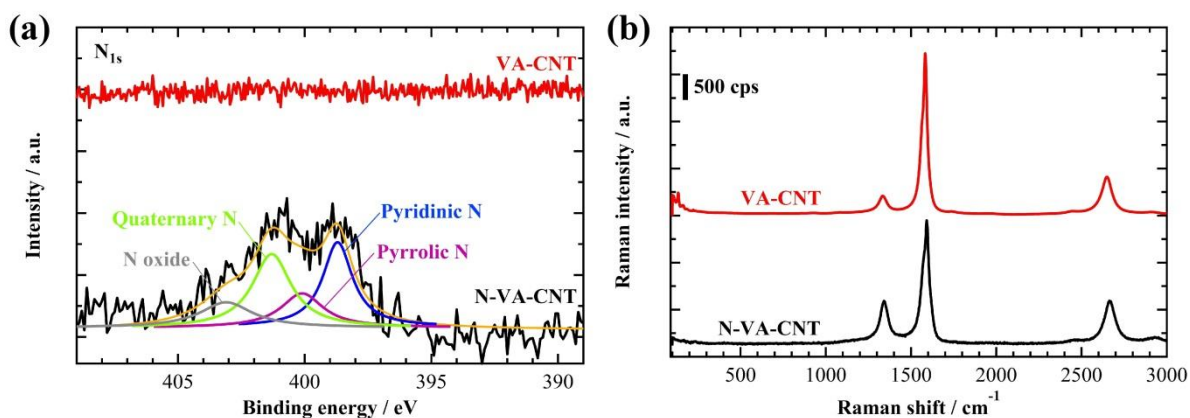


Fig 3.6 (a) Results of XPS around N 1s range and (b) Raman spectra for VA-CNT (red line) and N-VA-CNT (black line). Laser excitation wavelength of Raman spectra: 532 nm.

3.3.3 Nitrogen doped VA-CNT for ORR electrocatalysis

To evaluate the electrochemical activity for ORR in acidic condition, linear sweep voltammetry and analysis of reaction electron number in Fig 3.7 (a) and (b). In case of the Pt/C, onset potential and limiting current density were observed for 0.98 V (vs. RHE) and -5.7 mA/cm², respectively. Besides, reaction electron number of Pt/C was 4.0, resulting in high performance for ORR. For the carbon-based catalyst, VA-CNT and N-VA-CNT have lower limiting current density and reaction electron number than Pt/C. In particular, current density was dramatically increased and onset potential was shift toward positive potential by nitrogen doping on VA-CNT. Reaction electron numbers for N-VA-CNT and VA-CNT were 3.6 and 2.8 at 0.0 V (vs. RHE). For the alkaline condition (Fig 3.7 (c) and (d)), similar tendency was shown in LSV curves and curves of reaction electron number versus potential. Reaction electron numbers for N-VA-CNT and VA-CNT were 3.2 and 2.9 at 0.0 V (vs. RHE). In addition, onset potential positively was shift by nitrogen doping on VA-CNT. This result shows that ORR activity is enhanced by nitrogen doping on VA-CNT.

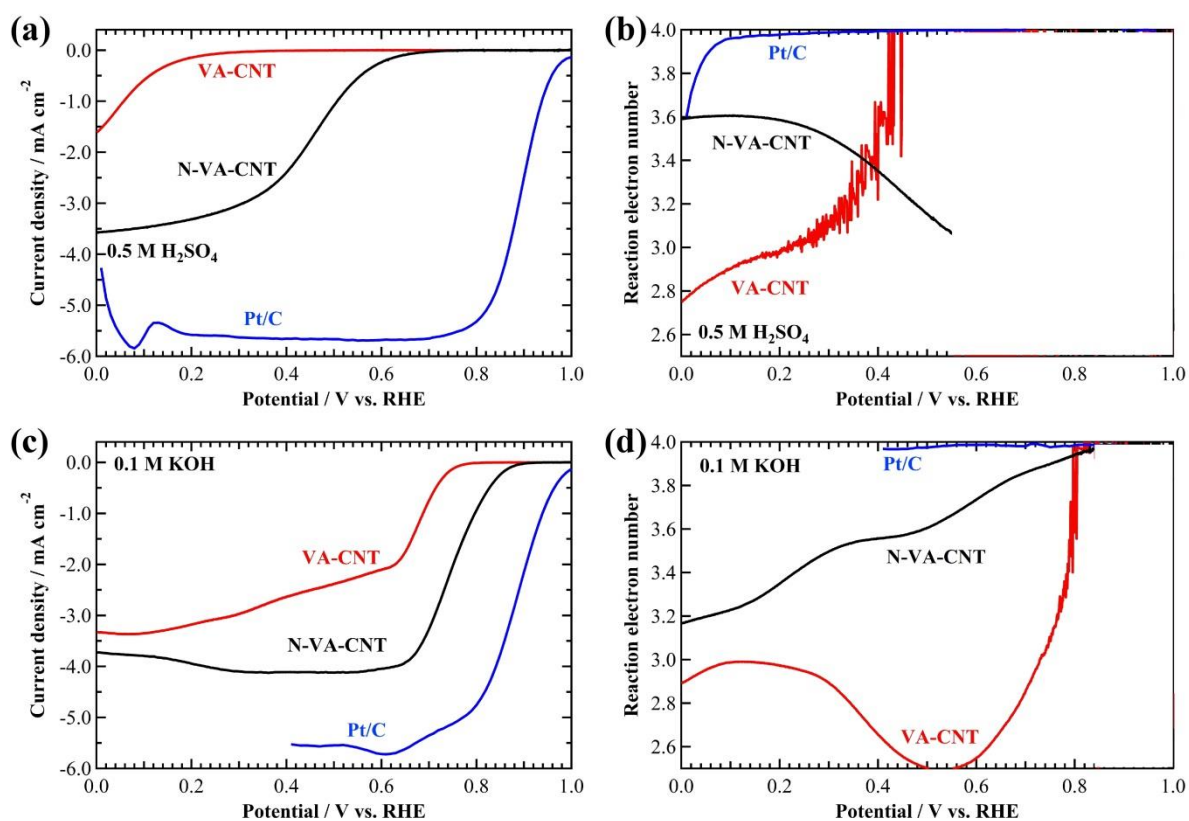


Fig 3.7 (a, c) Linear sweep voltammograms and (b, d) curves of reaction electron number versus potential on VA-CNT (red line), N-VA-CNT (black line), and Pt/C (blue line) in acidic condition (a, b, 0.5 M H₂SO₄) and alkaline condition (c, d, 0.1 M KOH). 0.1M H₂ClO₄ is used for Pt/C sample instead of 0.5 M H₂SO₄

3.4 Conclusion

In conclusion, I synthesized the VA-CNT by water-assisted CVD using *n*-hexane (C_6H_{14}) and ethylene (C_2H_4). As a result, synthesized VA-CNTs has relatively higher D band than commercially purchased single walled CNT from Raman spectroscopy. Besides, structure of VA-CNT depends on carbon source. In case of the VA-CNT (C_2H_4), various diameters of CNTs are formed, resulting in many RBM peaks from 150 cm^{-1} to 300 cm^{-1} Raman shift. On the other hand, VA-CNT (C_6H_{14}) has two peaks from 150 cm^{-1} to 200 cm^{-1} Raman shift. D band for VA-CNT (C_2H_4) is larger than that of VA-CNT (C_6H_{14}). From result of N_2 adsorption-desorption, VA-CNT (C_6H_{14}) has higher specific surface area than VA-CNT (C_2H_4). Therefore, VA-CNT (C_6H_{14}) has higher quality than VA-CNT (C_2H_4). This result implies that carbon nanoparticle from C_6H_{14} is easily formed by CVD process because C_6H_{14} has only single bond of C-C and C-H. On the other hand, C_2H_4 has double bond (C=C) and single bond of C-H, resulting in formation of defect site by insufficient temperature of CVD.

To develop the application of carbon based electrocatalyst, I synthesized the N-VA-CNT by pyrolysis using phthalocyanine with VA-CNT. In case of the XPS result, N-VA-CNT has the peak around N 1s range. Besides, RBM band is not shown and D band is increased by nitrogen doping on VA-CNT. This result is expected that N-graphene structure covered on VA-CNT, resulting in blocking the RBM mode. To evaluate the ORR activity, LSV and reaction electron number analysis are investigated in acidic and alkaline electrolytes. As a result, ORR activity is enhanced by nitrogen doping on VA-CNT. From the XPS result, N-VA-CNT has many N-graphene forms such as pyridinic N, pyrrolic N, quaternary N, and nitrogen oxide. In the previous work, ORR can be activated on the pyridinic N and quaternary N.²² On the basis of the result, activity of ORR is changeable for N-graphene structure. Therefore, N-VA-CNT would be used as precious metal free ORR catalyst.

3.5 Reference

- (1) Gasteiger, H. A.; Kocha, S. S.; Sompalli, B.; Wagner, F. T. Activity Benchmarks and Requirements for Pt, Pt-Alloy, and Non-Pt Oxygen Reduction Catalysts for PEMFCs. *Appl. Catal. B Environ.* **2005**, *56* (1–2), 9–35.
- (2) Hata, K.; Futaba, D. N.; Mizuno, K.; Namai, T.; Yumura, M.; Iijima, S. Water-Assisted Highly Efficient Synthesis of Impurity-Free Single-Walled Carbon Nanotubes. *Science* (80-.). **2004**, *306* (5700), 1362 LP-1364.
- (3) Chen, H.; Roy, A.; Baek, J.-B.; Zhu, L.; Qu, J.; Dai, L. Controlled Growth and Modification of Vertically-Aligned Carbon Nanotubes for Multifunctional Applications. *Mater. Sci. Eng. R Reports* **2010**, *70* (3–6), 63–91.
- (4) Bower, C.; Zhou, O.; Zhu, W.; Werder, D. J.; Jin, S. Nucleation and Growth of Carbon Nanotubes by Microwave Plasma Chemical Vapor Deposition. *Appl. Phys. Lett.* **2000**, *77* (17), 2767–2769.
- (5) Scott, C. D.; Arepalli, S.; Nikolaev, P.; Smalley, R. E. Growth Mechanisms for Single-Wall Carbon Nanotubes in a Laser-Ablation Process. *Appl. Phys. A Mater. Sci. Process.* **2001**, *72* (5), 573–580.
- (6) Iijima, S.; Ichihashi, T. Single-Shell Carbon Nanotubes of 1-Nm Diameter. *Nature* **1993**, *363* (6430), 603–605.
- (7) Shawky, A.; Yasuda, S.; Murakoshi, K. Room-Temperature Synthesis of Single-Wall Carbon Nanotubes by an Electrochemical Process. *Carbon N. Y.* **2012**, *50* (11), 4184–4191.
- (8) Huang, L.; White, B.; Sfeir, M. Y.; Huang, M.; Huang, H. X.; Wind, S.; Hone, J.;

- O'Brien, S. Cobalt Ultrathin Film Catalyzed Ethanol Chemical Vapor Deposition of Single-Walled Carbon Nanotubes. *J. Phys. Chem. B* **2006**, *110* (23), 11103–11109.
- (9) Yun, Y.; Shanov, V.; Tu, Y.; Subramaniam, S.; Schulz, M. J. Growth Mechanism of Long Aligned Multiwall Carbon Nanotube Arrays by Water-Assisted Chemical Vapor Deposition. *J. Phys. Chem. B* **2006**, *110* (47), 23920–23925.
- (10) Yoshihara, N.; Ago, H.; Tsuji, M. Chemistry of Water-Assisted Carbon Nanotube Growth over Fe–Mo/MgO Catalyst. *J. Phys. Chem. C* **2007**, *111* (31), 11577–11582.
- (11) Kaneko, A.; Yamada, K.; Kumahara, R.; Kato, H.; Homma, Y. Comparative Study of Catalytic Activity of Iron and Cobalt for Growing Carbon Nanotubes on Alumina and Silicon Oxide. *J. Phys. Chem. C* **2012**, *116* (49), 26060–26065.
- (12) Yamada, T.; Namai, T.; Hata, K.; Futaba, D. N.; Mizuno, K.; Fan, J.; Yudasaka, M.; Yumura, M.; Iijima, S. Size-Selective Growth of Double-Walled Carbon Nanotube Forests from Engineered Iron Catalysts. *Nat. Nanotechnol.* **2006**, *1* (2), 131–136.
- (13) Weiss, T.; Zielasek, V.; Bäumer, M. Influence of Water on Chemical Vapor Deposition of Ni and Co Thin Films from Ethanol Solutions of Acetylacetonate Precursors. *Sci. Rep.* **2016**, *5* (1), 18194.
- (14) Nishino, H.; Yasuda, S.; Namai, T.; Futaba, D. N.; Yamada, T.; Yumura, M.; Iijima, S.; Hata, K. Water-Assisted Highly Efficient Synthesis of Single-Walled Carbon Nanotubes Forests from Colloidal Nanoparticle Catalysts †. *J. Phys. Chem. C* **2007**, *111* (48), 17961–17965.
- (15) Yu, M.; Funke, H. H.; Falconer, J. L.; Noble, R. D. High Density, Vertically-Aligned Carbon Nanotube Membranes. *Nano Lett.* **2009**, *9* (1), 225–229.

- (16) Lu, C.; Liu, J. Controlling the Diameter of Carbon Nanotubes in Chemical Vapor Deposition Method by Carbon Feeding. *J. Phys. Chem. B* **2006**, *110* (41), 20254–20257.
- (17) Zavitsas, A. A. The Relation between Bond Lengths and Dissociation Energies of Carbon–Carbon Bonds. *J. Phys. Chem. A* **2003**, *107* (6), 897–898.
- (18) Yasuda, S.; Furuya, A.; Uchibori, Y.; Kim, J.; Murakoshi, K. Iron-Nitrogen-Doped Vertically Aligned Carbon Nanotube Electrocatalyst for the Oxygen Reduction Reaction. *Adv. Funct. Mater.* **2016**, *26* (5), 738–744.
- (19) Zhao, Y.; Yang, L.; Chen, S.; Wang, X.; Ma, Y.; Wu, Q.; Jiang, Y.; Qian, W.; Hu, Z. Can Boron and Nitrogen Co-Doping Improve Oxygen Reduction Reaction Activity of Carbon Nanotubes? *J. Am. Chem. Soc.* **2013**, *135* (4), 1201–1204.
- (20) Liang, J.; Jiao, Y.; Jaroniec, M.; Qiao, S. Z. Sulfur and Nitrogen Dual-Doped Mesoporous Graphene Electrocatalyst for Oxygen Reduction with Synergistically Enhanced Performance. *Angew. Chemie Int. Ed.* **2012**, *51* (46), 11496–11500.
- (21) Ishizaki, T.; Wada, Y.; Chiba, S.; Kumagai, S.; Lee, H.; Serizawa, A.; Li, O. L.; Panomsuwan, G. Effects of Halogen Doping on Nanocarbon Catalysts Synthesized by a Solution Plasma Process for the Oxygen Reduction Reaction. *Phys. Chem. Chem. Phys.* **2016**, *18* (31), 21843–21851.
- (22) Yasuda, S.; Yu, L.; Kim, J.; Murakoshi, K. Selective Nitrogen Doping in Graphene for Oxygen Reduction Reactions. *Chem. Commun.* **2013**, *49* (83), 9627.
- (23) Ramavathu, L. N.; Maniam, K. K.; Gopalram, K.; Chetty, R. Effect of Pyrolysis Temperature on Cobalt Phthalocyanine Supported on Carbon Nanotubes for Oxygen

Reduction Reaction. *J. Appl. Electrochem.* **2012**, *42* (11), 945–951.

(24) Dresselhaus, M. S.; Dresselhaus, G.; Saito, R.; Jorio, A. Raman Spectroscopy of Carbon Nanotubes. *Phys. Rep.* **2005**, *409* (2), 47–99.

(25) Li, X.; Chen, Y.; Cheng, Z.; Jia, L.; Mo, S.; Liu, Z. Ultrahigh Specific Surface Area of Graphene for Eliminating Subcooling of Water. *Appl. Energy* **2014**, *130*, 824–829.

Chapter 4

Synthesis and electrocatalytic activity for fluorine-doped carbon

4.1 Introduction

In Chapter 3, I studied the electrocatalytic activity of oxygen reduction reaction of nitrogen-doped vertically aligned carbon nanotube. To create the other carbon-based catalyst, in this chapter, I attempt to synthesize fluorine-doped carbon and evaluate the oxygen evolution reaction (OER) of fluorine-doped carbon. Electrochemical energy conversion and storage systems have attractive potential for clean energy applications. As an energy conversion system, electrochemical water splitting has been used to produce hydrogen.¹ In such a system, the hydrogen evolution reaction (HER) proceeds simultaneously with OER at the cathode and anode, respectively.² It is known that the efficiency of electrochemical water splitting is limited by the activity of the OER because it is a 4-electron reaction in comparison with the 2-electron reaction of HER, which results in a much higher overpotential.³ Conventionally, precious metal oxides, such as ruthenium oxide (RuO₂) and iridium oxide (IrO₂), are widely used as catalysts for OER owing to their inherent catalytic properties.^{4,5} However, the precious metal oxides are expensive and are in limited commercial supply.

Metal-free heteroatom-doped carbon has come into focus as catalysts for OER owing to its abundance, low cost and high electric conductivity. For example, Hashimoto *et al.* reported that nitrogen-doped carbon exhibits catalytic activity for

OER.⁶ Furthermore, the OER activity of nitrogen-doped carbon can be enhanced by increasing the quantity of pyridinic and quaternary nitrogen. In these nitrogen-doped carbons, positively charged carbon atoms act as active sites of OER because OH⁻ in the electrolyte have lower adsorption energy on the positively charged active sites.⁶

Among the heteroatom-doped carbons, fluorine-doped carbon has been studied as an OER catalysts using density functional theory (DFT) as shown in Fig 4.1.^{7,8} Fluorine atoms have the highest electronegativity among all the elements, therefore they induce the highest positive charge on carbon atoms when they are bonded, which has great potential for the OER.⁹ In normal DFT study, the carbon atom bonded to fluorine was in sp³ hybridization, which resulted in the “covalent” C-F bond.^{7,8} However, the C-F bond can also be “ionic” or “semi-ionic”. An ionic C-F bond appears on a carbon atom of sp² hybridization on a graphene structure, whereas a semi-ionic C-F bond is an intermediate state between covalent and ionic bond.^{10,11} In

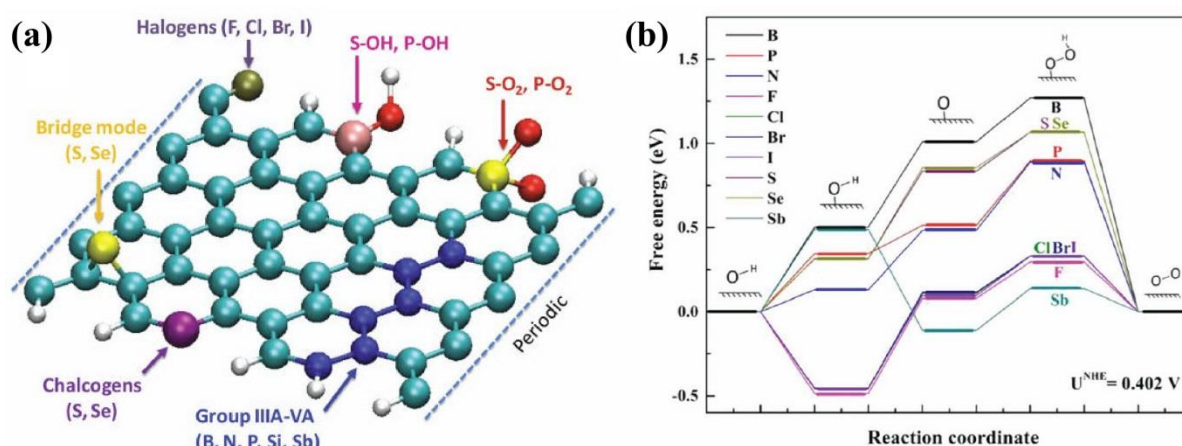


Fig 4.1 (a) Schematic design of the X-doped graphene nanoribbons, showing the possible position of dopants. (b) Free energy diagram of graphene with the best catalytic performance at the equilibrium potential ($U^0 = 0.402$ V) for oxygen evolution reaction in alkaline electrolyte.

general, semi-ionic bonds have higher polarities than covalent C-F bonds, which result in higher positive charge on carbon atoms.¹² Therefore, the fluorine-doped carbon with semi-ionic C-F bonds should have a greater activity for OER than that with the covalent C-F bonds.

Various fluorine precursors have been used to synthesize fluorine-doped carbon.^{11,13-15} In a previous work, fluorine-doped graphite was synthesized by a long-time reactor process using fluorine gas, which resulted in the formation of ionic and covalent C-F bonds.^{13,16} In another method, solution plasma synthesis was performed using trifluorotoluene as the fluorine precursor.¹⁴ As a result, the synthesized fluorine-doped carbon had a high semi-ionic C-F ratio. The OER activity of fluorine-doped carbon has not been studied to date. The relationship between the OER activity and the characteristics of C-F bonds is unclear.

In this chapter, I evaluated the OER activity of fluorine-doped carbon. Nafion was used as the fluorine precursor. *In-situ* O₂ monitoring voltammetry was used for the evaluation of the OER activity of the catalysis. The ionicity of C-F bond in the catalysis was determined by X-ray photoelectron spectroscopy (XPS) to evaluate the correlation between the C-F bonding and the activity. Furthermore, I evaluated the OER activity for pH dependence on fluorine-doped carbon. pH dependence study provides the mechanistic insight for the electrocatalysis from the potential versus current plot (Tafel plot), and proton order.¹⁷ Therefore, I discussed the possible mechanism for OER using pH dependence.

4.2 Experimental methods

Nafion (5% dispersion solution), KB (EC-600JD), and RuO₂ (99.9%) were purchased from Wako Pure Chemical Industries, LTD., Lion Special Chemicals Co., LTD., and Sigma-Aldrich, respectively. In a typical synthesis of F-KB with a mass ratio between Nafion and KB of 40 : 1 (40F-KB), Nafion (400 μ L) and KB (10 mg) were dispersed using an ultrasonication homogenizer (SMT UH-50F) at 50 W and 20 kHz in methanol (10 mL) for 30 min. After drying overnight at 60 $^{\circ}$ C, the mixture was pyrolyzed in Ar (200 sccm) for 1 hour at various temperatures such as 400 $^{\circ}$ C, 500 $^{\circ}$ C, 600 $^{\circ}$ C, 700 $^{\circ}$ C, and 800 $^{\circ}$ C as shown in Fig 4.2. KB was also heated at 600 $^{\circ}$ C for 1 hour before electrochemical measurement.

To evaluate the Nafion usage dependence, Nafion usage is reflected in the name of samples, such as 10F-KB (Nafion 100 μ L to KB 10 mg), 20F-KB (Nafion 200 μ L to KB 10 mg), and 40F-KB (Nafion 400 μ L to KB 10 mg). Pyrolysis temperature was set at 600 $^{\circ}$ C.

The sample (1 mg) was dispersed in ethanol (40 μ L) and deionized water (160 μ L) using an ultrasonic homogenizer for 10 min. Nafion (2 μ L) was then added to the composite ink and dispersed by the ultrasonic homogenizer for 1 min. The catalyst (8.3 μ L) was loaded onto a rotation disk electrode (RDE) as the working electrode. The RDE has a glassy carbon disk of diameter of 0.5 cm (catalyst loading: 0.2 mg cm⁻²).

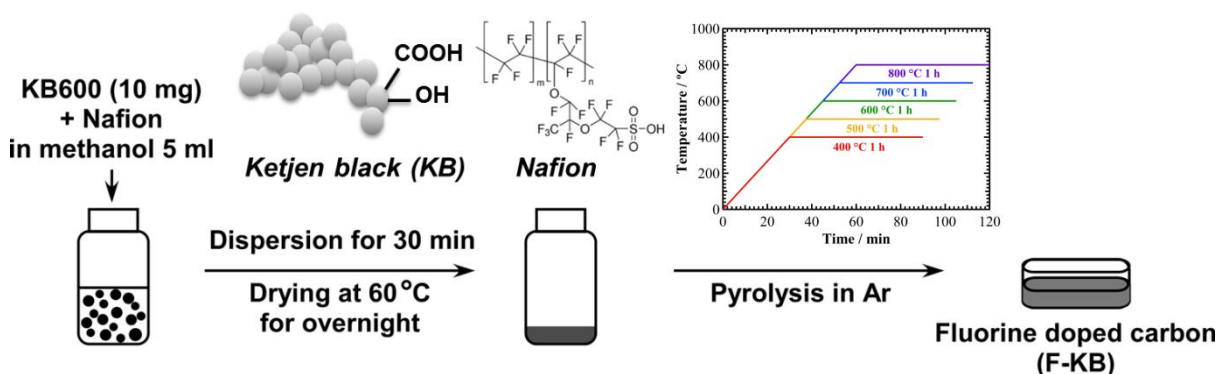


Fig 4.2 Synthesis procedure for fluorine doped carbon (F-KB).

The electrochemical cell was equipped with a dissolved O₂ detector (Pyroscience OXROB10), the working electrode, a Pt counter electrode, a reversible hydrogen electrode (RHE) as the reference electrode and 0.1 M KOH as electrolyte as shown in Fig 4.3 (a). KB and F-KBs were pre-treated by chronoamperometry at a constant potential of 1.6 V for 1 min to avoid the current from carbon oxidation in OER. To minimize the dissolved O₂ before measurements, the electrolyte was bubbled with Ar gas. Background O₂ concentration was subtracted from all data of O₂ concentration versus time. Linear sweep hydrodynamic voltammetry was performed from 1.0 V to 1.6 V with a scan rate of 10 mV s⁻¹. Rotation speed of the RDE was maintained at 1600 rpm. Dissolved O₂ concentration was recorded at 1.6 V for 10 min.

The distance between the dissolved O₂ detector and working electrode was set as approximately 5 mm. The O₂ detector is consist of a pair of blue and red light-emitting diodes (LEDs) and a silicon photodetector as shown in Fig 4.3 (b). O₂ concentration can be measured by the luminescence quenching between oxygen molecules and luminescent dye.¹⁸ The luminescent dye is excitable with orange-red light between wavelength ranging in 610-630 nm and exhibits oxygen-dependent luminescence in the range of 760-790 nm of near infrared.

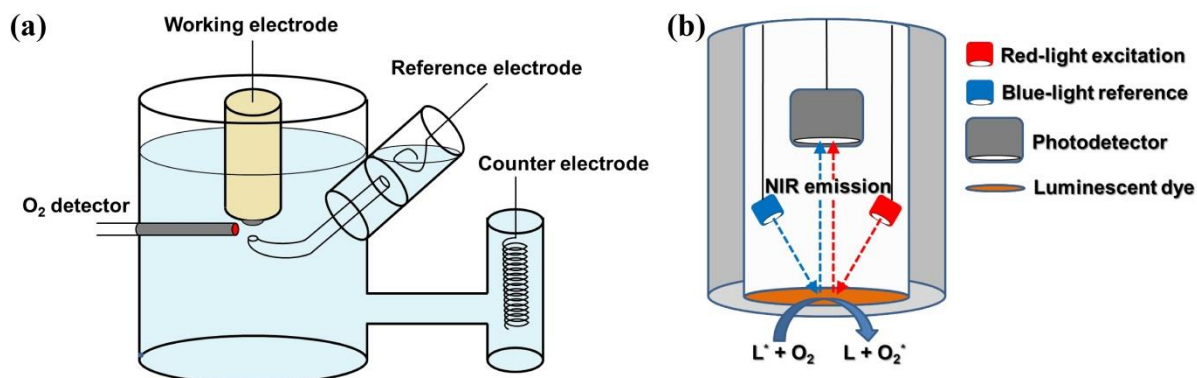


Fig 4.3 (a) Schematic image of electrochemical cell with O₂ detector. Reference electrode (reversible hydrogen electrode, RHE) and counter electrode (Pt wire). (b) Schematic configuration of O₂ detector.

X-ray photoelectron spectroscopy (XPS) was conducted using a JEOL JPS-9200 with a monochromatic Al K α X-ray source (1486.6 eV). O 1s at 531.0 eV was used as internal standard peak for XPS measurements. N₂ adsorption-desorption isotherms were obtained by using a Yuasa Ionics Autosorb 6AG at 77 K. Specific surface areas were estimated by the Brunauer–Emmett–Teller (BET) method. Raman spectra were recorded from 300 to 3200 cm⁻¹ with Nanofinder 30 (Tokyo Instrument, Inc.) using a 514 nm laser beam.

Density functional theory (DFT) calculations were carried out by the use of the Gaussian 03, at the B3LYP level of DFT with 6-31G** basis sets. Molecular model was treated as C₄₂H₁₆ for nanographene. The model structure was constructed by using the Avogadro package and structure was optimized by thermal quenching method. Thereafter, initial structure of molecular model was optimized by using “opt” command in Gaussian. Atomic coordinates are shown in appendix.

4.3 Results and discussion

4.3.1 OER activity for fluorine doped carbon with different pyrolysis temperature

Fig 4.4 (a) shows linear sweep voltammogram of 40F-KB 600 °C and KB without electrochemical pretreatment. As a result, KB exhibited the lowest current density of 1.0 mA cm⁻² at potential of 1.6 V, whereas current density for 40F-KB 600 °C was 5.1 mA cm⁻². In particular, current density for 40F-KB 600 °C was relatively increased than one for RuO₂ at 1.4 V. To verify the O₂ concentration for 40F-KB 600 °C at 1.4 V, O₂ concentration versus time curve for 40F-KB 600 °C and KB is recorded by constant potential 1.6 V and 1.4 V as shown in Fig 4.4 (b). In the case of the pristine KB, the O₂ concentration change was not observed over the 10 min. In addition, the oxygen concentration for 40F-KB 600 °C does not increase at 1.4 V (Fig 4.4 dotted line), therefore, the anodic current of 40F-KBs at 1.4 V corresponds to catalyst decomposition. OER occurs on 40F-KBs at 1.6 V, evidenced by the increase of O₂ concentration.

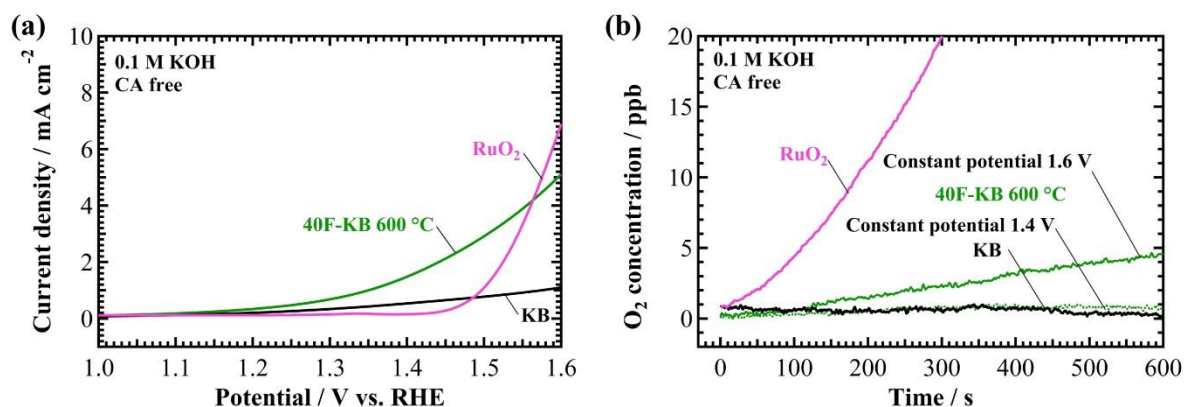


Fig 4.4 (a) Linear sweep voltammogram and (b) O₂ concentration versus time for 40F-KB 600 °C, RuO₂, and KB on RDE (1600 rpm) in 0.1 M KOH for chronoamperometry treatment free condition. Scan rate (10 mV s⁻¹). Constant potential of 1.6 V (Solid line) and 1.4 V (Dotted line).

Fig 4.5 (a) shows the linear sweep hydrodynamic voltammograms of KB and F-KB after electrochemical pretreatment. The catalyst loading was 0.2 mg cm^{-2} for all samples. KB exhibited the lowest current density of 0.8 mA cm^{-2} at potential of 1.6 V, whereas the current density of 40F-KB was 2.6 mA cm^{-2} . These results showed that the electrochemical activity of the KB can be enhanced by fluorine doping. According to related studies, the OER current densities of phosphorus-doped graphene and nitrogen-phosphorus-doped graphene were 19 mA cm^{-2} and 4 mA cm^{-2} at 1.6 V versus RHE, respectively (catalyst loading: 0.2 mg cm^{-2}).^{19,20} Surface-oxidized multi-walled carbon nanotubes had a current density of 0.8 mA cm^{-2} at 1.6 V versus RHE (catalyst loading: 1 mg cm^{-2}).²¹ 40F-KB showed a relatively lower activity than nitrogen- or phosphorus-doped carbon, but a higher current density than the oxygen-doped carbon. In the case of RuO_2 , the current density was approximately 6.5 mA cm^{-2} at 1.6 V.

Next, I evaluated the evolved O_2 by *in-situ* measurement with an O_2 detector at a constant potential of 1.6 V for 10 min after electrochemical pretreatment as shown in Fig 4.5 (b). In the case of the pristine KB, the O_2 concentration change was not observed over the 10 min. However, the O_2 concentration from 40F-KB gradually increased to approximately 3.7 ppb after 10 min. The increment of the O_2 concentration for RuO_2 was approximately 40 ppb over 10 min. Hence, 40F-KB has a catalytic activity of approximately 10% that of RuO_2 . The results prove that the catalytic activity for OER can be enhanced by fluorine doping on an inactive carbon substrate.

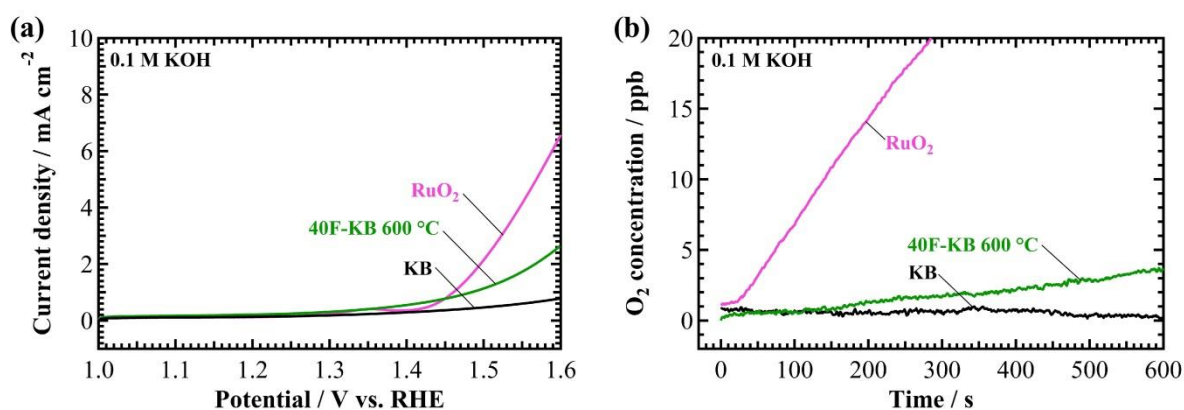


Fig 4.5 (a) Linear sweep voltammogram and (b) O₂ concentration versus time for 40F-KB 600 °C, RuO₂, and KB on RDE (1600 rpm) in 0.1 M KOH after electrochemical pretreatment. Scan rate (10 mV s⁻¹)

To verify the OER activity of F-KB with various synthetic conditions, different pyrolysis temperatures were employed. The pyrolysis temperatures were set at 400 °C, 500 °C, 600 °C, 700 °C, and 800 °C. Linear sweep hydrodynamic voltammetry of different 40F-KBs were performed and the results are shown in Fig. 4.6 (a, c, e, g, i). 40F-KB 600 °C and 40F-KB 700 °C exhibited higher OER current densities than KB. Other 40F-KBs had lower OER current densities than KB. I also confirmed similar tendency in the increment of the O₂ concentration at a constant potential of 1.6 V, as shown in Fig 4.6 (b, d, f, h, j). The noise for the O₂ concentration measurement was approximately 0.3 ppb. The 40F-KB 400 °C exhibited no higher O₂ concentration than the noise (Fig 4.6 (b)). The O₂ concentrations of the 500 °C and 800 °C samples slightly increased over 10 min as shown in Fig 4.6 (d) and (j). However, the O₂ concentration of the 600 °C and 700 °C samples increased by over 1.7 ppb over 10 min (Fig 4.6 (f) and (h)). These results showed that catalytic activity for OER can be affected by the pyrolysis temperature.

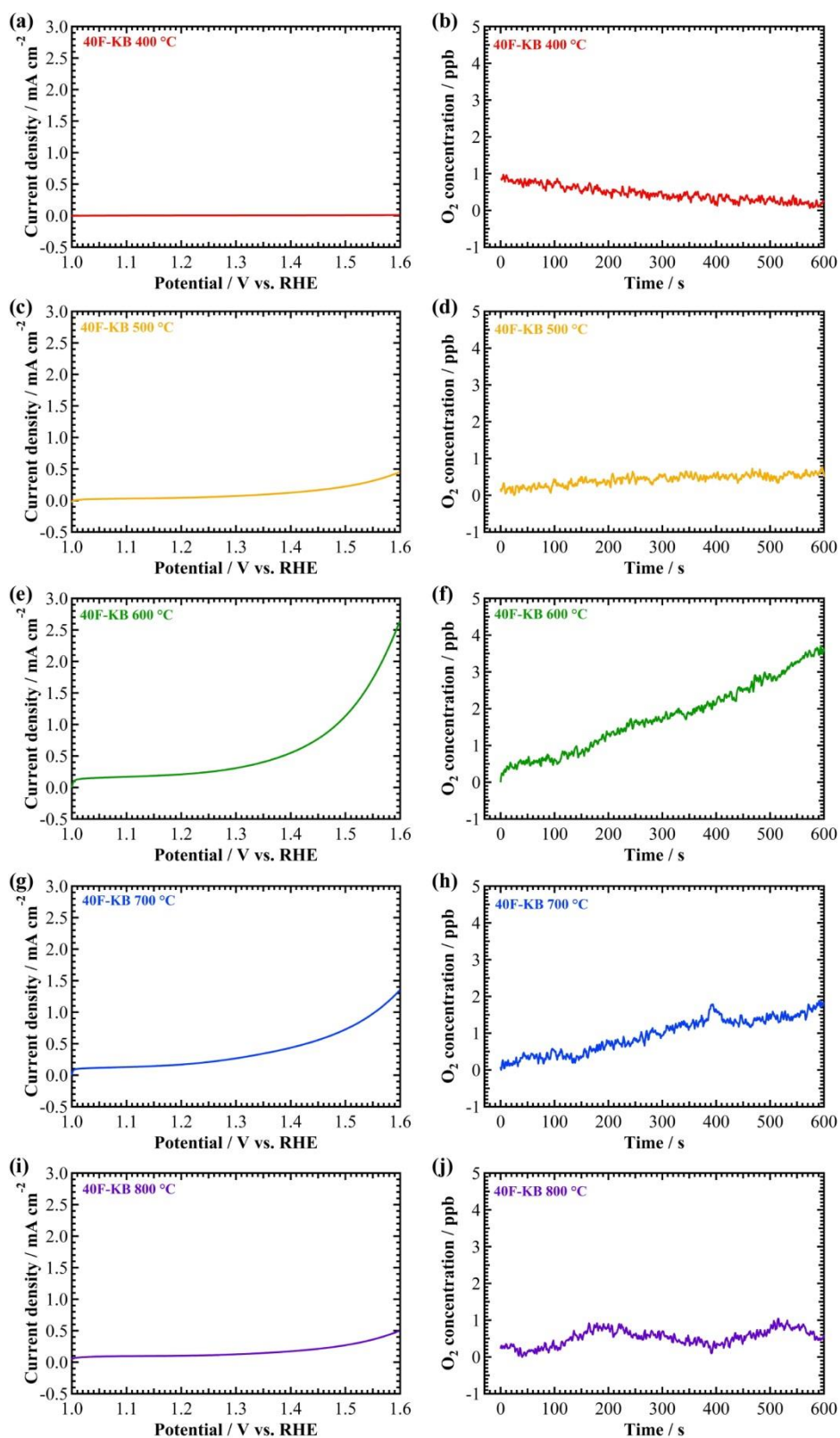


Fig 4.6 (a, c, e, g, i) Linear sweep voltammogram (scan rate: 10 mV s^{-1}) and (b, d, f, h, j) O_2 concentration versus time of 40F-KBs, RuO_2 , and KB on RDE (1600 rpm) in 0.1 M KOH after electrochemical pretreatment (1.6 V for 1 min).

The specific surface area (SSA) was measured to clarify the relationship between the OER activity and the SSA of the samples (Fig 4.7 (a)). The SSAs of samples are represented in Table 4.1. The SSA of KB, 40F-KB 800 °C, 40F-KB 600 °C, and 40F-KB 400 °C were 2177 m² g⁻¹, 1597 m² g⁻¹, 1488 m² g⁻¹, and 687 m² g⁻¹, respectively. It indicates that Nafion remained on the 40F-KB 400 °C, which resulted in filled pores. The N₂ adsorption-desorption isotherm of 40F-KB 600 °C and 40F-KB 800 °C were almost the same, which indicates complete decomposition of Nafion. However, 40F-KB 800 °C exhibited a much lower OER activity than 40F-KB 600 °C. Therefore, the catalytic activity was not related to SSA in 40F-KB. Raman spectroscopy was also used to investigate the details of the structure of 40F-KBs (Fig 4.7 (b)). KB and 40F-KBs exhibited the same Raman spectra. Thus, the disordered graphitic structure was maintained, even though fluorine was doped in KB.

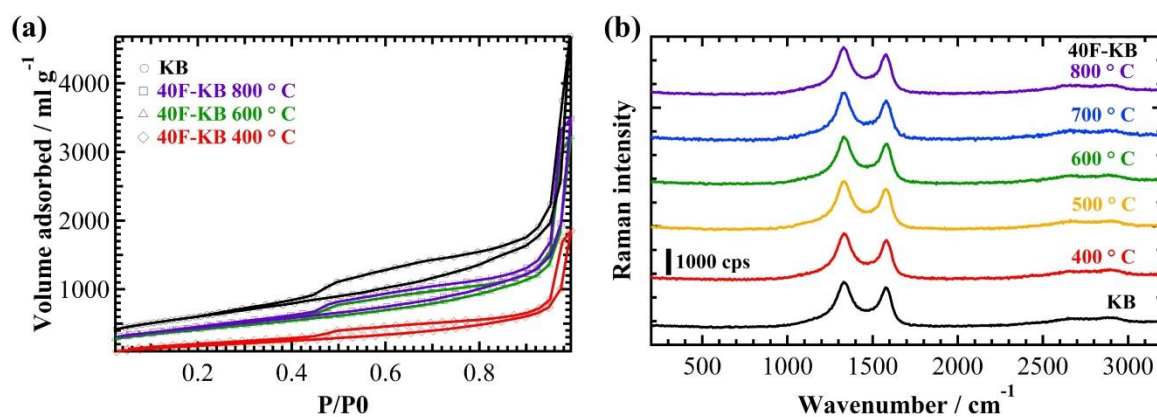


Fig 4.7 (a) N₂ adsorption-desorption isotherm of KB, 40F-KB 800°C, 40F-KB 600°C, and 40F-KB 400°C. (b) Raman spectra of 40F-KBs and KB. Laser excitation wavelength: 514 nm.

Table 4.1 Specific surface area of 40F-KBs and KB.

Sample	Specific surface area (m ² g ⁻¹)
KB	2177
40F-KB 800 °C	1597
40F-KB 600 °C	1488
40F-KB 400 °C	687

It should be emphasized that we performed chronoamperometry and *in-situ* O₂ concentration measurement for 40 min for the analysis of the durability as shown in Fig 4.8. As a result, current density gradually decreased to a few $\mu\text{A cm}^{-2}$ over 30 min (Fig. 4.8 (a)). Besides, O₂ concentration also saturated at about 7 ppb after 30 min. Thus, 40F-KB shows OER catalytic activity for 30 minutes.

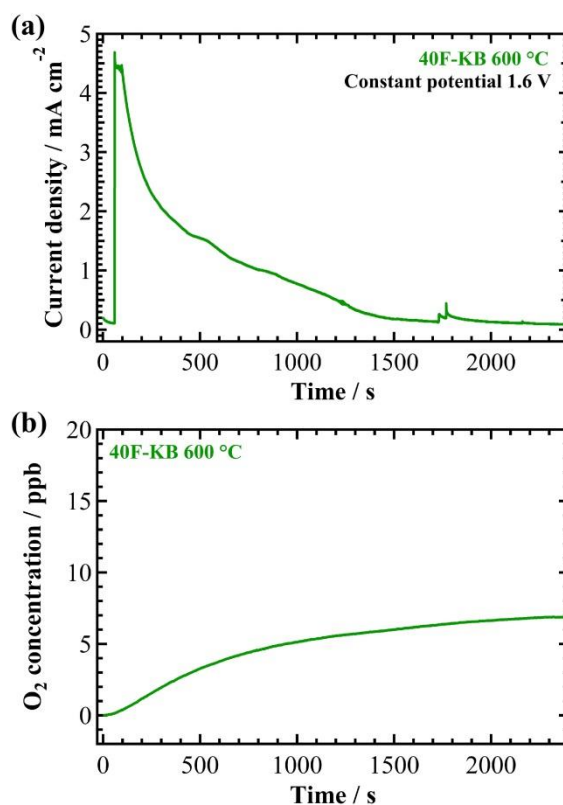


Fig 4.8 (a) Chronoamperometry and (b) O₂ concentration versus time curve for 40F-KB 600 °C. O₂ concentrations were recorded at 1.6 V constant potential after 40 min.

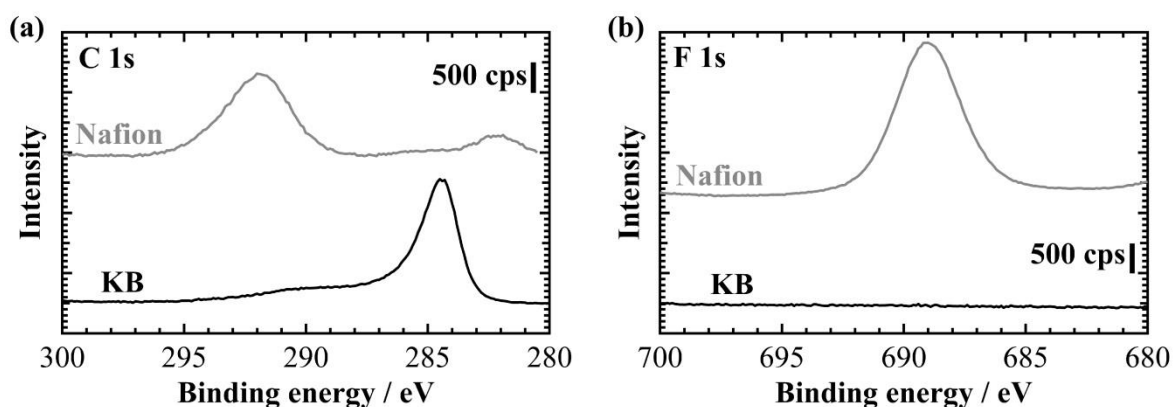


Fig 4.9 XPS spectra of the C 1s (a) and F 1s (b) ranges for Nafion and KB.

To demonstrate the correlation between the OER activity and C-F bonding, the 40F-KBs were investigated by XPS. The atomic ratios of carbon, fluorine and oxygen are shown in Table 4.2. No correlation between OER activity and oxygen ratio is found. The XPS near C1s and F1s regions are shown in Fig 4.9. In the case of Nafion, C1s and F1s appeared at 292.0 eV and 689.0 eV, respectively (Fig 4.9 (a) and (b)).

Table 4.2 Atomic ratios of 40F-KBs (c: covalent and s: semi-ionic)

Pyrolysis temperature	C (%)	F (%)	O (%)
400 °C	65.6	32.3 (c: 32.3, s: 0)	2.1
500 °C	90.0	6.2 (c: 3.3, s: 2.9)	3.8
600 °C	90.8	5.5 (c: 1.6, s: 3.9)	3.7
700 °C	92.4	4.9 (c: 1.4, s: 3.5)	2.9
800 °C	95.0	2.9 (c: 0.8, s: 2.1)	2.1

Atomic ratios of C, F and O were estimated from the areas of their 1s peaks and relative sensitivity factors (0.25: 1: 0.66). F 1s of semi-ionic C-F and covalent C-F have peaks at 687.0 eV and 689.0 eV of full width at half maximum (FWHM) of 2.1 eV and 6.2 eV, respectively. XPS results of KB and F-KBs are shown in Fig 4.10 (a) and (b). In comparison with Nafion, F1s peak was not observed from KB (Fig 4.10 (b)), whereas the F1s peak was observed from 40F-KBs (Fig. 4.10 (b)). Furthermore, 40F-KB 600 °C did not show S2p peak, which suggested the sulfonic acid group (-SO₃H) was completely removed by the pyrolysis at 600 °C (Fig. 4.11). For the 40F-KB 400 °C, peaks at 292.0 eV and 284.5 eV were present. The peak at 284.5 eV is well-known to be attributed to the sp² and sp³ carbon structures. This result suggests that 40F-KB 400 °C is mixture of Nafion and the KB, and 400 °C is too low for the decomposition of Nafion. With increased temperature, the fluorine peak was shifted towards the lower binding energy by approximately 2.0 eV, and the intensity of the carbon peak at 292.0 eV was decreased. Furthermore, the quantity of fluorine also decreased with the increase of the pyrolysis temperature, as shown in Table 4.2. In particular, the fluorine peak of 40 F-KB 600 °C can be deconvoluted into 689.0 eV and 687.0 eV, which are F atoms with covalent and semi-ionic C-F bonds, respectively.²² In addition, semi-ionic C-F bond increases up to 600 °C, and start to decrease above 600 °C. This result indicates that semi-ionic C-F bond can be increased with increasing the pyrolysis. The maximum semi-ionic to covalent bond ratio is approximately 5:2 above 600 °C. On the other hand, carbon fluoride also decomposes at high temperature, reducing the total amount of F. Thus, 600 °C is the optimized temperature considering both semi ionic ratio and total F content. This result means that the C-F bonding can easily be controlled by the pyrolysis temperature. The

changes from covalent C-F to semi-ionic C-F by raising the pyrolysis temperature of Nafion have not been reported previously.

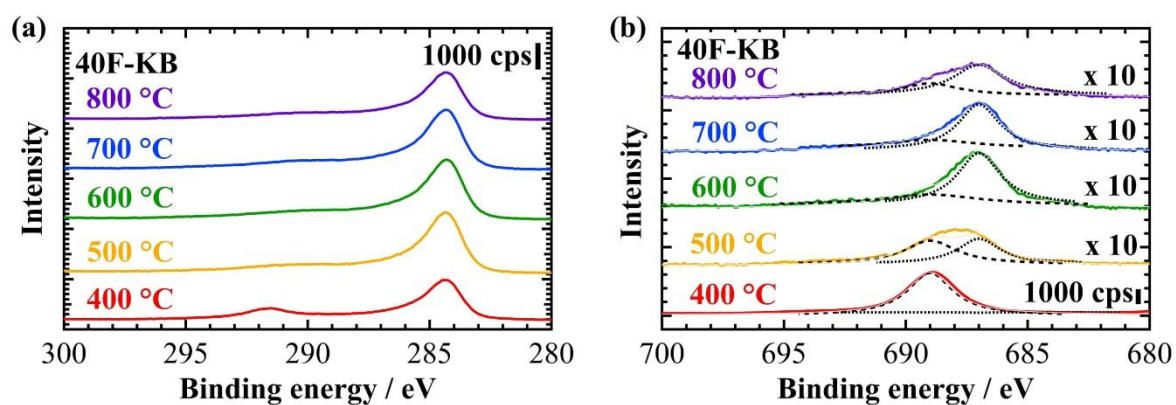


Fig 4.10 XPS spectra of the C 1s (a) and F 1s (b) ranges for 40F-KBs with pyrolysis temperature dependence.

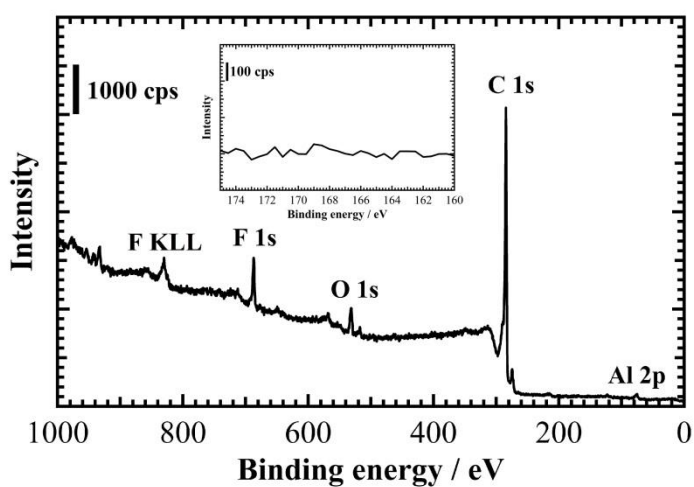


Fig 4.11 XPS wide scan spectra of 40F-KB and around the S2p ranges (inset)

As shown in Table 4.2, the maximum ratio of semi-ionic C-F bonding was found for the 40F-KB 600 °C. The O₂ production as a function of the atomic ratio of semi-ionic C-F bonding, as shown in Fig. 4.12. The O₂ concentration was recorded at 1.6 V after 10 min. As a result, the O₂ concentration increased with the increase of the atomic ratio of semi-ionic C-F. These results strongly indicate that OER occurs on the carbon atoms with semi-ionic C-F bonds. In particular, the OER activity is dramatically increased when the atomic ratio of semi-ionic C-F bond is above 3%. A probable reason is that neighboring carbon atoms both with semi-ionic C-F bonding have synergistic effect to further enhance OER activity.

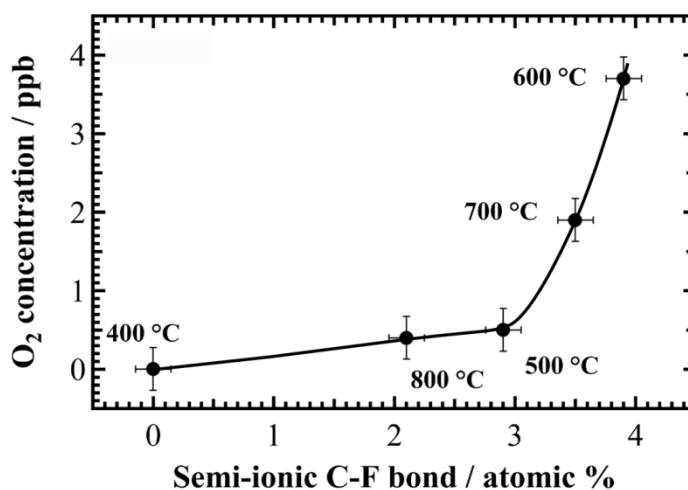


Fig 4.12 O₂ concentration versus atomic ratio (%) semi-ionic C-F bonds for 40F-KBs. O₂ concentrations were recorded at 1.6 V constant potential after 10 min.

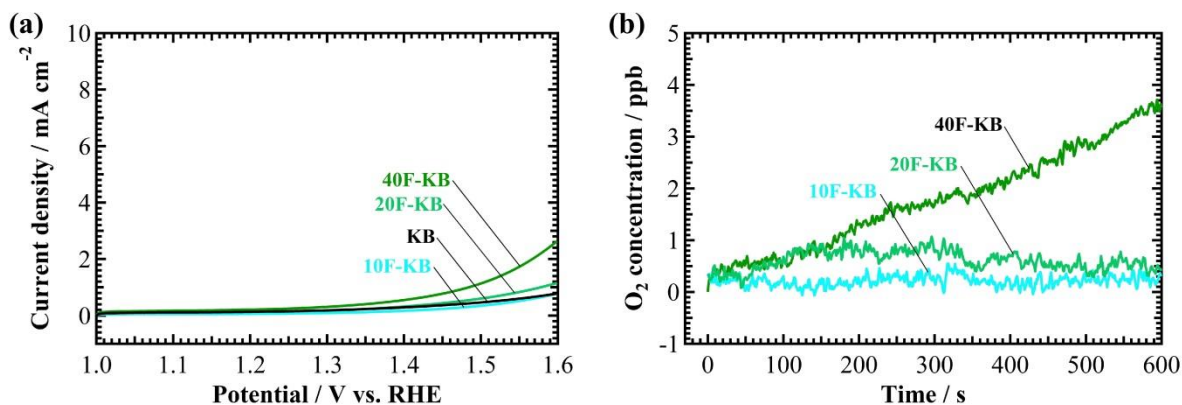


Fig 4.13 (a) Linear sweep voltammogram (scan rate: 10 mV s^{-1}) and (b) O_2 concentration versus time of 10F-KB, 20F-KB, 40F-KB and RuO_2 on RDE (1600 rpm) in 0.1 M KOH after electrochemical pretreatment (1.6 V for 1 min).

4.3.2 OER activity for fluorine-doped carbon depending on Nafion amount

Next, to evaluate dependence for Nafion usage on fluorine-doped carbon, Fig 4.13 shows linear sweep hydrodynamic voltammograms and O_2 concentration versus time curves of KB, 10F-KB, 20F-KB, and 40F-KB after electrochemical pretreatment. Pyrolysis temperature was set at $600 \text{ }^\circ\text{C}$. As a result, current density and O_2 concentration were increased with increasing the Nafion usage on KB. In case of the XPS, F-KBs had semi-ionic and covalent C-F bonding. Except for 10F-KB results, semi ionic to covalent bond ratio was 5 : 2. This result indicates that semi-ionic to covalent bond ratio is controlled by pyrolysis temperature.

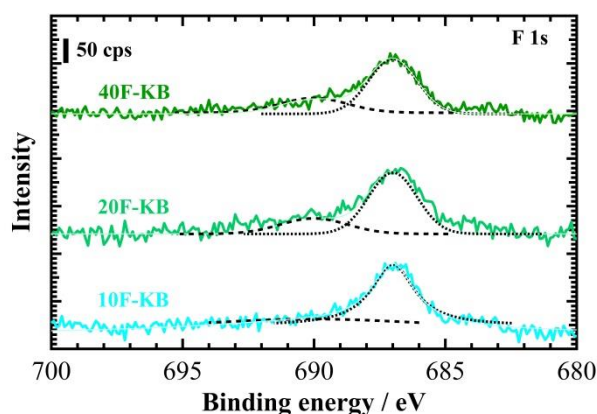


Fig 4.14 XPS spectra around F1s range for 10F-KB, 20F-KB, and 40F-KB.

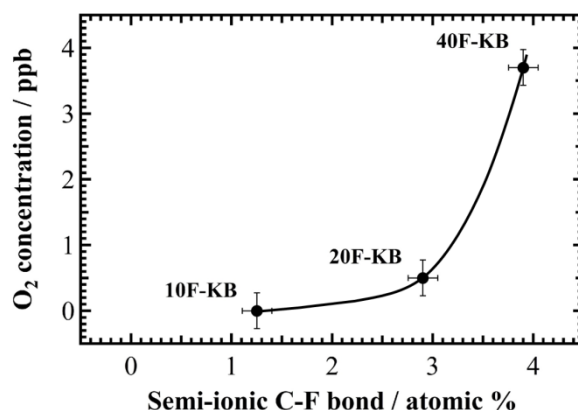


Fig 4.15 O₂ concentration versus atomic ratio (%) semi-ionic C-F bonds for 10F-KB, 20F-KB, and 40F-KB. Pyrolysis condition (600 °C). O₂ concentrations were recorded at 1.6 V constant potential after 10 min.

Fig 4.15 shows relationship for O₂ concentration with atomic ratio of semi-ionic C-F bonding. As a result, O₂ concentration was increased with increasing the semi-ionic C-F bonding. In addition, the OER activity of 20F-KB 600 °C was similar to 40F-KB 500 °C. Meanwhile, 20F-KB 600 °C and 40F-KB 500 °C possessed an equal quantity of semi-ionic C-F bonding but different amounts of covalent C-F bonding (Table 4.2 and Table 4.3). Based on this result, I proved that the covalent C-F bond is inactive for OER. Dresselhaus *et al.* reported that covalent C-F bonds appear on carbon with sp³ hybridization.¹⁰ Ito *et al.* suggested that covalent C-F bonds are formed on buckled carbon sheet, while semi-ionic bonds are formed on planar carbon sheet.²² Therefore, if a fluorine atom is bonded to a defect of the graphitic structure, a covalent C-F bond is formed. However, a semi-ionic C-F bond can be formed from the 2p_z orbital of a carbon atom which is perpendicular to the graphene plane. In general, the semi-ionic C-F bonds have higher polarity than the covalent C-F bonds.¹² Therefore, adsorption of OH⁻ in the first step of OER can be accelerated at the higher positively charged carbon with semi-ionic C-F bonds, leading to higher OER activity.

Table 4.3 Atomic ratio of fluorine doped carbon (c: covalent, and s: semi-ionic). Pyrolysis temperature at 600 °C

Sample	C (%)	F (%)	O (%)
10F-KB	91.3	1.3 (c: 0.05, s: 1.25)	2.1
20F-KB	90.0	4.1 (c: 1.2, s: 2.9)	5.4
40F-KB	90.8	5.5 (c: 1.6, s: 3.9)	3.7

4.3.3 pH-dependent OER activity for fluorine-doped carbon

pH dependence on OER activity was carried out to evaluate the reaction mechanism. In alkaline electrolyte, platinum or metal oxide shows a reversible binding of hydroxide ion coupled to one electron oxidation as a turnover-limiting electrochemical step to form a surface oxide species.^{23,24} The shift in mechanism between the pH region has been attributed to the kinetic facility of oxidizing hydroxide ion on active site.²⁵ Therefore, I investigated the OER activity for wide alkaline pH range from 11.5 to 14. For the electrochemical kinetic study, the Tafel slope is characteristic of an O₂ evolution mechanism. $d\log(i)/dpH$ cannot be experimentally estimated in potentiostatic system because overpotential is variable. Hence, Tafel slope is convoluted with the slope of the potential versus pH plot as followed;

$$\left(\frac{\partial E}{\partial pH}\right)_i = -\left(\frac{\partial E}{\partial \log(i)}\right)_{pH} \left(\frac{\partial \log(i)}{\partial pH}\right)_E \quad (1)$$

This formula estimates the dependence of $\log(i)$ on pH which is dependence of the electrocatalytic rate on proton order. Fig 4.16 (a) shows LSV curves for pH dependence on 40F-KB600. As a result, onset potential was shifted toward negative with increasing pH. On the basis of the result, potential versus pH curves are plotted at constant current density of 0.7 mA cm⁻² (Fig 4.16 (b)) and 0.25 mA cm⁻² (Fig 4.16 (c)). As a result, slopes for 0.7 mA and 0.25 were -0.135 V pH⁻¹ and -0.156 V pH⁻¹, respectively, and which correspond with left-hand side of formula (1).

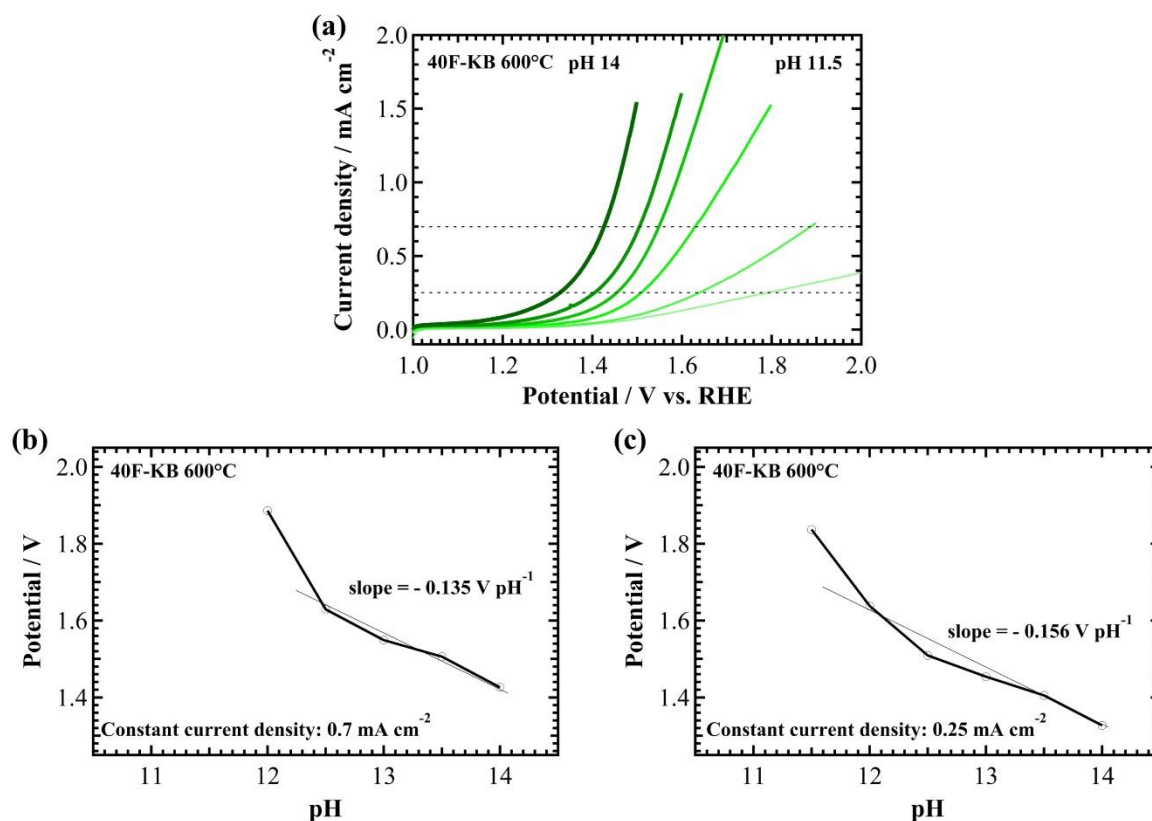


Fig 4.16 (a) Linear sweep voltammogram of 40F-KB 600 °C for pH dependence (pH 11.5, 12, 12.5, 13, 13.5, and 14). Potential versus pH curves for 40F-KB 600 °C at constant current density of (b) 0.7 mA cm⁻² and (c) 0.25 mA cm⁻².

Fig 4.17 shows Tafel slopes around 0.7 mA cm⁻² and 0.25 mA cm⁻² at constant pH 13. As a result, Tafel slopes around 0.7 mA cm⁻² and 0.25 mA cm⁻² were 231 mV decade⁻¹ and 210 mV decade⁻¹, respectively, and relatively higher than Tafel slope of IrO₂ nanoparticle.⁴ This result is expected that current density is partly attributed by carbon oxidation and decomposition, resulting in high Tafel slope for 40F-KB 600 °C. Using the formula (1), results of log(i) on pH for 0.7 mA cm⁻² and 0.25 mA cm⁻² were 0.58 and 0.74. In particular, these parameters were lower than first reaction order on proton activity. This result is expected for pre-equilibrium hydroxide ion adsorption on active site around semi-ionic C-F bond, and then active site is gradually decreased. Therefore, proton activity has almost half reaction order.

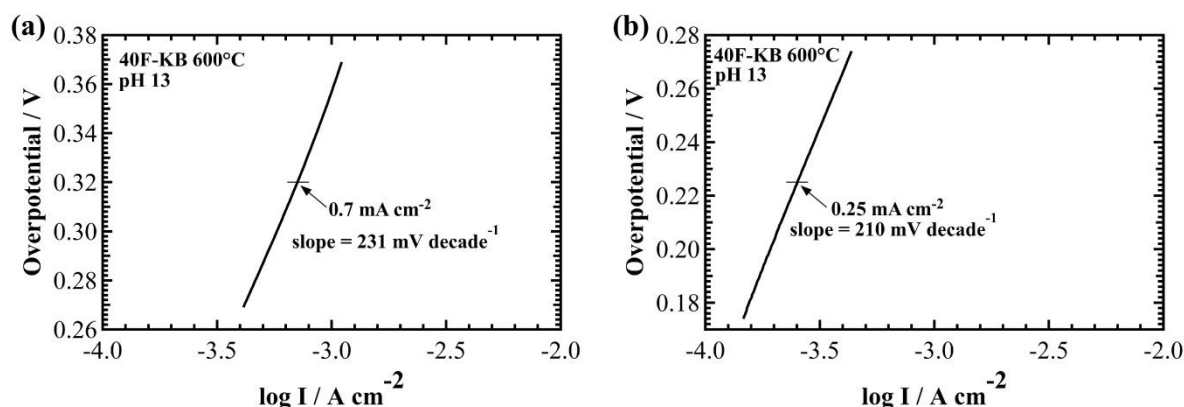


Fig 4.17 Tafel plots of 40F-KB 600 °C at pH 13. Center of plot range is current density of (a) 0.7 mA cm⁻² and (b) 0.25 mA cm⁻².

To compare the pristine KB, LSV curves for pH dependence and potential versus pH curves is shown in Fig 4.18. LSV curves on KB has also same tendency to result of 40F-KB as shown in Fig 4.16 (a). Besides, slopes of potential versus pH curves were -0.161 V pH^{-1} and -0.133 V pH^{-1} at constant current density of 0.7 mA cm⁻² and 0.25 mA cm⁻², respectively. In comparison with 40F-KB 600 °C, 40F-KB 600 °C was almost same result. Besides, Tafel slopes at pH 13 were 244 mV and 225 mV around current density of 0.7 mA cm⁻² and 0.25 mA cm⁻² as shown in Fig 4.19. Using these parameters and formula (1), log (i) on pH is estimated as 0.66 and 0.59 for 0.7 mA cm⁻² and 0.25 mA cm⁻², respectively. In case of the 40F-KB 600 °C, reaction order on proton activity for 0.25 mA cm⁻² was higher than result of 0.7 mA cm⁻². On the other hand, reaction KB for 0.25 mA cm⁻² had lower order on proton activity than 0.7 mA cm⁻². This result indicates that 40F-KB 600 °C has lower overpotential than KB, resulting in relatively high reaction order at 0.25 mA cm⁻². In addition, KB was also half reaction order on proton activity. This result is expected that proton activity is not affected by fluorine doping, but OER activity is changed by positively charged carbon of semi-ionic C-F bond.

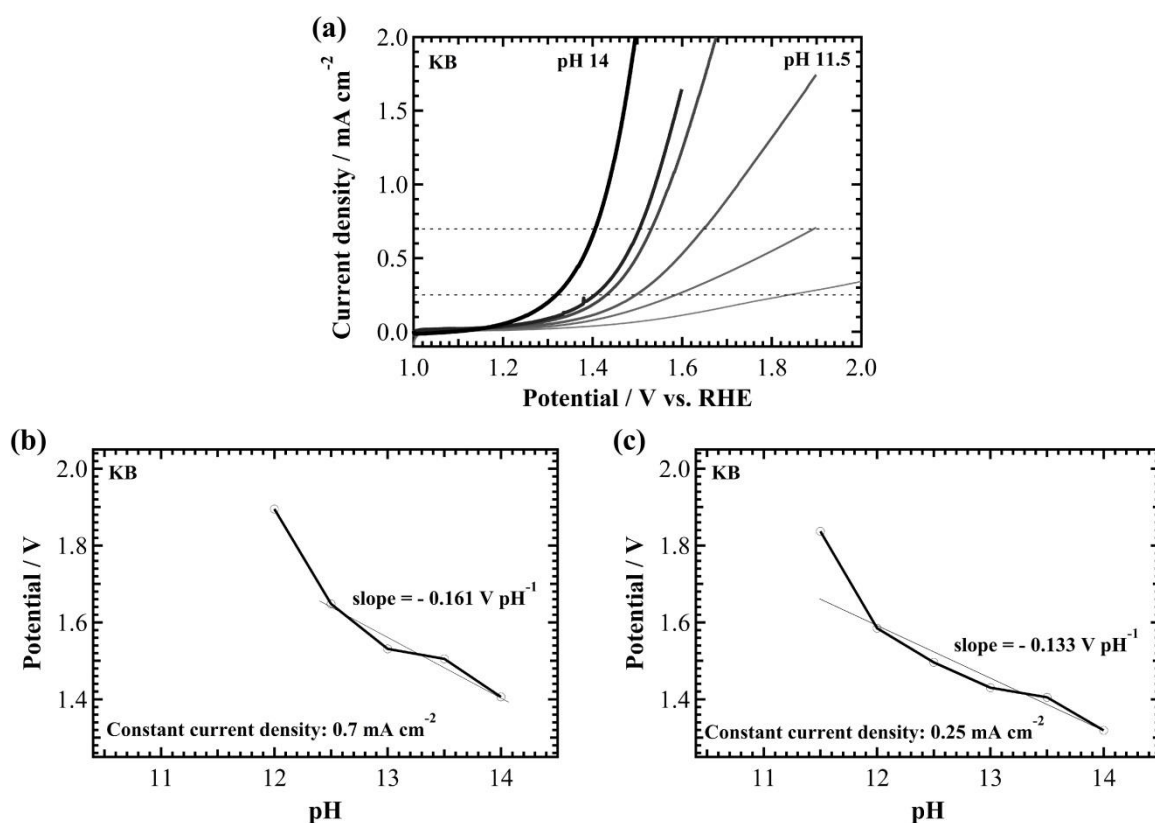


Fig 4.18 (a) Linear sweep voltammogram of KB for pH dependence (pH 11.5, 12, 12.5, 13, 13.5, and 14). Potential versus pH curves for KB at constant current density of (b) 0.7 mA cm⁻² and (c) 0.25 mA cm⁻².

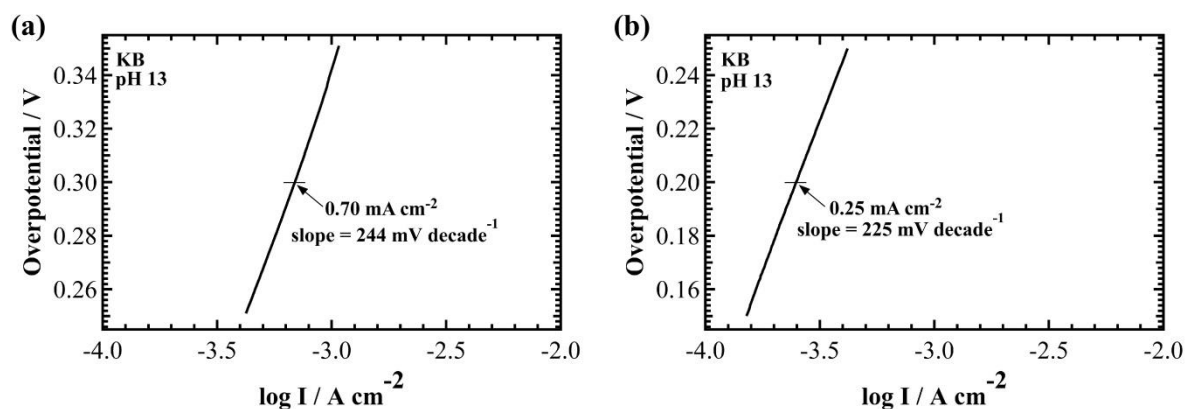


Fig 4.19 Tafel plots of KB at pH 13. Center of plot range is current density of (a) 0.7 mA cm⁻² and (b) 0.25 mA cm⁻².

4.3.4 Kinetic OER activity for fluorine-doped carbon

To evaluate the kinetic OER, potential and pH dependence were adopted for increment of O_2 concentration and current density. I first confirmed the relation between evolved O_2 concentration (C_{O_2}) and total current density (j_{total}) by using RuO_2 as model catalyst. Disk electrodes were rotated at 1600 rpm, and potentiostatic polarization was conducted in 0.1 M KOH aqueous solution (pH = 13) to induce OER. As a result, increase of electrochemical potential leads to the increase in both j_{total} and O_2 concentration C_{O_2} as shown in Fig 4.20. Importantly, slope of O_2 concentration for time, i.e. velocity for OER ($v_{OER} = dC_{O_2}/dt$), was increased with increment of j_{total} . This result suggests that there is positive correlation between v_{OER} and j_{total} using RDE with O_2 sensor method.

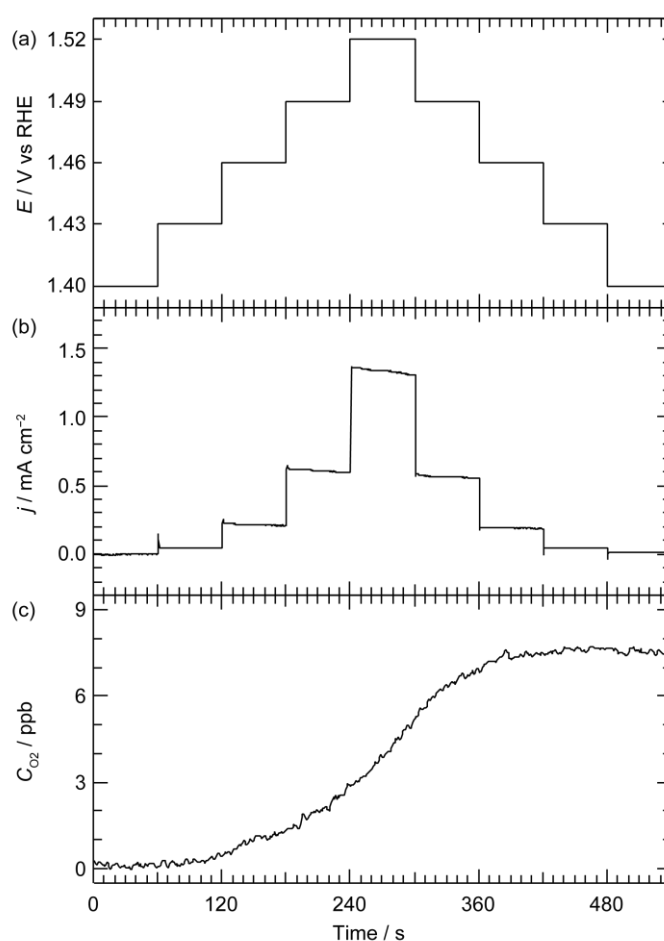


Fig 4.20 OER from RuO_2 in 0.1 M KOH solution (pH = 13). (a) Applied potential (E), (b) current density (j), and (c) O_2 concentration (C_{O_2}) were plotted versus time.

Fig 4.21 shows plot of time versus applied potential, j_{total} and C_{O_2} recorded for 40F-KB 600 °C in 0.1 M KOH aqueous solution (pH = 13). As discussed in RuO₂ experiment, C_{O_2} increased as the electrochemical potential, E , increased. On the other hand, forward trace and backward trace for j_{total} and v_{OER} was distinct. For example, v_{O_2} at 1.59 V in forward trace (0.011 ppb s⁻¹, 180 s – 240 s) was twice higher than backward trace (0.0047 ppb s⁻¹, 360 s - 420 s). In addition to that, j_{total} is not stable during the potentiostatic polarization. On the other hand, v_{OER} shows linearity under potentiostatic polarization. This observation of j_{total} and v_{OER} suggests that j_{total} is contributed from OER as well as catalyst oxidation after the initiation of OER.

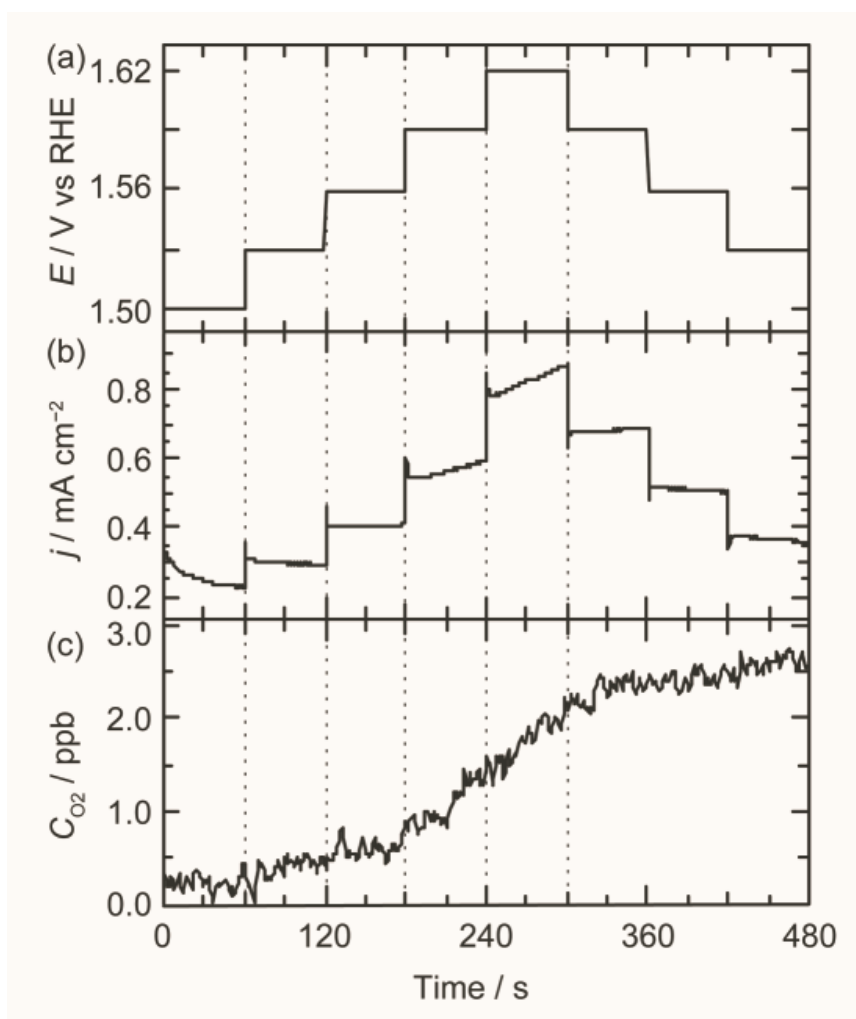


Fig 4.21 OER from 40F-KB 600 °C in 0.1 M KOH solution (pH = 13). (a) Applied potential (E), (b) current density (j_{total}) and (c) O₂ concentration (C_{O_2}) were plotted versus time.

I investigated effect of proton concentration on the observed current density. Fig 4.22 shows the Tafel plot of OER from 40F-KB 600 °C by plotting j_{total} and E versus NHE scale. We averaged j_{total} in each duration for potentiostatic polarization because of instability of observed current density during chronoamperometry as shown in Fig 4.23. Importantly, j_{total} showed different behaviour depending on pH of KOH aqueous solution (pH = 12, 13, 14). In case of pH 12, the current density was almost similar values around $30 \mu\text{A cm}^{-2}$ regardless to the applied potential. In addition, increase in pH leads to the increase in j_{total} . On the other hand, in the case of pH 13.5 and 14, j_{total} were almost same order. The Tafel slopes, $\partial E/\partial \log(j_{\text{total}})$, were variant depending on pH of solution as shown in Fig 4.22. Tafel slopes at pH 13, pH 13.5, and pH 14 were 227 mV dec^{-1} , 225 mV dec^{-1} , and 183 mV dec^{-1} , respectively. These Tafel slopes were even higher than 118 mV dec^{-1} , which corresponds to the single-electron transfer rate-limiting step.²⁶ The observed high Tafel slopes are due to the rate-limiting chemical step or diffusion steps, which are not due to the electrochemical process.

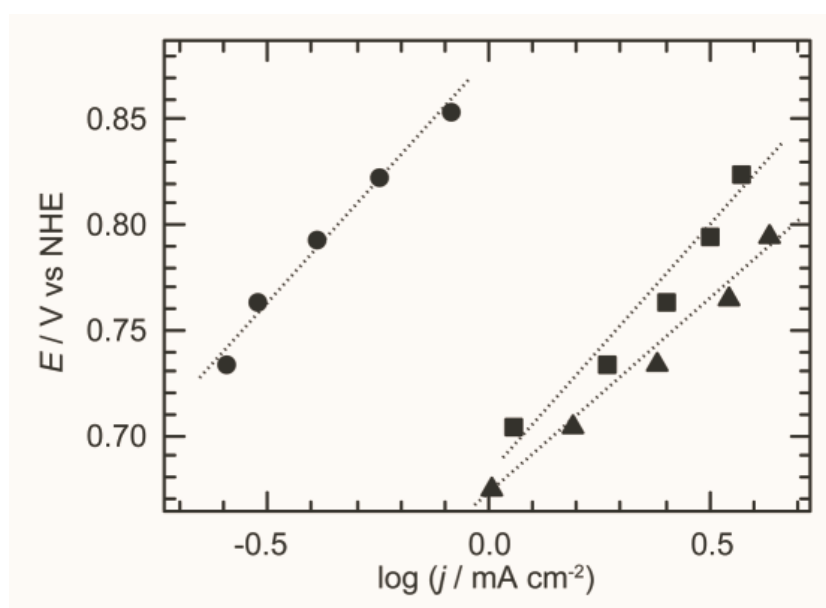


Fig 4.22 Tafel plot of total current density versus electrochemical potential under oxygen evolution condition from 40F-KB 600 °C. The data were recorded in pH 13 (circle) pH 13.5 (square) and (c) pH 14 (triangle). Current density was averaged throughout at each potential duration.

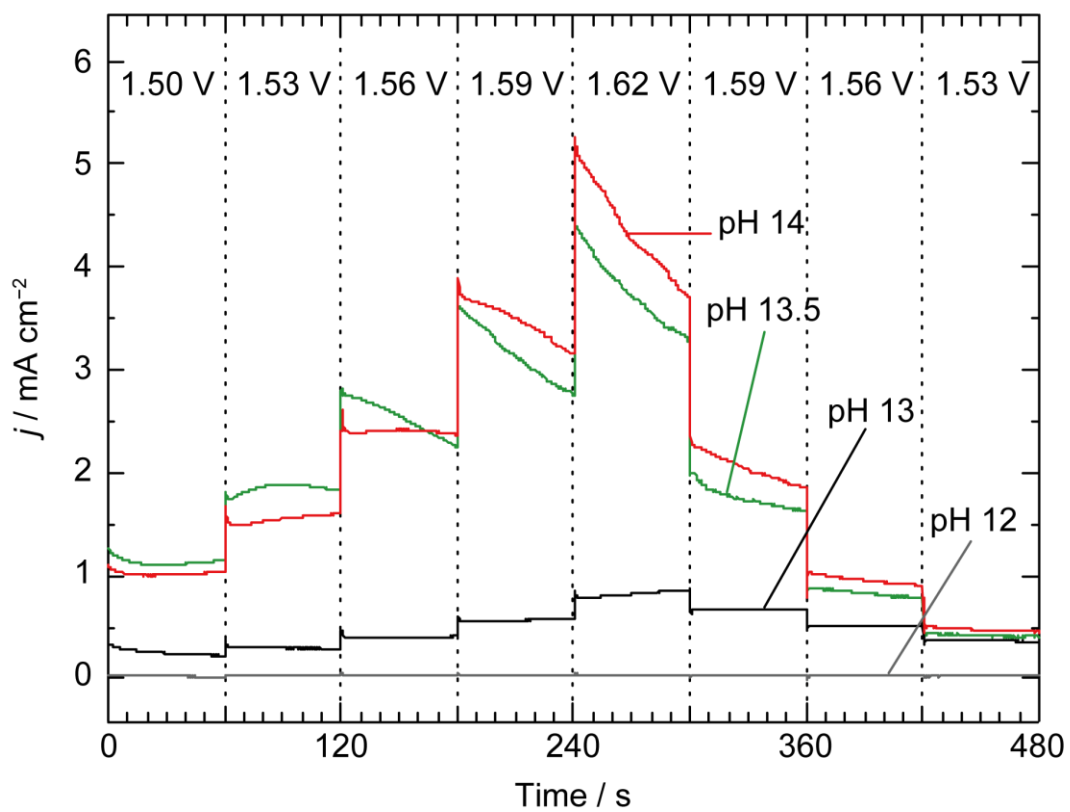


Fig 4.23 Chronoamperometry for 40F-KB 600 °C at different electrochemical potentials. Applied electrochemical potentials were shown in above.

To evaluate pH dependence of ν_{OER} , I investigated the ν_{OER} from the measurement of C_{O_2} under potentiostatic polarization. In case of pH 12, C_{O_2} was almost same regardless to applied potential as shown in Fig 4.24. However, ν_{OER} at pH 13.5 and pH 14 were significantly increased than results of pH 12 and pH 13. In addition, ν_{OER} at the potential of 1.62 V corresponds maximum value 0.038 ppb s^{-1} in KOH solution (pH = 14). Therefore, OER activity of 40F-KB 600 °C is enhanced by increasing the pH and E. Besides, oxygen evolution rate was slightly decreased with backward trace from 1.62 V to 1.53 V in comparison with forward trace from 1.53 V to 1.62 V at pH 13. Fig 4.25 shows Tafel plots of OER from 40F-KB 600 °C by plotting ν_{OER} and E versus NHE scale. Tafel slope can be treated as same even for ν_{OER} instead of j_{OER} (vide infra). Tafel slopes were similar regardless to pH of KOH aqueous solutions. Tafel slopes at pH 13, pH 13.5, and pH 14 were 62 mV dec^{-1} , 62 mV dec^{-1} , and 66 mV dec^{-1} , respectively. In addition to that potential shift at the same ν_{OER} are quite similar to each other, and $\partial E/\partial \log(a_{\text{H}^+})$ is 63 mV pH unit^{-1} . This observation suggests that ν_{OER} is related to the activity of proton.

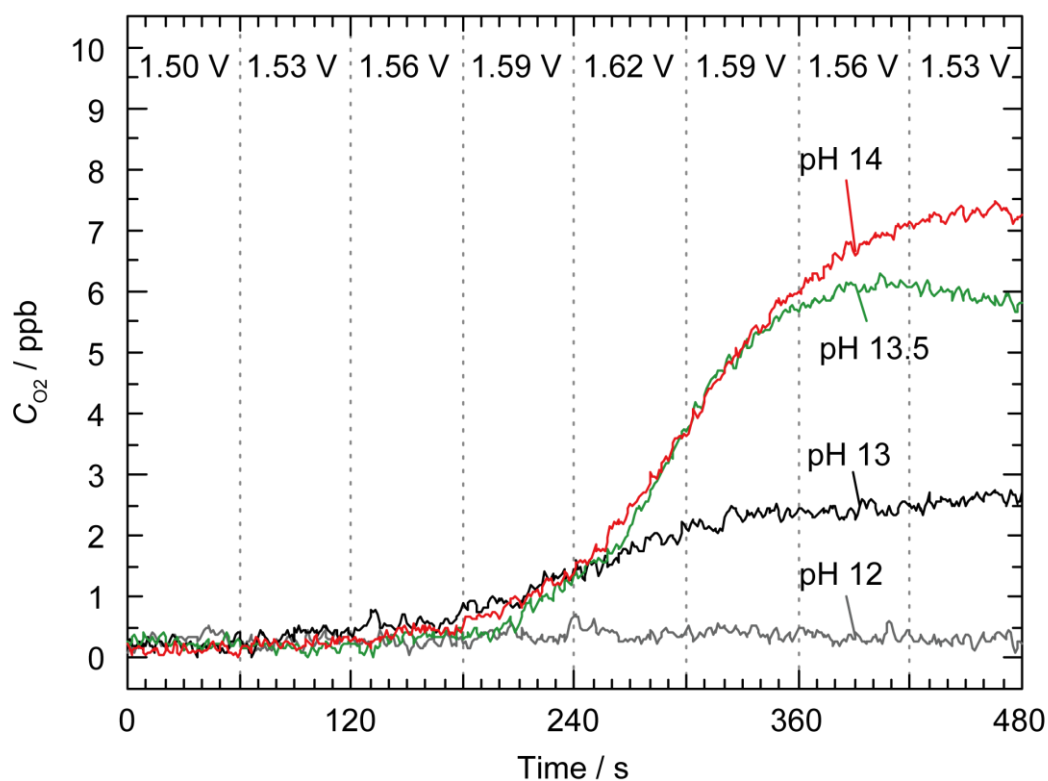


Fig 4.24 Time-course analysis of O_2 concentration trace under the potentiostatic polarization. Applied electrochemical potentials were shown in above.

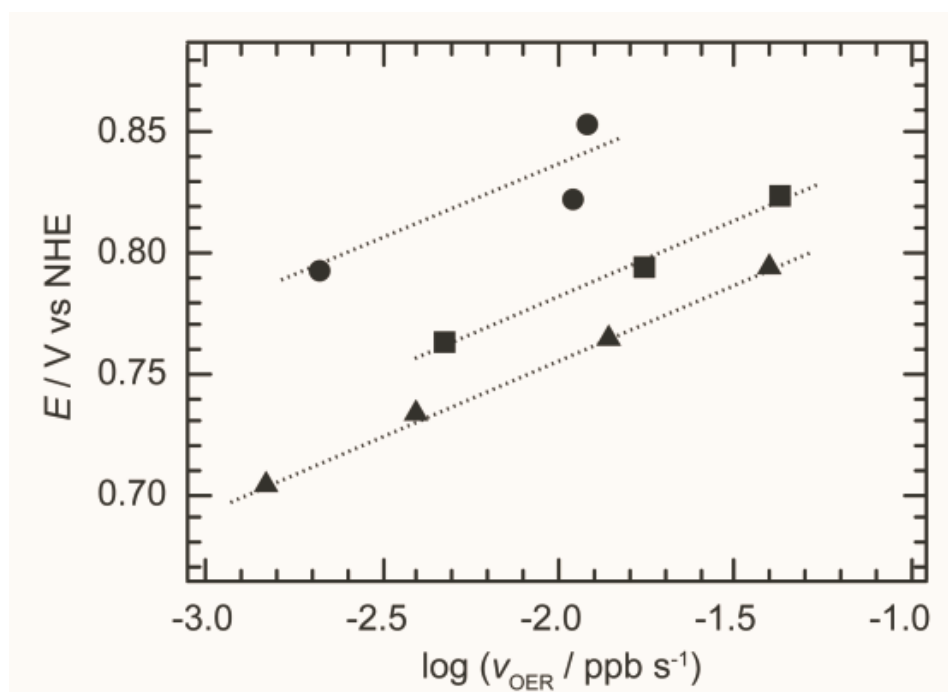


Fig 4.25 Tafel plot of reaction velocity of OER (v_{OER}) versus electrochemical potential (E) under oxygen evolution condition from 40F-KB 600 °C. The data were recorded in pH 13 (circle) pH 13.5 (square) and (c) pH 14 (triangle). v_{OER} were evaluated from the slope of the concentration of oxygen versus time; dC_{O_2}/dt .

Conventionally, kinetic model is constructed from rate-limiting kinetics in the net reaction of catalytic cycle. OER current (j_{OER}) is described by velocity of reaction (v_{OER}) and Faraday's constant (F), and number of electron (n). j_{OER} is followed as expression;

$$j_{\text{OER}} = nFv_{\text{OER}} \quad (2)$$

Therefore, v_{OER} can be used as an parameter for Tafel analysis, and Tafel slope discussed herein is expressed as $\partial E/\partial \log(v_{\text{OER}})$. pH difference induces the shift of the thermodynamic potential between water and oxygen equilibrium redox couple. Therefore, the order of the proton is estimated from the following equation 3, which is based on the Euler's chain rule.^{25,27,28}

$$\frac{\partial \log(v_{\text{OER}})}{\partial \log(a_{\text{H}^+})} = - \frac{\partial E}{\partial \log(a_{\text{H}^+})} / \frac{\partial E}{\partial \log(v_{\text{OER}})} \quad (3)$$

Here, $\partial E/\partial \log(v_{\text{OER}})$ is conventional Tafel slope and $\partial E/\partial \log(a_{\text{H}^+})$ is explained as potential shift depending on pH at the same v_{OER} . As shown in Fig 4.25, Tafel slope for all the plot corresponds to almost 59 mV dec⁻¹ value regardless to pH that corresponds to $2.3 \times RT/F$. In addition to that, the potential shift to the pH at same reaction rate, $\partial E/\partial \text{pH}$, is 60 mV pH unit⁻¹. By using equation 3, v_{OER} is revealed to be proportional to inverse first order dependence of proton activity.

The reaction order for v_{OER} is described as following expression by using constant v_0 .

$$v_{\text{OER}} = v_0(a_{\text{H}^+})^{-1} \exp\left(\frac{FE}{RT}\right) \quad (4)$$

The rate expression carries the observed inverse first order dependence on proton activity, and the exponential relationship with electrochemical potential, E . Rearrangement of the log form of equation 4 yields a Tafel slope, $\partial E/\partial \log(v_{\text{OER}})$, of 59 mV decade that is also consistent with experimental data. Equation is consisted with a mechanistic sequence

involving a reversible one electron, one proton equilibrium step followed by rate-determining chemical step. These mechanisms are expressed as following equation 5 and 6;

$$\frac{\theta}{1-\theta} = K(a_{H^+})^{-1} \exp\left(\frac{FE}{RT}\right) \quad (5)$$

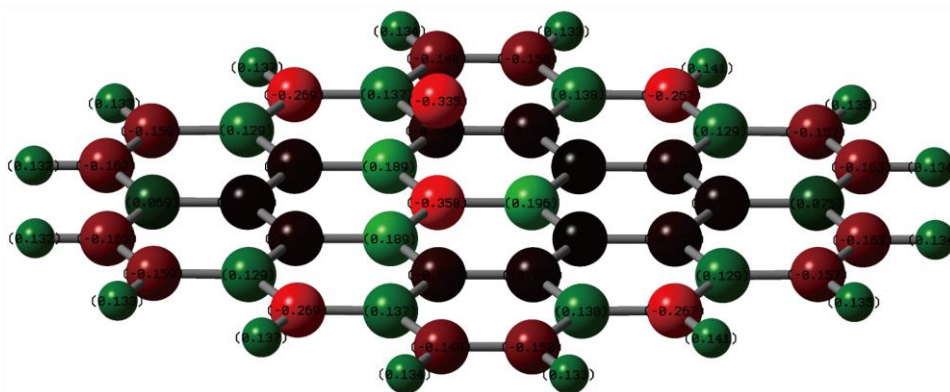
$$v_{OER} = k_2\theta \quad (6)$$

θ is the coverage of the adsorption step involving the proton-coupled electron transfer process. Due to the pre-equilibrium, θ is expected as small value. Therefore, $\theta/(1-\theta) \cong \theta$. Importantly, intrinsic exchange reaction rate is determined by pre-factor, k_2K . This is suggestive that interaction between hydroxide and water or adsorption enthalpy for the hydroxide is important.

In order to investigate the structural origin of 40F-KB 600 °C, I conducted the theoretical calculation for the model molecular structure of 40F-KB 600 °C. 40F-KB 600 °C has 90.8% of carbon element and 3.9% of fluorine from semi-ionic C-F bonding. That corresponds to one C-F bond site per 50 Å². I constructed aromatic system based on model structure (C₄₂H₁₆F) for the structure evaluation as shown in Fig 4.26. Importantly, I found that fluorine-doping on the graphene-like sheet induces the positive charge for neighboring α -carbon atom revealed by Mulliken charge analysis. In case of semi-ionic C-F bonding structure, α -carbon is positively charged with the values of 0.196 and 0.189. On the other hand, in case of covalent C-F bonding structure, α -carbon is less positively charged such as 0.124 and 0.112. This result suggests that fluorine doping induces charge localization at α -carbon atom, which can be an active site for turn-over rate-determining step as shown in Fig 4.27. This result would be expected that fluorine-doping induces (1) the increase of hydroxide adsorption energy or (2) increase of electrophilicity of adsorbed hydroxide species.

Interestingly observed phenomena in fluorine doped carbon are reminiscent with the highly active catalyst such as perovskites and surface platinum oxides.^{25,29,30}

(a) Semi-ionic C-F bond



(b) Covalent C-F bond

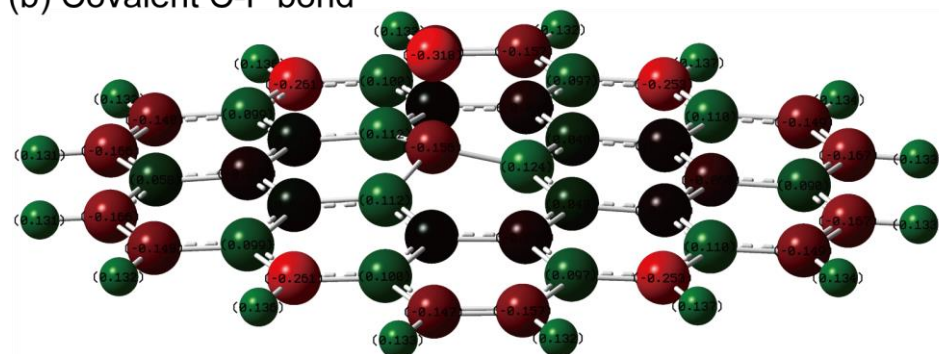


Fig 4.26 Mulliken charge analysis for semi-ionic C-F model structure and covalent C-F model structure. Green color and red color indicates the positive and negative charges respectively.

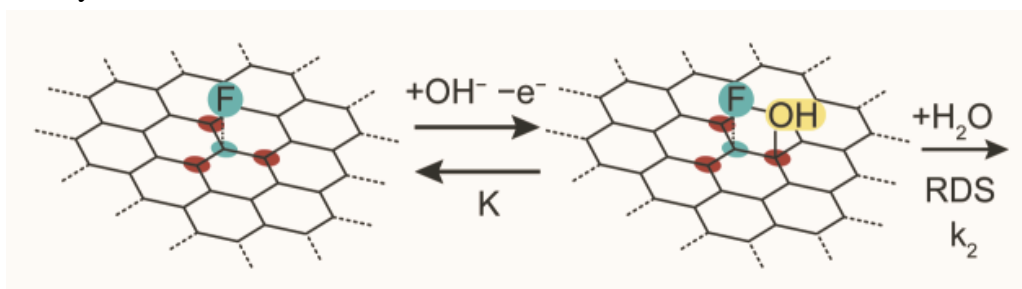


Fig 4.27 Schematic illustration of reaction mechanism of F-carbon. Pre-equilibrium of the hydroxide adsorption and one-electron oxidation occurred at positive charge carbon site (red) with respect to the fluorine-doped carbon sites (blue). The adsorbed hydroxide reacts with H₂O for the irreversible rate-determining chemical step.

4.4 Conclusion

Fluorine-doped carbon was successfully synthesized by pyrolysis of KB with Nafion. Electrochemical characterization and detection of the O₂ production were performed on the resulting fluorine-doped carbon. The OER activity was found to be enhanced by fluorine doping. Furthermore, the nature and quantity of C-F bonds can be controlled by the pyrolysis temperature. It is found that the increase of OER activity depends on the quantity of semi-ionic C-F bonds. The fluorine-doped carbon pyrolyzed at 600 °C had the most semi-ionic C-F bonding (3.9%), which showed the best OER performance. In case of the Nafion usage dependence, OER activity was enhanced by semi-ionic C-F bonds regardless of quantity of covalent C-F bond. On the basis of result from pH dependence, reaction order on proton activity was 0.5 ~ 0.8, in which was lower than first reaction order because hydroxide ion adsorbs on active site, and then active site gradually decreased. Proton activity was not affected by fluorine doping from results of pH dependence. These results suggest that OER occurs on carbon atoms with semi-ionic C-F bonding because of their very high positive charge. In addition, I discovered that non-linear relation between OER activity and the atomic ratio of semi-ionic C-F. This result implies that there may be synergistic effect between neighboring semi-ionic C-F bonding. In particular, I showed that fluorine doped carbon possesses high catalytic activity from the kinetic data profile. In most of the cases, carbon catalysts suffer from the decomposition, and mechanistic study are quite difficult in terms of the catalyst design. To solve this problem, I evaluate the comparison between evolved O₂ and current density by potential and pH dependence. As a result, Tafel data and pH dependence proved that OER catalysis proceeds with proton coupled electron transfer process and irreversible chemical step. The presented study shed lights on the potential

catalysts for designer interfaces.

4.5 Reference

- (1) Zheng, Y.; Jiao, Y.; Li, L. H.; Xing, T.; Chen, Y.; Jaroniec, M.; Qiao, S. Z. Toward Design of Synergistically Active Carbon-Based Catalysts for Electrocatalytic Hydrogen Evolution. *ACS Nano* **2014**, 8 (5), 5290–5296.
- (2) Fortunelli, A.; Goddard III, W. a.; Sementa, L.; Barcaro, G. Optimizing the Oxygen Evolution Reaction for Electrochemical Water Oxidation by Tuning Solvent Properties. *Nanoscale* **2015**, 7 (10), 4514–4521.
- (3) Suen, N.-T.; Hung, S.-F.; Quan, Q.; Zhang, N.; Xu, Y.-J.; Chen, H. M. Electrocatalysis for the Oxygen Evolution Reaction: Recent Development and Future Perspectives. *Chem. Soc. Rev.* **2017**, 46 (2), 337–365.
- (4) Reier, T.; Oezaslan, M.; Strasser, P. Electrocatalytic Oxygen Evolution Reaction (OER) on Ru, Ir, and Pt Catalysts: A Comparative Study of Nanoparticles and Bulk Materials. *ACS Catal.* **2012**, 2 (8), 1765–1772.
- (5) Cherevko, S.; Geiger, S.; Kasian, O.; Kulyk, N.; Grote, J. P.; Savan, A.; Shrestha, B. R.; Merzlikin, S.; Breitbach, B.; Ludwig, A.; et al. Oxygen and Hydrogen Evolution Reactions on Ru, RuO₂, Ir, and IrO₂ Thin Film Electrodes in Acidic and Alkaline Electrolytes: A Comparative Study on Activity and Stability. *Catal. Today* **2016**, 262, 170–180.
- (6) Zhao, Y.; Nakamura, R.; Kamiya, K.; Nakanishi, S.; Hashimoto, K. Nitrogen-Doped Carbon Nanomaterials as Non-Metal Electrocatalysts for Water Oxidation. *Nat. Commun.* **2013**, 4, 1–7.
- (7) Zhao, Z.; Xia, Z. Design Principles for Dual-Element-Doped Carbon Nanomaterials as

- Efficient Bifunctional Catalysts for Oxygen Reduction and Evolution Reactions. *ACS Catal.* **2016**, *6* (3), 1553–1558.
- (8) Zhao, Z.; Li, M.; Zhang, L.; Dai, L.; Xia, Z. Design Principles for Heteroatom-Doped Carbon Nanomaterials as Highly Efficient Catalysts for Fuel Cells and Metal-Air Batteries. *Adv. Mater.* **2015**, *27* (43), 6834–6840.
- (9) O’Hagan, D. Understanding Organofluorine Chemistry. An Introduction to the C–F Bond. *Chem. Soc. Rev.* **2008**, *37* (2), 308–319.
- (10) Divittorio, S. L.; Dresselhaus, M. S.; Dresselhaus, G. A Model for Disorder in Fluorine-Intercalated Graphite. *J. Mater. Res.* **1993**, *8* (7), 1578–1585.
- (11) Nakajima, T.; Koh, M.; Gupta, V.; Žemva, B.; Lutar, K. Electrochemical Behavior of Graphite Highly Fluorinated by High Oxidation State Complex Fluorides and Elemental Fluorine. *Electrochim. Acta* **2000**, *45* (10), 1655–1661.
- (12) Lee, Y. S. Syntheses and Properties of Fluorinated Carbon Materials. *J. Fluor. Chem.* **2007**, *128* (4), 392–403.
- (13) Palchan, I.; Crespin, M.; Estrade-Szwarckopf, H.; Rousseau, B. Graphite Fluorides: An XPS Study of a New Type of CF Bonding. *Chem. Phys. Lett.* **1989**, *157* (4), 321–327.
- (14) Panomsuwan, G.; Saito, N.; Ishizaki, T. Simple One-Step Synthesis of Fluorine-Doped Carbon Nanoparticles as Potential Alternative Metal-Free Electrocatalysts for Oxygen Reduction Reaction. *J. Mater. Chem. A* **2015**, *3* (18), 9972–9981.
- (15) Sun, X.; Zhang, Y.; Song, P.; Pan, J.; Zhuang, L.; Xu, W.; Xing, W. Fluorine-Doped Carbon Blacks: Highly Efficient Metal-Free Electrocatalysts for Oxygen Reduction Reaction. *ACS Catal.* **2013**, *3* (8), 1726–1729.

- (16) Tressaud, A.; Moguet, F.; Flandrois, S.; Chambon, M.; Guimon, C.; Nanse, G.; Papirer, E.; Gupta, V.; Bahl, O. P. On the Nature of C-F Bonds in Various Fluorinated Carbon Materials: XPS and TEM Investigations. *J. Phys. Chem. Solids* **1996**, *57* (6–8), 745–751.
- (17) Birss, V. I. Oxygen Evolution at Platinum Electrodes in Alkaline Solutions. *J. Electrochem. Soc.* **1987**, *134* (1), 113.
- (18) Holst, G.; Glud, R. N.; Köhl, M.; Klimant, I. A Microoptode Array for Fine-Scale Measurement of Oxygen Distribution. *Sensors Actuators B Chem.* **1997**, *38* (1–3), 122–129.
- (19) Ma, T. Y.; Ran, J.; Dai, S.; Jaroniec, M.; Qiao, S. Z. Phosphorus-Doped Graphitic Carbon Nitrides Grown In Situ on Carbon-Fiber Paper: Flexible and Reversible Oxygen Electrodes. *Angew. Chemie - Int. Ed.* **2015**, *54* (15), 4646–4650.
- (20) Xiao, Z.; Huang, X.; Xu, L.; Yan, D.; Huo, J.; Wang, S. Edge-Selectively Phosphorus-Doped Few-Layer Graphene as an Efficient Metal-Free Electrocatalyst for the Oxygen Evolution Reaction. *Chem. Commun.* **2016**, *52* (88), 13008–13011.
- (21) Lu, X.; Yim, W. L.; Suryanto, B. H. R.; Zhao, C. Electrocatalytic Oxygen Evolution at Surface-Oxidized Multiwall Carbon Nanotubes. *J. Am. Chem. Soc.* **2015**, *137* (8), 2901–2907.
- (22) Sato, Y.; Itoh, K.; Hagiwara, R.; Fukunaga, T.; Ito, Y. On the So-Called “Semi-Ionic” C-F Bond Character in Fluorine-GIC. *Carbon N. Y.* **2004**, *42* (15), 3243–3249.
- (23) Conway, B. E.; Liu, T. C. Characterization of Electrocatalysis in the Oxygen Evolution Reaction at Platinum by Evaluation of Behavior of Surface Intermediate States at the

- Oxide Film. *Langmuir* **1990**, *6* (1), 268–276.
- (24) Favaro, M.; Valero-Vidal, C.; Eichhorn, J.; Toma, F. M.; Ross, P. N.; Yano, J.; Liu, Z.; Crumlin, E. J. Elucidating the Alkaline Oxygen Evolution Reaction Mechanism on Platinum. *J. Mater. Chem. A* **2017**, *5* (23), 11634–11643.
- (25) Surendranath, Y.; Kanan, M. W.; Nocera, D. G. Mechanistic Studies of the Oxygen Evolution Reaction by a Cobalt-Phosphate Catalyst at Neutral PH. *J. Am. Chem. Soc.* **2010**, *132* (46), 16501–16509.
- (26) Huynh, M. H. V.; Meyer, T. J. Proton-Coupled Electron Transfer. *Chem. Rev.* **2007**, *107* (11), 5004–5064.
- (27) Bockris, J. O. M. Kinetics of Activation Controlled Consecutive Electrochemical Reactions: Anodic Evolution of Oxygen. *J. Chem. Phys.* **1956**, *24* (4), 817–827.
- (28) Shinagawa, T.; Garcia-Esparza, A. T.; Takanabe, K. Insight on Tafel Slopes from a Microkinetic Analysis of Aqueous Electrocatalysis for Energy Conversion. *Sci. Rep.* **2015**, *5* (August), 1–21.
- (29) Iwakura, C.; Fukuda, K.; Tamura, H. The Anodic Evolution of Oxygen on Platinum Oxide Electrode in Alkaline Solution. *Electrochim. Acta* **1976**, *21*, 501–508.
- (30) Bockris, J. O.; Otagawa, T. The Electrocatalysis of Oxygen Evolution on Perovskites. *J. Electrochem. Soc.* **1984**, *131* (2), 290.

Chapter 5

General Conclusion

In this thesis, I focused on the synthesis of the carbon nanomaterial and evaluation on the electrocatalytic activity of heteroatom-doped carbon. Synthesis of carbon nanomaterial has been widely approached by numerous methods. Among these methods, electrochemical deposition has attractive advantages such as its low-cost, easy process and room temperature synthesis condition (*Chapter 2*). Thermal deposition technique such as chemical vapor deposition (CVD) is also used for synthesis of carbon nanotube (CNT) because structure of synthesized carbon material is controllable by catalyst and carbon source (*Chapter 3*). In addition, selective heteroatom doping is possible by pyrolysis process using heteroatom sources (*Chapter 3 and Chapter 4*). Using these heteroatom doped carbons, I evaluated the electrocatalytic activity of oxygen reduction reaction (ORR) and oxygen evolution reaction (OER) (*Chapter 3 and Chapter 4*).

First, I adopted the electrochemical deposition for synthesis of carbon using halogenated carbon source such as CCl_4 and CBr_4 in the hydrophobic ionic liquid (*Chapter 2*). Halogenated carbon is easily dehalogenated by electrochemical reaction as carbon source. Graphitic carbon was obtained by carbonization process on graphitic carbon edge through the carbon source supply. Furthermore, H_2O was added as proton source to synthesize the carbon-hydrogen (C-H) bond. Hydrophobic ionic liquid was used as electrolyte because it possesses the wide electrochemical window and controllable the amount of H_2O . As a result, trans-polyacetylene was synthesized by dehalogenation of halogenated carbon and sequential

hydrogenation/protonation step with H₂O by nucleation and aggregation on the nucleation site. On the basis of the result, I firstly reported the synthesis of trans-polyacetylene by electrochemical deposition.

To develop the synthesis of the other carbon allotropes, I synthesized the nitrogen-doped vertically aligned carbon nanotube (N-VA-CNT) by water-assisted CVD and pyrolysis process for nitrogen-doping in *Chapter 3*. In case of VA-CNT synthesis, I discussed carbon source dependence for the first time by using *n*-hexane (C₆H₁₄) and ethylene (C₂H₄). As a result, I successfully synthesized VA-CNT by water-assisted CVD, and controlled the diameter of CNT by carbon source. Besides, VA-CNT synthesized from C₆H₁₄ has higher specific surface area and diameter than VA-CNT synthesized from C₂H₄. N-VA-CNT was synthesized by pyrolysis process of phthalocyanine as nitrogen source with VA-CNT from C₆H₁₄. Besides, ORR activity is enhanced by nitrogen-doping on VA-CNT.

Finally, I showed synthesis and evaluation of ketjen black (KB)-based catalyst in particular for OER of fluorine-doped carbon in *Chapter 4*. Theoretical study showed importance of positively charged carbon sites on OER activity. Therefore fluorine-doped carbon is expected to exhibit OER activity because fluorine has the highest electronegativity. Ketjen black (KB) and Nafion were used as carbon substrate and fluorine precursor to form fluorine-doped Ketjen black (F-KB). As a result, the OER activity was found to be enhanced by fluorine-doping. Furthermore, the nature and quantity of C-F bonds such as semi-ionic and covalent can be controlled by the pyrolysis temperature. In particular, I firstly found that the OER activity depends on quantity of semi-ionic C-F bond regardless of covalent C-F bond. From analysis of Tafel plot and pH dependence on potential, proton activity is not affected by fluorine doping, but OER activity is changed by positively charged carbon of semi-ionic C-F bond. This result implies that there may be

synergistic effect between neighboring semi-ionic C-F bond.

In conclusion, I attempt to control the carbon bonding by electrochemical deposition, water-assisted CVD, and pyrolysis process. Carbon to halogen bond was decomposed and polymerized by electrochemical deposition (*Chapter 2*). Carbon to carbon bond such as diameter of CNT was controlled by water-assisted CVD using carbon source dependence (*Chapter 3*). Carbon to fluorine bond was changed by pyrolysis temperature (*Chapter 4*). In particular, electrocatalytic activity such as ORR and OER was enhanced by specific carbon to heteroatom (*Chapter 3* and *Chapter 4*). Therefore, my results exemplify control of carbon bonding for carbon-based material by selective synthesis method, as well as support to design the electrochemical catalyst for electric charge effect of metal-free heteroatom-doped carbon.

List of Publications

- (1) Yasuda, S.; Yu, L.; **Kim, J.**; Murakoshi, K. Selective Nitrogen Doping in Graphene for Oxygen Reduction Reactions. *Chem. Commun.* **2013**, 49 (83), 9627.
- (2) **Kim, J.**; Shawky, A.; Yasuda, S.; Murakoshi, K. Selective Synthesis of Graphitic Carbon and Polyacetylene by Electrochemical Reduction of Halogenated Carbons in Ionic Liquid at Room Temperature. *Electrochim. Acta* **2015**, 176, 388–393.
- (3) Yasuda, S.; Furuya, A.; Uchibori, Y.; **Kim, J.**; Murakoshi, K. Iron-Nitrogen-Doped Vertically Aligned Carbon Nanotube Electrocatalyst for the Oxygen Reduction Reaction. *Adv. Funct. Mater.* **2016**, 26 (5), 738–744.
- (4) **Kim, J.**; Zhou, R.; Murakoshi, K.; Yasuda, S. Advantage of Semi-Ionic Bonding in Fluorine-Doped Carbon Materials for the Oxygen Evolution Reaction in Alkaline Media. *RSC Adv.* **2018**, 8 (26), 14152–14156.

Acknowledgments

I would like to thank my Prof. Kei Murakoshi for his guidance and discussion of my study. If he did not accept the admission in physical chemistry laboratory of Hokkaido university, I can't have the valuable experience.

I am grateful to Prof. Tetsuya Taketsugu and Prof. Hiroki Habazaki for their interest in my work, and being my committee, for spending time reading my dissertation.

I am thankful to Dr. Satoshi Yasuda, Dr. Hiro Minamimoto, Dr. Tomohiro Fukushima, Dr. Ruifeng Zhou, and Dr. Xiaowei Li for his valuable discussion and direction of research. Thanks to his help, I was able to accept my first order paper. I am also grateful to my laboratory peer for their support on my experiment. I am thankful to Rumi Akiyama. She always assisted my paperwork and application of scholarship.

I heartily thank to Prof. Sam K. Jo for his advice and discussion about research attitude and mind. I sincerely hope that he achieves the innovative research result.

Last but not least, I would like to express my greatest gratitude to my parents, brother, and my grandmother for their support and encouragement. I hope that my family will always be healthy and happy.

Jeheon Kim